Design, Simulation, and Experimental Validation of a Novel High-Speed Omnidirectional Underwater Propulsion Mechanism

Taylor Njaka

Dissertation submitted to the Faculty of the
Virginia Polytechnic Institute and State University
in partial fulfillment of the requirements for the degree of

Doctor of Philosophy
in
Mechanical Engineering

Pinhas Ben-Tzvi, Chair
Stefano Brizzolara, Chair
Corina Sandu
Steve C Southward

December 14, 2020
Blacksburg, Virginia

Keywords: Underwater Rotorcraft, High-Speed ROV, UUV, Omnidirectional Propulsion, Marine Robotics, Mechatronics, UUV Simulation, Maneuvering, System Identification

Design, Simulation, and Experimental Validation of a Novel High-Speed Omnidirectional Underwater Propulsion Mechanism

Taylor Njaka

ABSTRACT

This dissertation explores a novel omnidirectional propulsion mechanism for observation-class underwater vehicles, enabling for operation in extreme, hostile, or otherwise high-speed turbulent environments where unprecedented speed and agility are necessary. With a small overall profile, the mechanism consists of two sets of counter-rotating blades operating at frequencies high enough to dampen vibrational effects on onboard sensors. Each rotor is individually powered to allow for roll control via relative motor effort and attached to a swashplate mechanism, providing quick and powerful manipulation of fluid-flow direction in the hull's coordinate frame without the need to track rotor position. The omnidirectional mechanism exploits properties emerging from its continuous counter-rotating blades to generate near-instantaneous forces and moments in six degrees of freedom (DOF) of considerable magnitude, and is designed to allow each DOF to be controlled independently by one of six decoupled control parameters. The work presented in this dissertation validates the mechanism through physical small-scale experimentation, confirming near-instantaneous reaction time, and aligning with computational fluid dynamic (CFD) results presented for the proposed theorized full-scale implementation. Specifically, it is demonstrated that the mechanism can generate sway thrust at 10-20% surge thrust capacity in both simulation and physical tests. It is also shown that the magnitude of forces and moments generated is directly proportional to motor effort and corresponding commands, in par with theory. Any apparent couplings between different control modes are deeply

understood and shown to be trivially accounted for, effectively uncoupling all six control parameters. The design, principles, and bullard-pull simulation of the proposed full-scale mechanism and vehicle implementation are then thoroughly discussed. Kinematic and hydrodynamic analyses of the hull and surrounding fluid forces during different maneuvers are presented, followed by the mechanical design and kinematic analysis of each subsystem. To estimate proposed full-scale performance specifications and UUV turbulence rejection, a full six-DOF maneuvering model is constructed from first principles utilizing CFD and regression techniques. This dissertation thoroughly examines the working principles and performance of a novel omnidirectional propulsion mechanism. With the small-scale model and full scale simulation and analysis, the work presented successfully demonstrates the mechanism can generate nearly instantaneous omnidirectional forces underwater in a controlled manner, with application to high-speed agile vehicles in dynamic environments.

Design, Simulation, and Experimental Validation of a Novel High-Speed Omnidirectional Underwater Propulsion Mechanism

Taylor Njaka

GENERAL AUDIENCE ABSTRACT

This dissertation explores a novel omnidirectional propulsion mechanism for observation-class underwater vehicles, enabling for operation in extreme, hostile, or otherwise high-speed turbulent environments where unprecedented speed and agility are necessary. The mechanism utilizes independently-powered rotors to command near-instantaneous forces and moments in all six degrees of freedom (DOF). The design allows each DOF to be independently controlled by one of six decoupled control parameters. The method for generating lateral thrust through the mechanism is originally verified through computational fluid dynamic (CFD) tests, but the complete novelty of the lateral maneuver calls for physical verification for any noteworthy validation. The work presented in this dissertation validates the mechanism through physical small-scale experimentation, confirming near-instantaneous reaction time, and aligning with CFD results presented for the proposed theorized full-scale implementation. Specifically, it is demonstrated that the mechanism can generate sway (side/side) thrust at 10-20% surge (forward/backward) thrust capacity in both simulation and physical tests. It is also shown that the magnitude of forces and moments generated is directly proportional to motor effort and corresponding commands, in par with theory. Finally, a full six-DOF model for underwater vehicle trajectory is constructed utilizing detailed maneuvering techniques to estimate full-scale performance. With the small-scale model and full-scale simulation and analysis, the work successfully demonstrates the mechanism can generate nearly instantaneous omnidirectional forces underwater in a controlled manner, with application to high-speed agile vehicles in dynamic environments.

DEDICATION

This dissertation is dedicated to

My parents, Ann and Chima Njaka,

and

My good friends, Dillon Patel and Lauren Ten Cate.

in loving memory of

my grandfather, Dr. Jack Gratzek

and my uncle, Ikechi Njaka

ACKNOWLEDGEMENTS

It is important to know that this dissertation was written in the time period of the 2019-2020 SARS-CoV-2 pandemic. As the virus attacks the bodies of our elders, long-term self-isolation corrodes the mental health of the able. Few are an exception to the latter.

The year 2020 has been incredibly challenging for a large fraction of people in the developed world. The emotional toil is extreme, but during this time I have never seen or felt more love and support from my family and friends. As we march through this living Hell together, it becomes more and more evident that the care we have for one-another is what matters most, driving us to maintain focus in a world of despair. It is through the strength of my advisors, family, and friends that I am able to write this now.

My deepest gratitude falls upon my advisors, who I have eventually grown to recognize as friends. They have consistently supported me over the years while believing in the idea that eventually became the dissertation you see before you now. Namely, I would first really like to thank Dr. Pinhas Ben-Tzvi, who was the first to believe in me and approve this project, while on several occasions picking me up when I have fallen- even outside of academia. The advice and help he has provided has proven invaluable, and I could never thank him enough for it. I would also really like to thank Dr. Stefano Brizzolara, who provided the deepest insights on most aspects of my research while closely guided my progress both in work and in life. He has my eternal respect and friendship. My advisors have played a significant impact on my life and on the accomplishments presented in this dissertation. Furthermore, my committee members Dr. Corina Sandu and Dr. Steve Southward have helped me significantly, in part due to their constructive comments and impact on my academic progress. I am honored to have gotten to know them.

My parents have consistently supported me emotionally though hard times, and even as they have recently suffered the loss of both my uncle Ikechi Njaka and grandfather, they

continue to stay positive and always keep in touch. I have looked up to them my entire life. My grandfather, Dr. Jack Gratzek, originally helped convince me to pursue a Ph.D. many years ago, and I have seen him as a role model, as he stayed fun and positive, never allowing age-induced neurological problems to consume who he was. My grandmother, Kathleen Gratzek, is incredibly loving to every member of our family, and during these times needed to make difficult decisions while staying cheerful and confident. She has never failed at doing so. Jack passed away one week before the submission of this dissertation.

Many close friends such as Dillon Patel, Samantha Owens, Daniel Kramnik, Lauren Ferris, Rebecca Li, Brandon Avila and others, have called often just to show their fun-loving support during these difficult times, even as they themselves are under emotional distress. Close friends like these are hard to come by in life, and they played a large role in giving me the strength to see this through. I would also really like to thank Lauren Ten Cate for her critical role in empowering me to get this done.

I would also like to thank my current and former colleagues and professors Franz Hover, Daniel Stilwell, Lakshmi Miller, Naina Pasharoti, Georgios Kontoudis, Suraj Pawar, Jack Webster, the McKibbins and others, for their continued help and support. Additionally, professional advisors Mary Gaskill and Tremayne Waller played a major role in my success.

The force-sensing apparatus and accelerated fabrication of the small-scale model would not have been possible without the help of a team consisting of Jonah Fike, Marco Brizzolara, and Kye Gonino during the summer of 2019. Later, during the 2020 pandemic, Kye helped greatly with further fabrication and then testing for the lateral force compensation algorithm presented in this dissertation. Without his help, many of the tests would have not been possible in the short timespan they were conducted in. Many of the people mentioned here (and not mentioned) have provided me with the strength to stay productive while under heavy emotional siege. They were responsible for the considerable increase in productivity during the 2020 pandemic. I can never thank them enough.

TABLE OF CONTENTS

LIST OF FIGURES

LIST OF ABBREVIATIONS

AoA	Angle of Attack
AUV	Autonomous Underwater Vehicle
BARFA	Blade-Axis Re-enforcing Flap Adapter
CAD	Computer-Aided Design
CFD	Computational Fluid Dynamics
DOF	Degree(s) of Freedom
EOM	Equations(s) of Motion
ESC	Electronic Speed Controller
IMU	Inertial Measurement Unit
LPM	Lumped-Parameter Model
ROV	Remotely-Operated Vehicle
PMM	Planar-Motion Mechanism
PWM	Pulse-Width Modulation
SSPAM	Servo-Swashplate Actuation Mechanism
UUV	Unmanned Underwater Vehicle
VPMM	Virtual Planar-Motion Mechanism
b.l.	Botton-left servo in a triangular configuration
b.r.	Botton-right servo in a triangular configuration
top	Top servo in a triangular configuration

NOMENCLATURE

A, S	Area
α	Global surge-command control parameter
β	Generalized pitch/yaw-command control parameter
β_{y}	Global pitch moment-command control parameter
β_{z}	Global yaw moment-command control parameter
$C_A(\nu)$	Six-DOF hydrodynamic added-Coriolis matrix
$C_{RB}(\nu)$	Six-DOF rigid-body Coriolis matrix
$D(\nu)$	Six-DOF hydrodynamic damping Matrix
D	Drag
δ	Global roll command control parameter
δ_{c}	SNAME virtual pitch-elevator command for canards
δ_{e}	SNAME virtual pitch-elevator command for rear fins
δ_{r}	SNAME virtual yaw-rudder command for rear fins
δ_{roll}	Virtual roll command for rear fins
δ_i	Physical angular deflection of a control-surface with index i
η	World-frame position vector $[x, y, z, \phi, \theta, \psi]^\top$
$\forall$	Volume

Γ Generalized sway/heave-command control parameter

Γ_{y} Global sway thrust-command control parameter

Γ_{z} Global heave thrust-command control parameter

K Body-frame roll-moment

K Scaling factor used for scaling forces in CFD to achieve simulation convergence

M Body-frame pitch-moment

N Body-frame yaw-moment

n Number of timesteps in an unsteady CFD simulation

n Total number of rear control surfaces

$\mathrm{n_e}$ Number of rear control surfaces that are not positioned at $\Phi_i = \frac{\pi}{2}$ or $\Phi_i = \frac{3\pi}{2}$

$\mathrm{n_r}$ Number of rear control surfaces that are not positioned at $\Phi_i = 0$ or $\Phi_i = \pi$

ν Body-frame motion-states vector $[u, v, w, p, q, r]^\top$

ϕ World-frame roll orientation angle

ϕ_{b} Hydrofoil attack angle

Φ_i Static alignment angle (about roll axis) of a control-surface with index i

p Body-frame roll rotation rate

P Matrix composed of time-series velocity-states column vectors arranged: $\left[\overrightarrow{up},\ \overrightarrow{p|p|},\ \overrightarrow{\dot{p}}\right]$

$P^\dagger$ Pseudo-inverse of non-square matrix P, equal to $(P^\mathsf{T}P)^{-1}P^\mathsf{T}$

ψ World-frame yaw orientation angle

ψ_{drift} Vehicle drift angle (heading - orientation) about the yaw-axis

q Body-frame pitch rotation rate

ρ Density of saltwater

r Body-frame yaw rotation rate

r Radial distance from the rotor's center of rotation along the blade

R_i Position of blade attachment point along r

R_o Position of the outermost blade tip along r

R Matrix composed of time-series velocity-states column vectors arranged: $\left[\overrightarrow{ur}, \overrightarrow{r \cdot r}, \overrightarrow{\dot{r}}\right]$

$R^\dagger$ Pseudo-inverse of non-square matrix R, equal to $(R^\mathsf{T}R)^{-1}R^\mathsf{T}$

τ Six-DOF control force vector of all propulsion and control-surface forces

τ_{lag} Time delay from sensor lag in the feedback loop (figs. 2.5 and 2.6)

θ World-frame pitch orientation angle

θ_{drift} Vehicle drift angle (heading - orientation) about the pitch-axis

θ_{rot} Blade orientation about the rotational axis of the rotor

u Body-frame surge (forward positive) velocity

U Matrix composed of time-series velocity-states column vectors arranged: $\left[\overrightarrow{u \cdot u}, \overrightarrow{\dot{u}}\right]$

$U^\dagger$ Pseudo-inverse of non-square matrix U, equal to $(U^\mathsf{T}U)^{-1}U^\mathsf{T}$

v Body-frame sway (rightward positive) velocity

V,V(r) Velocity

V Matrix composed of time-series velocity-states column vectors arranged: $\left[\overrightarrow{u\dot{v}},\ \overrightarrow{v_{\mathrm{I}}\dot{v}_{\mathrm{I}}},\ \overrightarrow{\dot{v}}\right]$

$V^{\dagger}$ Pseudo-inverse of non-square matrix V, equal to $(V^{\mathsf{T}}V)^{-1}V^{\mathsf{T}}$

w Body-frame (downward positive) heave

X Body-frame surge (forward positive) force

$(x, y, z)_G$ Sub-components of the position for center of gravity

Y Body-frame sway (rightward positive) force

Y(r) Beam deflection

Z Body-frame heave (downward positive) force

B Buoyant displacement

C(r) Blade cord length (distance between leading and trailing edges) evaluated at r

C_d Drag coefficient of the FX76-100 hydrofoil

C_G Center of Gravity

C_l Lift coefficient of the FX76-100 hydrofoil

C_i Innermost cord length $C(r = R_i)$ of the blade

C_o Outermost cord length $C(r = R_o)$ of the blade

E Elastic modulus; Young's modulus

$F, F_{(\mathrm{x,y,z})}$ Force; Forces along $\hat{x}$, $\hat{y}$, and $\hat{z}$, respectively

$F_{(1,4)}$ Blade-induced drag force out of the page according to Fig. 3.27 in Quadrants 1 and 4, respectively

$f_{(1-6)}$ Linear forces measured by tension gauges 1-6, respectively

$F_{(2,3)}$ Blade-induced drag force into the page according to Fig. 3.27 in Quadrants 2 and 3, respectively

F_{surge} Surge force generated specifically from surge command α

F_{sway} Sway force generated specifically from sway command Γ

$F_{\text{tangential plane}}$ Byproduct force directed into the page via blade drag, according to Fig. 3.27

$F_{RotorLim}$ Rotor-force upper limit for CFD simulation convergence

$G(\eta)$ Six-DOF force vector of gravitational restoring forces and moments

i Index

$I(\text{r})$ Area moment of inertia, also known as the second moment of inertia, evaluated at r

$I_{(ij)}$ Moment of inertia about *(ij)*

$K_{\dot{p}}$ Added-mass sub-component of roll moment K that multiplies $\dot{p}$

$K_{(\text{subscript})}$ Sub-component of roll moment K which multiplies the product of all elements in the specified *subscript*

K_{meas} Hydrodynamic roll moment measured during a CFD maneuver

L Length

$L_{(\text{x,y,z})}$ Pivot lengths within the force-sensing apparatus

m Mass

$M_{\dot{q}}$ Added-mass sub-component of pitch moment M that multiplies $\dot{q}$

$M_{\dot{w}}$ Added-mass sub-component of pitch moment M that multiplies $\dot{w}$

$M_{(\text{subscript})}$ Sub-component of pitch moment M which multiplies the product of all elements in the specified *subscript*

$M_{(\text{x,y,z})}$ Moments about $\hat{x}$, $\hat{y}$, and $\hat{z}$, respectively

M_A Six-DOF hydrodynamic added-mass matrix

M_{RB} Six-DOF rigid-body mass matrix

$M_r(\text{r})$ Bending moment

$N_{\dot{r}}$ Added-mass sub-component of yaw moment N that multiplies $\dot{r}$

$N_{\dot{v}}$ Added-mass sub-component of yaw moment N that multiplies $\dot{v}$

$N_{(\text{subscript})}$ Sub-component of yaw moment N which multiplies the product of all elements in the specified *subscript*

N_{meas} Hydrodynamic yaw moment measured during a CFD maneuver

N_{ext} External yaw moment acting on the body

$T, T_{(\text{x,y,z})}$ Torque; Torque about body-frame $\hat{x}$, $\hat{y}$, and $\hat{z}$, respectively

$X_{\dot{u}}$ Added-mass sub-component of surge force X that multiplies $\dot{u}$

$X_{(\text{subscript})}$ Sub-component of surge force X which multiplies the product of all elements in the specified *subscript*

X_{meas} Hydrodynamic surge force measured during a CFD maneuver

X_{ext} External surge force acting on the body

$Y_{\dot{r}}$ Added-mass sub-component of sway force Y that multiplies $\dot{r}$

$Y_{\dot{v}}$ Added-mass sub-component of sway force Y that multiplies $\dot{v}$

$Y_{(\text{subscript})}$ Sub-component of sway force Y which multiplies the product of all elements in the specified *subscript*

Y_{meas} Hydrodynamic sway force measured during a CFD maneuver

Y_{ext} External sway force acting on the body

$Z_{\dot{q}}$ Added-mass sub-component of heave force Z that multiplies $\dot{q}$

$Z_{\dot{w}}$ Added-mass sub-component of heave force Z that multiplies $\dot{w}$

$Z_{(\text{subscript})}$ Sub-component of heave force Z which multiplies the product of all elements in the specified *subscript*

ω Input frequency of the disturbance being examined (Figs. 2.5 and 2.6)

Motor Effort The raw PWM command sent to the ESCs driving the motors, remapped to percentage

Motor Offset The smallest *Motor Effort* value which actually causes the motors to spin

K_1 The ratio between *intended* sway force and Γ

K_2 The ratio between *unintended tangential* sway force and $\alpha \cdot \Gamma$

K_3 The ratio between K_2 and K_1, effectively constant.

K_α Constant scaling factor linking command α to the output force F_{surge}, encompassing all unknown hydrodynamic and motor-rate properties

K_Γ Constant scaling factor linking command Γ to the output force F_{sway}, encompassing all unknown hydrodynamic and motor-rate properties

Chapter 1

Introduction

1.1 Background

This dissertation explores a novel omnidirectional propulsion mechanism for observation-class underwater vehicles, enabling for operation in environments outside the scope of current technology. The mechanism utilizes independently-powered rotors to command near-instantaneous forces and moments independently in all six degrees of freedom (DOF). The work presented in this dissertation validates the mechanism through physical small-scale experimentation, confirming near-instantaneous reaction time, and aligns with CFD results presented for the proposed theorized full-scale implementation. It is also shown that the magnitude of forces and moments generated is directly proportional to motor effort and corresponding commands, in par with theory. Any apparent couplings between different control modes are deeply understood and shown to be trivially accounted for, effectively uncoupling all six control parameters. With the small-scale model and full scale simulation and analysis, the work successfully demonstrates the mechanism can generate nearly instantaneous omnidirectional forces underwater in a controlled manner, with application to high-speed agile vehicles.

1.2 Contributions

This dissertation introduces and explores a novel omnidirectional propulsion mechanism that can potentially allow a small vehicle to operate in environments far outside the range of conventional ROVs or AUVs. The contributions of the work presented can be broadly described as follows:

1. **Design**

   This dissertation outlines the design methodology behind underwater rotorcraft. The concepts and designs presented in this dissertation regarding the mechanism are novel and unique. Furthermore, a novel off-axis force-sensing apparatus is designed and fabricated, validating the mechanism's underlying theory through small-scale experimentation.

2. **Dynamics**

   The methodology for generating instantaneous lateral force underwater is both hydrodynamically and kinematically novel, enabling true quick omnidirectionality in all DOF.

3. **Control**

   A novel control methodology is introduced for the mechanism, allowing each DOF to be controlled independently by one of six decoupled control parameters. Furthermore, the additional implementation of control-surfaces on future UUV implementations that are optimized for specific speeds is introduced and discussed in conjunction with traditional maneuvering.

4. **Simulation**

   (a) Maneuvering

A clear and straightforward methodology for simulating trajectory of any streamlined UUV is outlined entirely from first principles. Redundancies between added-Coriolis and hydrodynamic linear viscous damping terms in the literature for maneuvering models are clarified in this study. Some studies explicitly avoid the use of VPMM maneuvers in coefficient estimation due to potential complications arising from said redundancies [23].

(b) Computational Fluid Dynamics (CFD)

This dissertation quantifies input downscaling of CFD input forces and re-upscaling of output measurements to achieve simulation convergence without increasing cell density. Also, a new method (Eqn. 4.12) is introduced to calculate momentum-based forces through a virtual surface with nonzero volume, proving useful in virtual box thrust estimation.

1.3 Direct Applications

Section 2.3.1 outlines how fluid turbulence-based disturbances on a fully-submerged, neutrally-buoyant ROV can be treated as imposed velocity on the craft's reference frame, regardless of vehicle size. Rejecting such disturbances is nontrivial and largely dependent on agility, allowing for many direct applications of the proposed mechanism. Direct applications for the work presented in this dissertation are outlined as follows:

1. **Observation**

   (a) Hull inspection and damage reporting

   The ability to lock any pose and with a moving external object in the presence of fluid turbulence allows for *moving hull* inspection, or docked hull inspection under normally inoperable or time-sensitive conditions. For example, a submerged

submarine may require a quick hull inspection or damage report without surfacing or even while moving, which can only be accomplished through a device with capabilities similar to our proposed mechanism.

(b) Dock or area inspection

Dock or seafloor inspection can be achieved faster and under a wider range of conditions.

(c) Biological observation

Applications include prolonging underwater observation or film of relatively fast-moving or large migrating marine life.

2. **Light Manipulation**

(a) Underwater welding or cutting onto moving, oscillating, or stationary surfaces under time-critical or otherwise turbulent conditions

(b) Sensor or instrument delivery onto fast, illusive objects or specific humane locations on living specimen

3. **Payload Delivery**

The ability for an unmanned vehicle to move at high speed with sufficient agility to dodge potential countermeasures can help guarantee payload delivery. Likewise, it could help intercept or divert threats of a similar nature.

1.4 Dissertation Structure

The rest of this dissertation is outlined as follows:

- **Chapter 2** officiates the problem statement, introducing the proposed design with comparison to current technology. It covers simulated disturbance rejection performance for various forms of turbulence.

- **Chapter 3** serves to prove the mechanism's rationality as a whole through experimental comparison with hypothesis, presenting the working principles, small-scale design, experimentation and results. The findings and structure of this chapter are largely taken from a study [34] published to IEEE/ASME *Transactions on Mechatronics* in December 2020, and the results are believed to be significant.

- **Chapter 4** thoroughly analyses the design and simulation of a proposed full-scale mechanism.

- **Chapter 5** covers underwater vehicle trajectory simulation in 3-space, allowing for accurate vehicle performance estimations used throughout the dissertation.

- **Chapter 6** summarizes the dissertation and details future work on the subject.

- **Appendix** details the ROVs and AUVs discussed in previous chapters.

1.5 Related Publications

Disclosure: Content from these publications has been used extensively throughout this dissertation:

Journal Articles

1. Taylor Njaka, Stefano Brizzolara and Pinhas Ben-Tzvi. "Design and Experimental Validation of a Novel High-Speed Omnidirectional Underwater Propulsion Mecha-

nism," in *IEEE/ASME Transactions on Mechatronics*, December, 2020. doi: 10.1109/TMECH.2020.3037887.

2. Taylor Njaka, Stefano Brizzolara, and Daniel J Stilwell. CFD Investigation of Hull-Rudder Interaction for Improved Maneuvering Models. *SNAME Transactions 2019*, Vol 127, 2019.

Conference Articles

1. Taylor Njaka, Stefano Brizzolara, and Pinhas Ben-Tzvi. Design and Simulation of a Novel High-Speed Omnidirectional Fully-Actuated Underwater Propulsion Mechanism. In *Proceedings of the 2019 ASME IDETC/CIE 2019*. ASME, 2019. doi:10.1115/DETC2019-97534.

2. Taylor Njaka, Lakshmi M Miller, Stefano Brizzolara, and Daniel J Stilwell. Method for Improving Existing Maneuvering Models to Accommodate Large Drift Angles. In *OCEANS MTS/IEEE Global 2020*. IEEE, 2020.

Patents

1. T. Njaka, P. Ben-Tzvi, S. Brizzolara, "Highly-Agile Omnidirectional Fully-Actuated Novel Underwater Propulsion Mechanism", U.S. Provisional Patent Application No. 63/116,380, November 20, 2020.

Chapter 2

Problem Statement, Current Technology, and Proposition

Much of the content of this chapter is directly adapted from [34], published in December, 2020.

2.1 Problem Statement and Proposition

Long has there been a divide between the class of submersibles composed of streamlined, torpedo-shaped vehicles (autonomous underwater vehicles (AUVs)) and that of omnidirectional or semi-omnidirectional crafts resembling the famous *ALVIN* submersible (remotely operated vehicles (ROVs)). Crafts such as the latter are capable of complex tasks involving external manipulation but are lethargic in nature and prone to flow-based disturbances, as found in shallow waters at stormy conditions or in turbulent tidal environments near artificial piers. There exists a need for an unmanned underwater vehicle (UUV) which combines the speed and agility of AUVs with the full-omnidirectionality and precision of ROVs [40, 43, 30]. Such a vehicle could potentially operate in conditions unreachable to the other two vehicle classes, while reducing the total operating time and thereby the financial and strategic cost for deployment in ROV-specific applications.

The growing interest in robots replacing humans in turbulent, potentially dangerous environments [51] where precision, speed, and robustness are necessary [10] has inspired the development of a new class of underwater robotic thrust mechanism capable of true

agile omnidirectionality in a compact design. Fig. 2.1 outlines the mechanism. Challenges include but are not limited to minimizing reaction time to position disturbances, which is hindered by the delay of accelerating water and the thrust-to-mass ratio of any smaller craft attempting to actively reject disturbance. For large crafts, resilience to disturbances is inherent in vehicle mass, but fast position control is not practical. In much smaller crafts, fast position control is possible but delayed by the acceleration time of traditional ducted thrusters, making their inherent susceptibility to disturbances difficult to overcome.

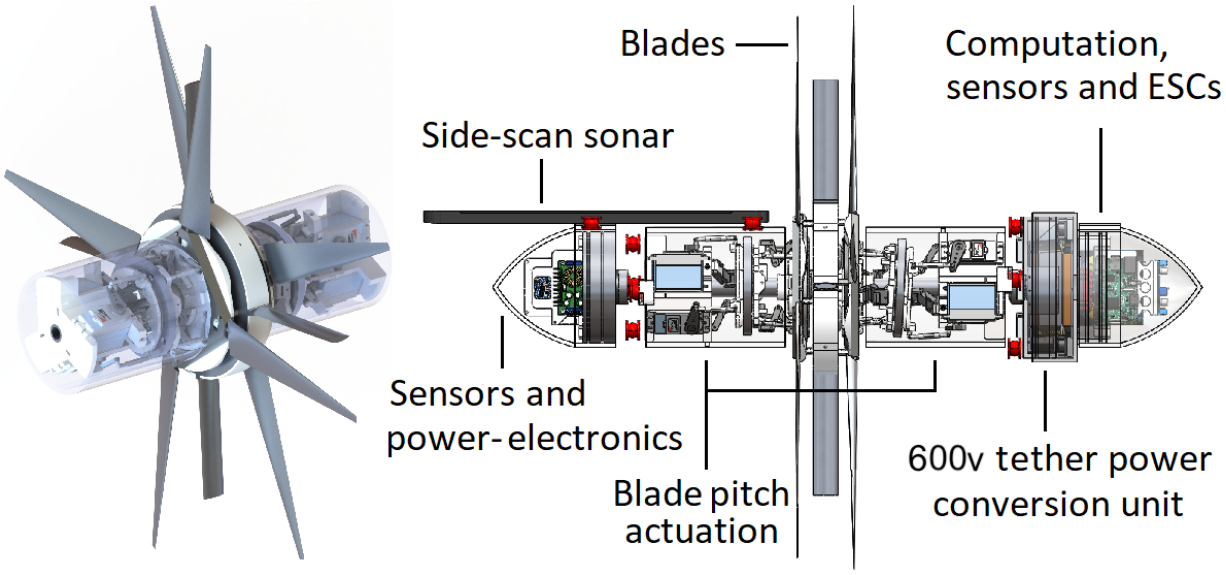

Figure 2.1. (Left) Propulsion mechanism. **(Right)** UUV implementation, with displacement 10.81kg and total vehicle length 0.86m.

2.2 AUVs

Classifying the proposed design with AUVs or ROVs is largely subjective. Traditional AUVs are high-speed, underactuated flight vehicles used primarily for underwater mapping and survey applications. Omnidirectional ROVs, on the other hand, are used primarily for inspection and intervention. Like the proposed design, ROVs share the same zero-turning radius benefit that results from their omnidirectionality, but suffer greatly in maximum

speed and agility, where *agility* can be measured as the potential for instantaneous acceleration on demand. This is quantified by dividing maximum thrust by the sum of mass and added mass, where *added mass* is the virtual added mass created by fluid momentum around an accelerating body. The proposed design possesses the speed capabilities of traditional AUVs, while maintaining the zero-turning radius of omnidirectional ROVs [33] at low speed, and negligible full-turning radius at *sustained* maximum speed. Figure 2.2 compares the relevant maximum-velocity characteristics of traditional AUVs [31, 20, 7] with those of our proposed design.[1]

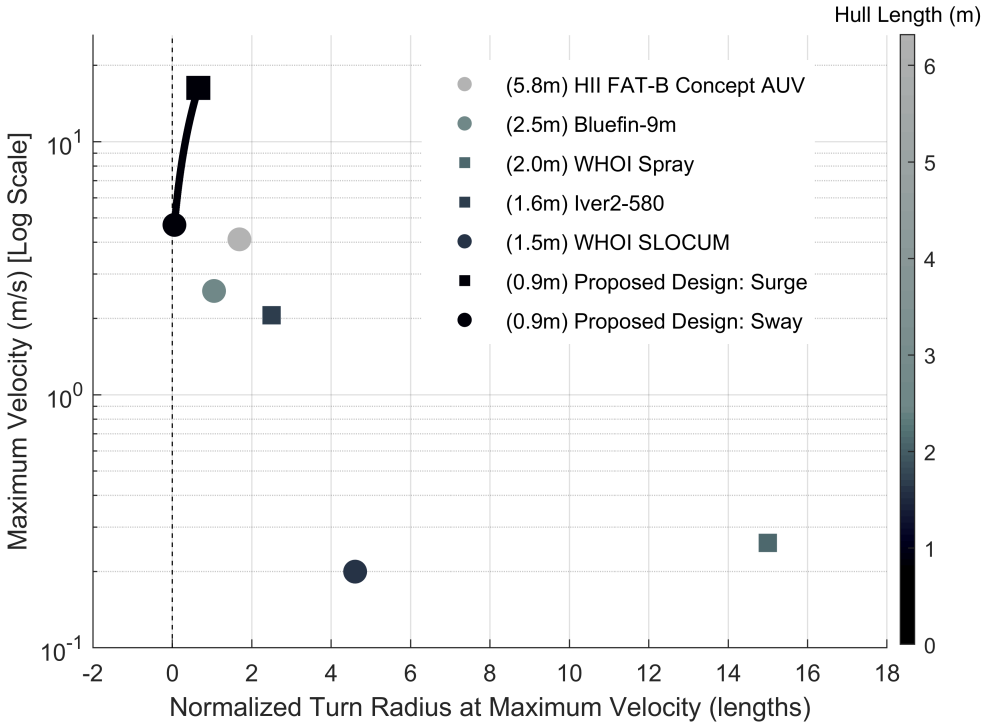

Figure 2.2. A general representation of performance characteristics of typical AUVs compared with that of the proposed design at maximum velocity.

[1]See Chapter 5 for methodology behind calculating hydrodynamic added-mass and drag properties of AUV-profiled hulls (including that of our proposed design) for trajectory simulation. The turn radii of Huntington-Ingalls' conceptual AUV design and the proposed design are calculated using CFD and modelling methods also presented in Chapter 5.

2.3 ROVs

With its omnidirectionality and ability to carry and manipulate a payload, the proposed system is perhaps better classified with ROVs. Its high power consumption also bolsters this classification [21], as it would require a tether for missions exceeding 15 minutes. Fig. 2.3 compares *mass + added mass, top speed,* and *agility* of typical omnidirectional ROVs [2, 28, 46] with the proposed design characteristics. Added masses are calculated from vehicle geometries [15, 24] and virtual planar-motion mechanism tests [35]. For completeness, a wide range of ROVs is considered ranging from *heavy work-class* ROVs to *observation-class* ROVs in the size range of the proposed system. The ROV-profiled *Alvin* is also included for reference.

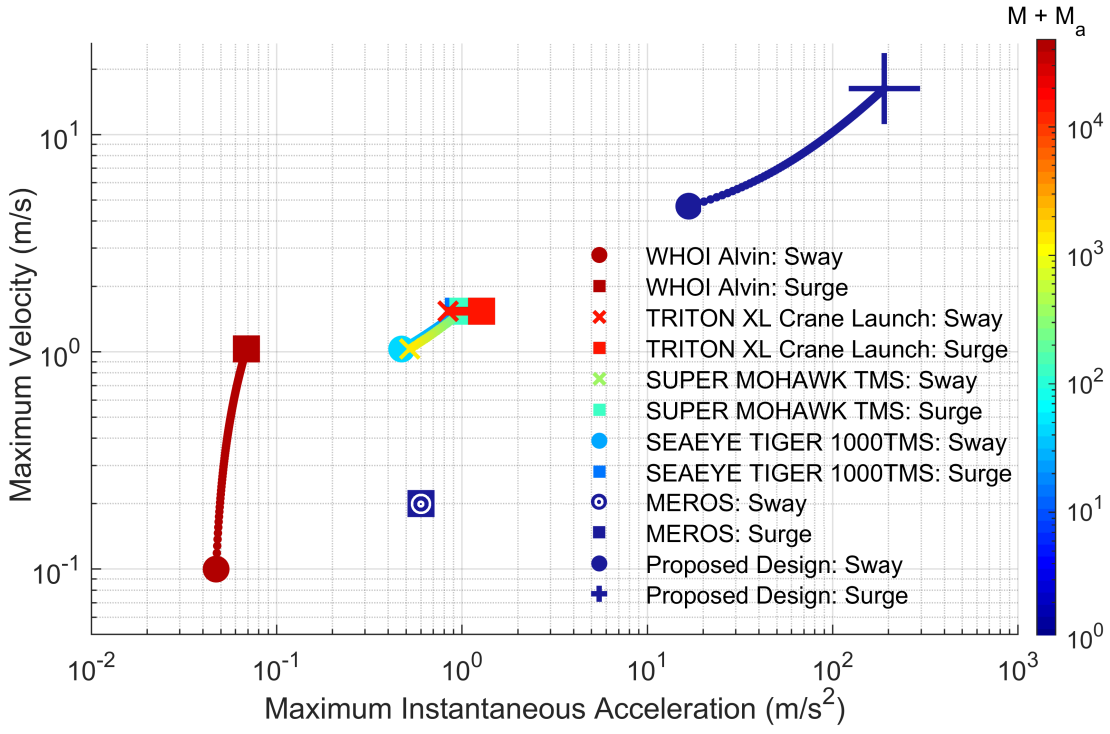

Figure 2.3. A comparison of mass, top speed, and agility-based characteristics of typical ROVs with proposed design.

One small-profile omnidirectional ROV, the *MEROS* [9], attempts to achieve adequate agility by maximizing thrust and minimizing size, but limitations using this method are realized as the craft's very thrusters greatly impact its final volume and shape profile. A CAD representation of the MEROS is shown in Fig. 2.4.

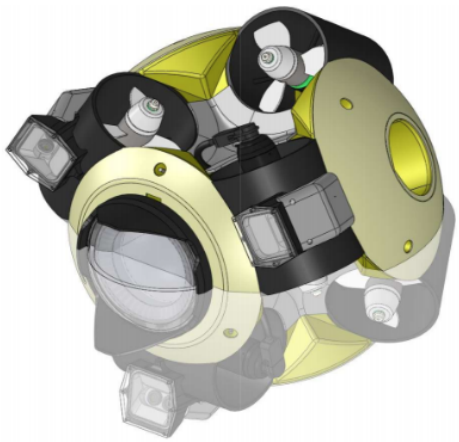

Figure 2.4. [9] CAD representation of the *MEROS* ROV. With a diameter of 0.4m, the *MEROS* is similar in size to the proposed design, which has a length of 0.406m without nose attachments.

The proposed design decouples blade-pitch actuator loads from rotor torques and forces while exploiting properties of already-moving water to eliminate the delay between actuator action and force output [33]. Such high agility and reaction time may allow the craft to not only *react to* but actively *reject* various types of disturbances. Using techniques presented throughout this dissertation,[2] it is possible to quantify and map responses to different forms of disturbance.

[2]See Chapter 5 for methodology behind calculating hydrodynamic added-mass and drag properties of the proposed design for trajectory modelling, including final update laws and vehicle dynamics. Propulsive properties are calculated using methods presented in Chapter 4.

2.3.1 Disturbance Rejection Performance

Ship hull inspection is necessary for both military and commercial applications. It occurs in shallow water, where stormy weather can perturb even the relative sanctuary of a harbor. Manual inspection is costly, and autonomous inspection is vastly aided by speed, agility, and robustness to turbulence. Potentially hazardous objects detected by instruments on or under a dock require closer inspection, and in stormy conditions with bobbing or moving ships, autonomously driven inspection may delay an operation. In military practices, delays like this are unacceptable and potentially devastating. A submerged submarine, for example, may require a quick hull inspection or damage report without surfacing or even while moving, which can only be accomplished through a device with capabilities similar to our proposed mechanism. For a UUV to achieve such tasks, it must be able to actively reject high-frequency heavy turbulence through its agility and its ability to direct large amounts of thrust on demand with a small overall profile.

High agility allows a craft to not only *recover from*, but actively *reject* different types of disturbances. Fluid disturbances are different from external mechanical force-based disturbances due to the fact that neutrally buoyant bodies, when completely submerged in a carrier fluid, are compelled to accelerate in unison with surrounding fluid so long as the surrounding fluid accelerates relatively uniformly, as in the presence of a wave with wavelength greater than the hull length in the direction of wave propagation, or near some integer division of said length [42]. Such fluid turbulence-based disturbances can thus be treated as imposed velocity on the craft's reference frame, regardless of the craft's size. Modeling these rejections should be akin to modeling reference frame synchronization with a moving object in a tracking maneuver, which by itself is a compelling test of maneuverability.

Inertial measurement units (IMUs) on the craft can detect the corresponding imposed acceleration and the craft can potentially actively reject some of it, so long as no acceleration or velocity performance characteristics are saturated. Performance characteristics regarding the delay due to acceleration measurement and actuator movement are also measured and quantified. Servos used in this mechanism have an operational range of $\pm 30^o$ rotation. 0^o arm positions yield 0-N force output, and 6.5° deflection is calculated to yield upwards of 2500N forward thrust at 50% efficiency [see 4.2.1]. KST BLS662 servos have a 0-60^o time of 0.14 seconds and hence a 0-7^o time of roughly 0.016 seconds. The proposed design decouples servo loads from propeller torques and forces while exploiting properties of already-moving water to kill the delay between actuator action and force output [see 4.2.2]. A "force rate" limit due to servo speed can then be set at $\frac{2500N}{0.016sec}$, or 164 kN/s (21 kN/sec for sway). Recall the "disturbance rejection performance" for a fluid-based disturbance is akin to "tracking performance" of position/velocity synchronization with a moving reference. We model tracking and disturbance rejection performance in a block diagram that includes all said acceleration, velocity, and force-rate limitations in Fig. 2.5(a)[39]. The expected turbulence-disturbance rejection performance of the proposed mechanism is then compared with that of typical ROVs in Figs. 2.5(b) and 2.5(c).

A time lag $\tau_{\text{lag}} = 2\text{ms}$ was considered for the feedback loop to incorporate expected delays associated with IMU readings and loop speed, where the model would be best represented as a discretized system with timestep τ_{lag}. However, with τ_{lag} many times smaller than $\frac{1}{4}$ the input period ($\tau_{\text{lag}} \ll \frac{1}{4}(\frac{2\pi}{\omega})$), it was cast from the simulation entirely. Other ROV models are expected to experience much higher delays than the proposed design due to the fact that their rotors must accelerate and decelerate themselves with their surrounding water from idle to generate force, which the proposed design avoids altogether. Despite this, we still approximate τ_{lag} for other ROVs to *equal* that of the proposed design, to dispel all doubt on the superiority of its performance in this regard.

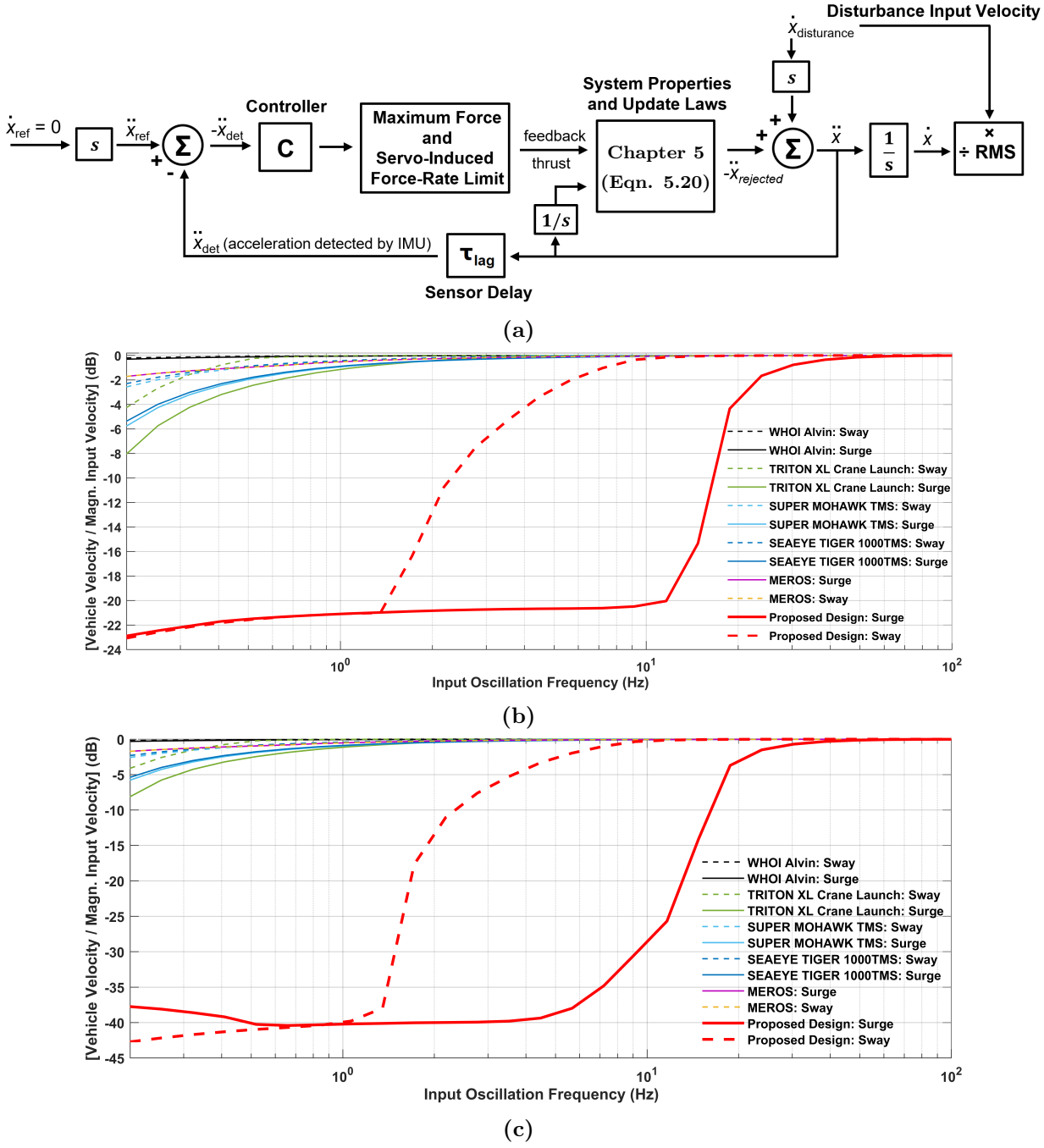

Figure 2.5. (a) A block diagram detailing the process of fluid-driven velocity disturbance/ turbulence-rejection using accelerometer readings, and (b) A comparison of fluid-driven velocity disturbance-rejection of the proposed mechanism with different ROV models, with simple proportional feedback C = 10. (c) Velocity disturbance-rejection comparison of ROVs with C = 100. The amplitude of input velocity, which is the simulated disturbance, is locked at 2m/s to maintain consistent energy flux. Proportional control is shown because the extremely limited agility of traditional ROVs induces integrator windup at low frequencies. The proposed design excels considerably over typical commercial ROVs for 2m/s velocity disturbance input in all cases.

Assuming larger omnidirectional craft even incorporate IMUs for active disturbance rejection from their fluid surroundings, it is evident their lethargy greatly limits the extent to which they can adequately reject imposed accelerations. However, the extent to which these ROVs can limit their position shift due to mechanical force disturbances is greatly aided by their own sheer masses. A block diagram representing external force-based disturbance rejection to position shift is shown in Figure 2.6(a) while Figure 2.6(b) compares the expected performance of the proposed mechanism with that of several omnidirectional ROVs.

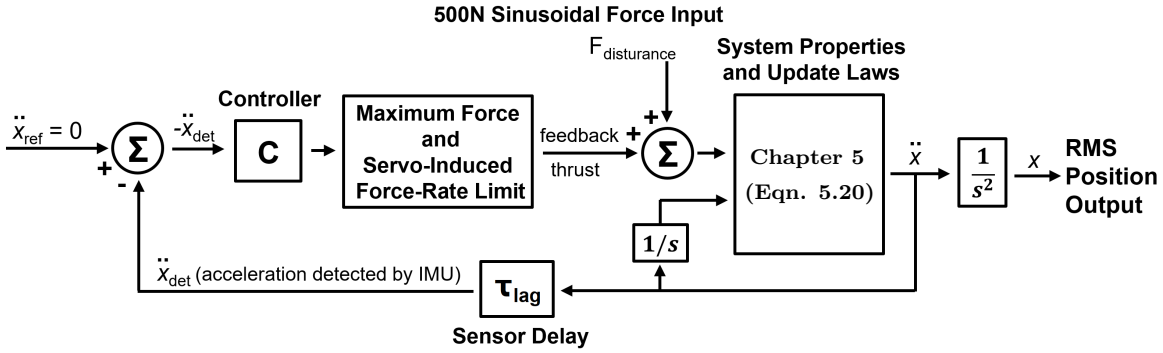

(a)

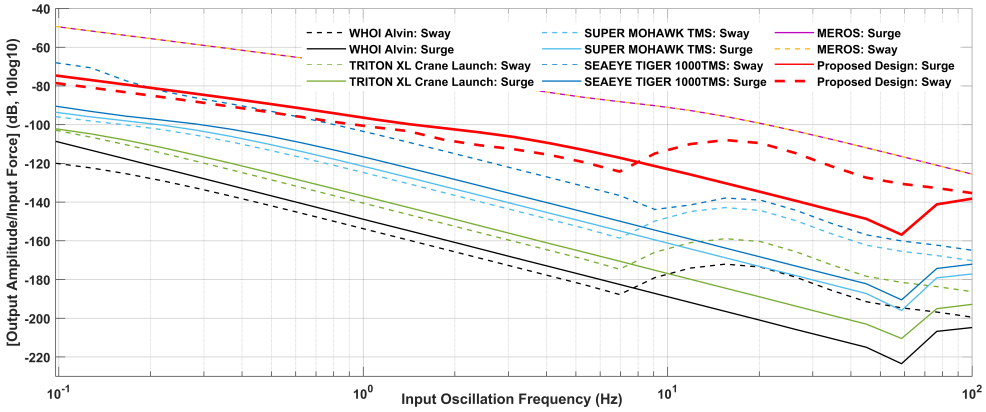

(b)

Figure 2.6. (a) A block diagram detailing the process of external force-driven disturbance-rejection using accelerometer readings, and (b) A comparison of force-driven position disturbance-rejection of the proposed mechanism with different ROV models at 500N force input and proportional control. Feedback is based on IMU acceleration data.

It is evident the proposed design can potentially operate in extreme environments inaccessible to modern ROVs by actively rejecting velocity and/or force-based disturbances.

Chapter 3

Concepts, Design, and Findings

The ability for the proposed craft to vector thrust within its low profile and still control tremendous power may allow it to achieve exceptional maneuverability, but the concept must first be tested. The purpose of this chapter is to explain the working principles, and demonstrate the dynamic thrust ability of the novel omnidirectional thrust mechanism through physical small-scale experimentation. A small-scale model is designed only for static force-readings, in stark contrast to the proposed full-scale dynamic model presented in Chapter 4. Both models are designed around Bullard Pull conditions for omnidirectionality, as they are expected to be equally responsive along any two opposite directions. They both share the same mechanism.

As such, this chapter details the design, working principles, and testing of of a mechanism that utilizes independently-powered rotors to command near-instantaneous forces and moments in all six degrees of freedom. In this chapter, a small-scale force-validating model is fabricated and tested for various force and moment commands. Kinematic and hydrodynamic analyses of the hull and surrounding fluid forces during various blade maneuvers are presented, followed by the mechanical design and kinematic analysis of each subsystem in a small scale model. Experimental results of the small-scale model are presented that verify the concepts presented for the larger-scale model. Finally, an open-loop mathematical model is constructed with decoupled parameters for each degree of freedom.

This chapter serves to prove the mechanism's rationality as a whole through experimental comparison with hypothesis. The findings and content of this chapter are largely adapted from [34] published to IEEE/ASME *Transactions on Mechatronics* in December 2020, and the results are believed to be significant.

3.1 Working Principles

We propose a small craft capable of true omnidirectionality at high speeds. The proposed design utilizes two decoupled counter-rotating rotors, each consisting of four highly-actuated blades centered around a hollow tubing framework. The central tubing network is chosen to allow for the safe wiring of four 670-watt brushless motors operating at maximum load. The hull is intended to be largely free-flowing for required motor cooling and quick deployment. Such cooling is made necessary by the considerable power-to-volume ratio of the motors, enabling the craft to produce upwards up 2500N on its primary axis [33]. Gyroscopic and similar inertial effects are assumed to largely cancel out, becoming negligible with respect to the magnitude of forces and moments generated. Designed mostly around pre-manufactured parts, the outer hull has a main diameter of 0.14m (5.5in) and length of 0.41m (16in) without nose attachments. Fig. 3.1 presents an overview of the full-scale design.

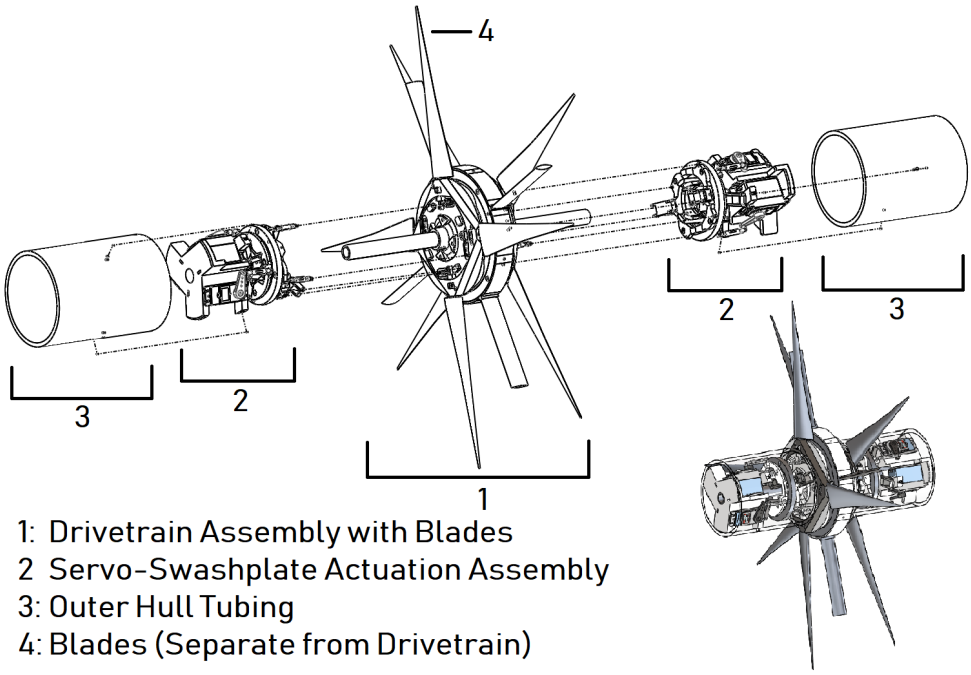

Figure 3.1. Overview of all full-scale model sub-assemblies.

Each of the two rotors contains one servo-swashplate actuation mechanism (SSPAM), which must quickly manipulate the pitch of spinning blades in a passive controlled manner, independent of the rotation rate. This is realized by using three servos to alter the planar projection of a wide bearing assembly (swashplate) connected to the trailing edge of each blade. For explanation purposes, we will assume each SSPAM is actually composed of *four* servos: +y, -y, +z, and -z, as shown in Fig. 3.2.

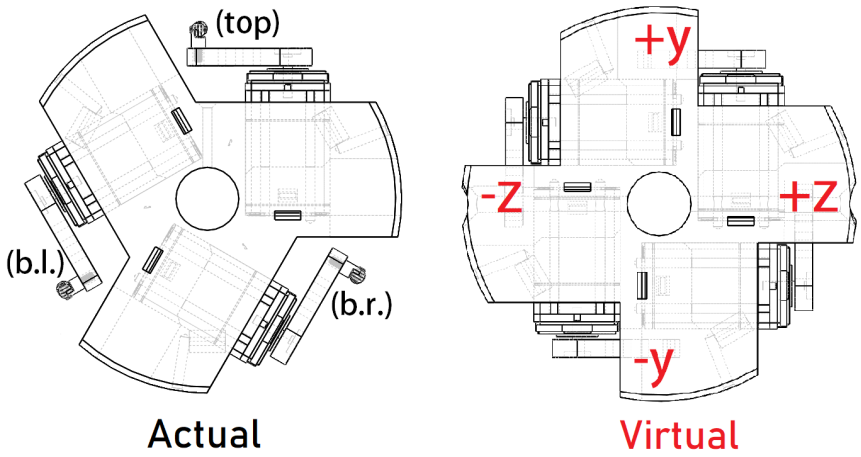

Figure 3.2. Servo alignment for swashplate actuation.

The virtual four-servo-per-rotor model greatly facilitates control-command implementation. Each servo in a rotor directly controls the pitch of blades passing through its particular quadrant, and all four servos are given the same forward offset parameter. A top servo (+y) controls the pitch of all blades passing through its (top) quadrant. A bottom servo (-y) controls the pitch of all blades passing through the bottom quadrant, while the difference between the two controls the relative thrust effort between top and bottom quadrants, thus controlling the yaw-related moment across the hull itself. The shared forward offset between these servos +y and -y directly controls the net forward thrust of all blades passing through quadrants +y and –y. When the same forward offset is applied to

all four blades, it is an adequate control for overall surge thrust, as thrust is linear with blade pitch in our angle range and can therefore be superimposed. Physical servo-arm and blade-pivot geometries are chosen for blade angles to match corresponding actuator angles in a four-servo configuration. The four-servo plate-control model is trivially realized back to the three-servo model with a simple transformation, where the three servos are labeled (top), (b.r.), and (b.l.).

$$\angle(top) = \angle(+y) \tag{3.1}$$
$$\angle(b.r.) = \frac{1-\sqrt{3}}{4}\angle(+y) + \frac{3-\sqrt{3}}{4}\angle(^{-}y) + \frac{\sqrt{3}}{2}\angle(+z)$$
$$\angle(b.l.) = \frac{1-\sqrt{3}}{4}\angle(+y) + \frac{3-\sqrt{3}}{4}\angle(^{-}y) + \frac{\sqrt{3}}{2}\angle(^{-}z)$$

where (top) represents the uppermost servo, $(b.r.)$ represents the bottom right servo, and $(b.l.)$ represents the bottom left servo in a triangular orientation. A four-servo controller would use this transformation to output appropriate values to servos in the physical three-servo model.

The four-servo-per-rotor model also allows for decoupled bi-planar control and intuitive two-dimensional Cartesian controller representation. Because all four servos are fed with the same forward offset surge-command, servos ±z can control the craft's behavior in the horizontal plane while servos ±y control the craft's behavior in the vertical plane. Furthermore, any subsequent horizontal-plane control parameter that is fed to servo +z as a value N will be fed to servo -z as the value -N. The same holds true for servos ±y. Notice how the centroid of the swash plate connecting the four servos never shifts for such control inputs, completely decoupling inputs unique to the xy plane from inputs unique to the xz plane. A two-dimensional representation can then be constructed that depicts how the vehicle behaves in the isolated xy plane. Viewing the entire hull from the side, we explore the interactions between virtual actuators ±y on the ±x rotors during different maneuvers. Fig. 3.3 illustrates the two-dimensional surge maneuver in Cartesian space.

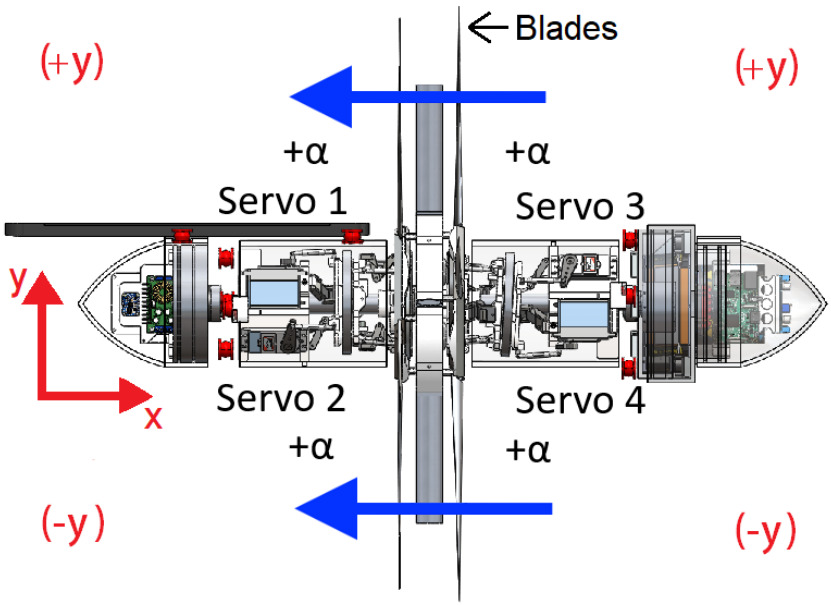

Figure 3.3. Two-dimensional surge maneuver on a full ROV implementation. Surge parameter α is fed to all servos in the proposed design, causing a positive thrust in $\hat{x}$. The resulting flow is represented with blue arrows.

Likewise, Fig. 3.4(a) illustrates the yaw maneuver in two dimensions and specifies control inputs governed by global vertical yaw parameter β. Yaw inputs -β, β, -β, and β are fed directly to servos 1, 2, 3, and 4, respectively. Control parameters can be superimposed to achieve multiple maneuvers simultaneously, as they do not inherently interfere with each other [26] due to the rigid nature of the blades. Fig. 3.4(b) details how control parameters α and β would be fed to servos 1-4 to execute two independent control modes at once.

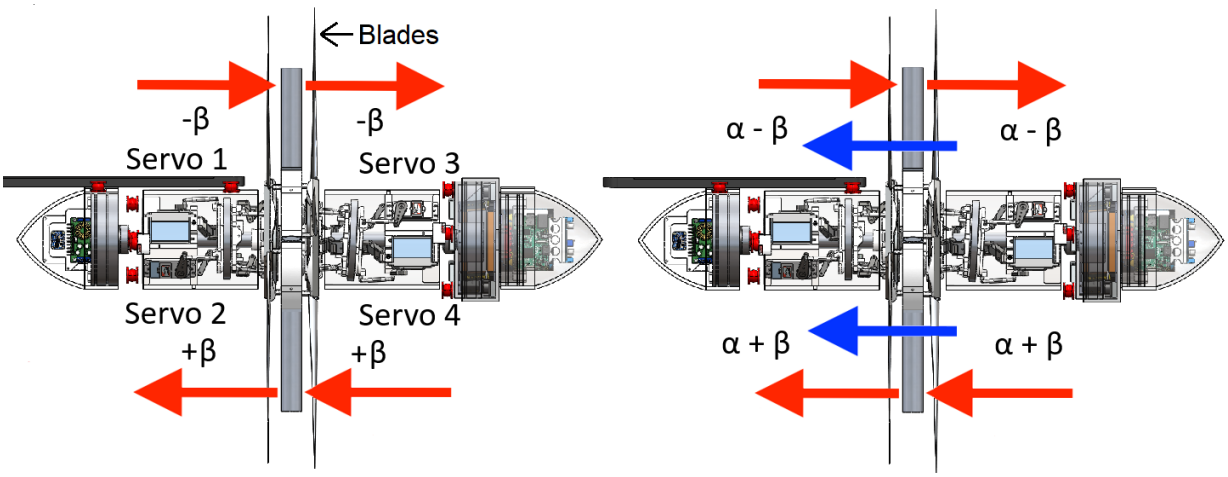

Figure 3.4. (a, left) Two-dimensional yaw maneuver on ROV implementation. (b, right) Two-dimensional superposition of yaw and surge maneuvers. Servos are fed the summation of different control parameters. Arrows conceptualize components of the fluid flow resulting from commands α and β.

A third control parameter Γ is proposed for sway. Such a maneuver is made possible from the rigid nature of the blades and durable alignment-locking of the rotor axes. As with the other planar control parameters, sway-related actuator inputs do not shift swashplate centroids, maintaining isolation between all vertical and horizontal-plane maneuvers. The lack of kinematic overlap allows for superposition of *all* control parameters, as they do not fundamentally interfere with each others' functionality [26]. Fig. 3.5 elaborates the principle behind the sway maneuver mechanism.

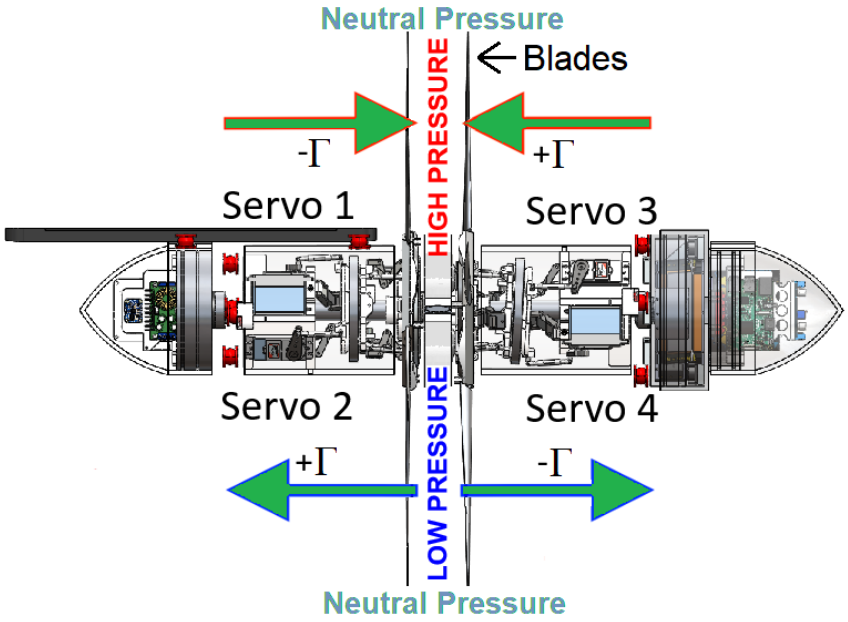

Figure 3.5. Two-dimensional sway maneuver on ROV implementation. Sway parameters -Γ, Γ, Γ, and -Γ are added to servo inputs 1, 2, 3, and 4, respectively.

Flow leakage between the high and low pressure regions would reduce sway thrust. The issue regarding unwanted flow across the pressure differential in the sway maneuver is presented and solved in Fig. 3.6.

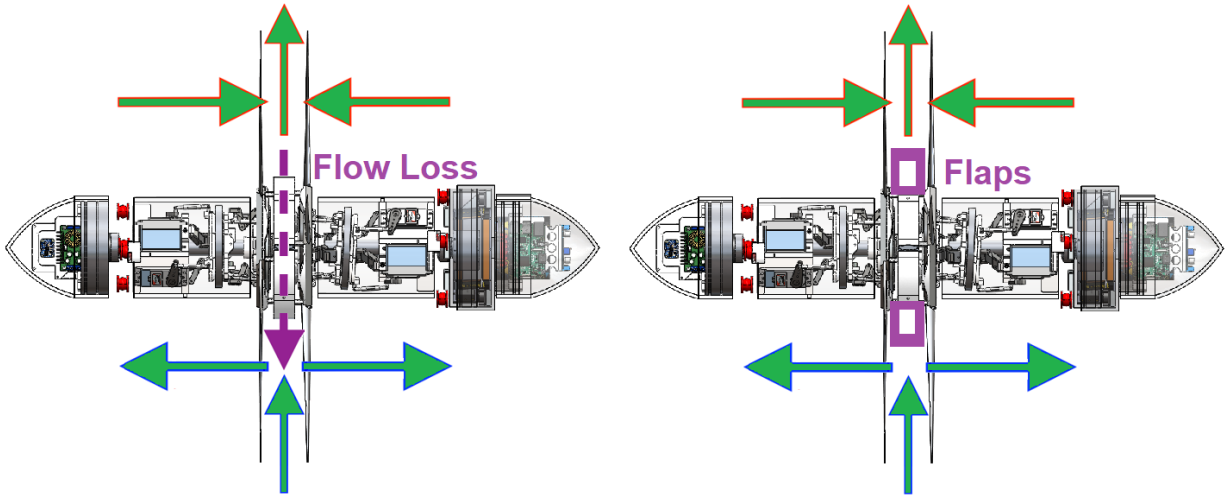

Figure 3.6. Flow loss due to pressure differential across space between rotors. Unwanted flows are minimized through the *BARFA* flaps described in Section 3.2.2.

Final inputs to virtual servos 1-4 are then respectively α-β-Γ, α+β+Γ, α-β+Γ, and α+β-Γ. We set $\alpha \in (-10^o, 10^o)$, $\beta \in (-10^o, 10^o)$, and $\Gamma \in (-10^o, 10^o)$ such that $|\alpha+\beta+\Gamma| < 30^o$, the physical control limit of each servo. Servo arm and blade pivot lengths are chosen to match blade angles with servo angles in corresponding quadrants.

Rotors are decoupled from one-another to allow for simple roll control via torque-balancing. Because the effective input to each *loaded* rotor is torque, not speed [41] (as with many programmable torque-oriented RC-car ESCs which utilize back-EMF in rotor-stator phase estimation to prevent skipping, like those in this mechanism), roll-torque remains balanced regardless of blade parameters and relative speed, as rotation rate is simply a byproduct of the torque input. This allows for roll control via a single parameter δ, effectively decoupled from all other parameters and realized merely by varying the relative effort between the two rotors. The separate rotors are read 90% effort $\pm\delta$, where $\delta \in (-10\%, 10\%)$. Control parameters are then mapped to physical actuator commands as follows:

$$\begin{bmatrix} +x \text{ Rotor Effort} \\ -x \text{ Rotor Effort} \\ +x \text{ ``top'' Servo Angle} \\ +x \text{ ``b.r.'' Servo Angle} \\ +x \text{ ``b.l.'' Servo Angle} \\ -x \text{ ``top'' Servo Angle} \\ -x \text{ ``b.r.'' Servo Angle} \\ -x \text{ ``b.l.'' Servo Angle} \end{bmatrix} = \begin{bmatrix} 90\% \\ 90\% \\ 90^o \\ 90^o \\ 90^o \\ 90^o \\ 90^o \\ 90^o \end{bmatrix} + \begin{bmatrix} 0 & 0 & 0 & -1 & 0 & 0 \\ 0 & 0 & 0 & 1 & 0 & 0 \\ 1 & 0 & -1 & 0 & 0 & -1 \\ 1 & \frac{\sqrt{3}}{2} & \frac{1}{2} & 0 & -\frac{\sqrt{3}}{2} & \frac{1}{2} \\ 1 & -\frac{\sqrt{3}}{2} & \frac{1}{2} & 0 & \frac{\sqrt{3}}{2} & \frac{1}{2} \\ -1 & 0 & -1 & 0 & 0 & 1 \\ -1 & -\frac{\sqrt{3}}{2} & \frac{1}{2} & 0 & -\frac{\sqrt{3}}{2} & \frac{-1}{2} \\ -1 & \frac{\sqrt{3}}{2} & \frac{1}{2} & 0 & \frac{\sqrt{3}}{2} & \frac{-1}{2} \end{bmatrix} \begin{bmatrix} \alpha \\ \Gamma_y \\ \Gamma_z \\ \delta \\ \beta_y \\ \beta_z \end{bmatrix} \tag{3.2}$$

where Γ_y and Γ_z respectively control force along $\hat{y}$ and $\hat{z}$, while β_y and β_z respectively control moment about $\hat{y}$ and $\hat{z}$. Fig. 3.7 shows how the blades alter pitch during their sweep about $\hat{x}$, in response to each superimposable control parameter.

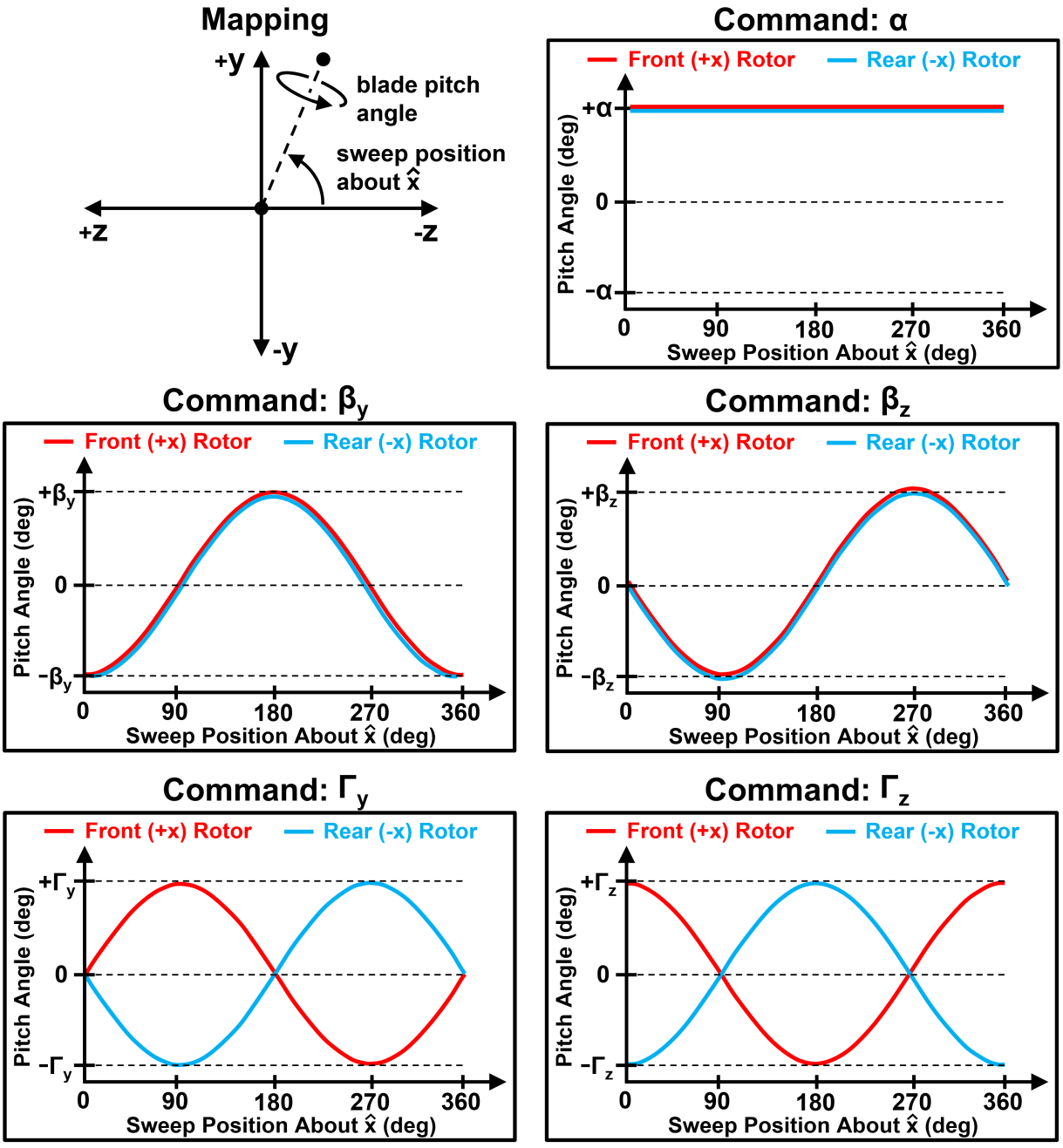

Figure 3.7. Blade pitch angles throughout sweep about $\hat{x}$.

It is important to note that the conceptual validation of roll, surge, and yaw maneuvers was determined to have lesser relevance in testing practicality of the proposed mechanism. For example, in no reasonable scenario will pulling *all* blade pitches forward *not* cause the craft to surge as intended if properly programmed with servo limits considered. Yaw

and roll control parameters are similarly straightforward. These maneuvers are practically identical to the operational foundation of all dual-blade rotorcraft [26]. The omnidirectionality of the proposed mechanism comes from its unique ability to potentially *sway* quickly, allowing it to move in any orientation at speeds far beyond the scope of ROVs or AUVs. STARCCM+ computational fluid dynamic (CFD) simulations suggest the propulsor can generate sway thrust at a magnitude near 10-20% surge thrust capability [33]. A small-scale physical model is then constructed to both validate the dynamic omnidirectional thrust ability of the craft, and gauge the feasibility of the novel sway maneuver as a principle.

3.2 Small-Scale Model Design

A small-scale force-validation model was constructed to verify the conceptual working principles. The model was designed to be tested in a water tank while fixed to an off-axis, six-DOF force-sensing apparatus placed above the tank. The experimental testing tank setup is outlined in Fig. 3.8.

3.2.1 Force-Sensing Apparatus

The force-sensing apparatus is designed and fabricated using 80/20 aluminum bars to measure any forces and moments imposed by the attached propulsor at a depth of 0.3m in bullard pull. The economical design relies on six strategically placed tension sensors and bearings to discern between the different forces and moments, as elaborated in Fig. 3.9.

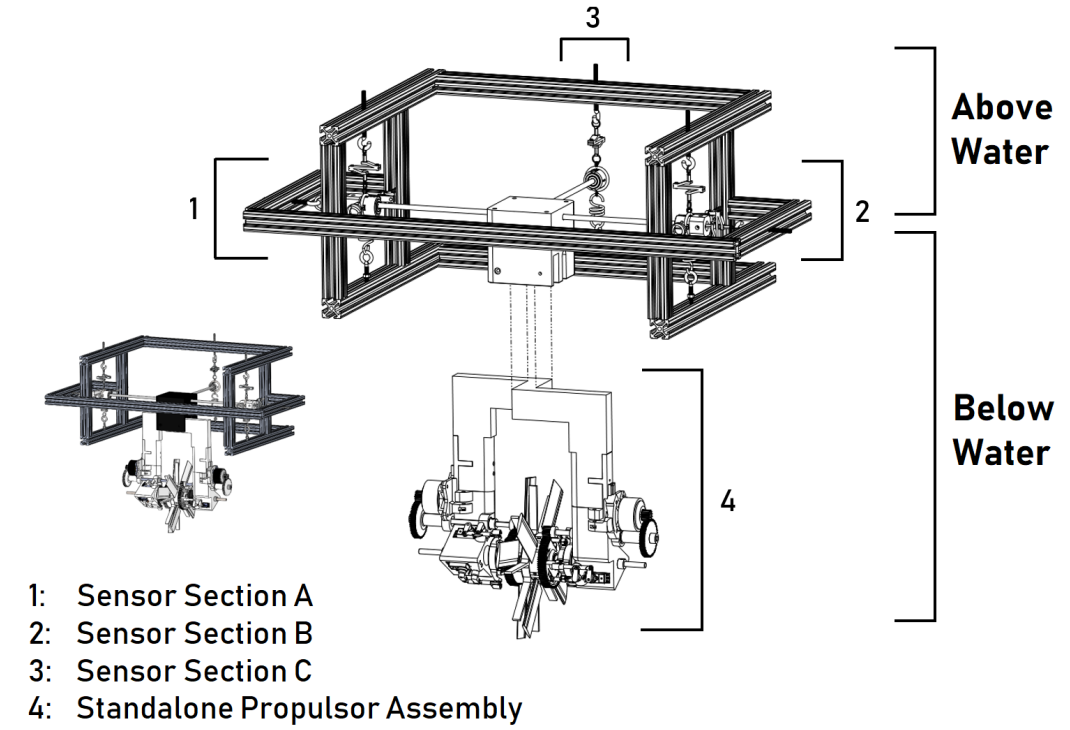

Figure 3.8. Test setup of the small-scale model.

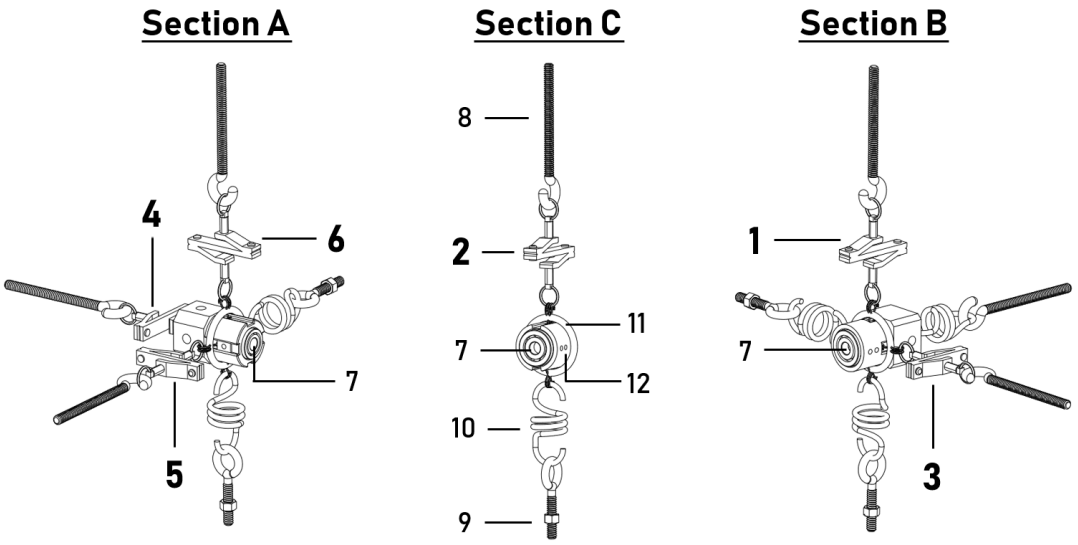

Figure 3.9. Sub-components of the force-sensing apparatus for the small-scale model. Bearings are positioned to facilitate small-angle exploits in force estimation.

With the three sections under high tension, small-angle deflection principles are exploited to discern between the different forces and moments on its attached off-axis propulsor. Fig. 3.10 illustrates how the forces and moments (F_x, F_y, F_z, M_x, M_y, M_z) generated by the propulsor are linked to the linear forces (f_1, f_2, f_3, f_4, f_5, f_6) measured by the tension sensors.

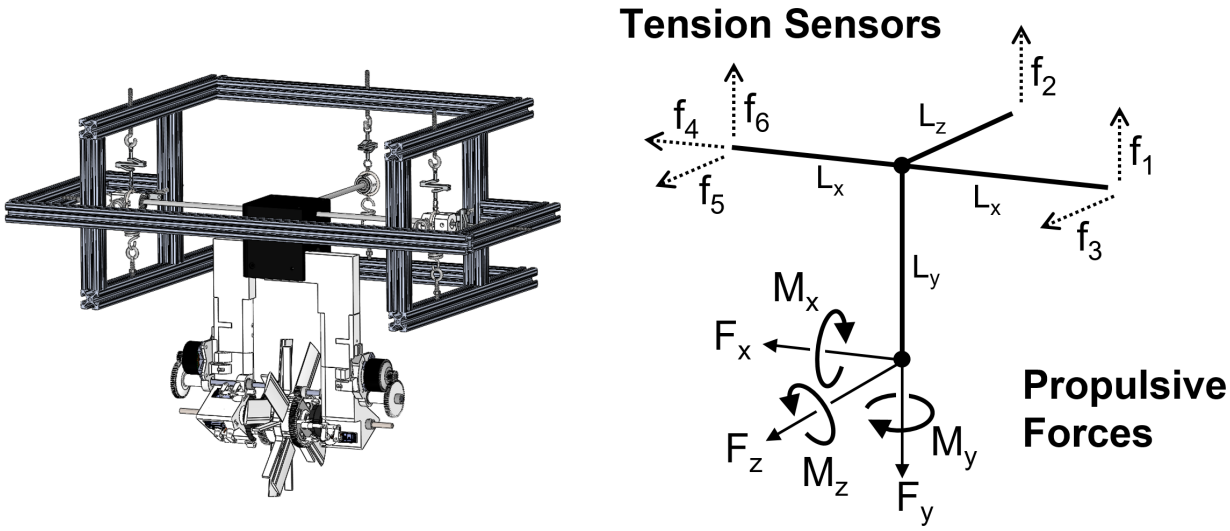

Figure 3.10. Force-sensing apparatus tension mapping and configuration. Lengths L_x, L_y, and L_z are measured to be 0.2387m, 0.225m, and 0.2675m, respectively.

Forces and moments (F_x, F_y, F_z, M_x, M_y, M_z) generated by the propulsor are then mapped to linear forces (f_1, f_2, f_3, f_4, f_5, f_6) detected by the tension sensors as follows:

$$
\begin{aligned}
F_x &= f_4 \\
F_y &= -f_1 - f_2 - f_6 \\
F_z &= f_3 + f_5 \\
M_x &= -L_z f_2 \\
M_y &= L_x f_3 - L_x f_5 \\
M_z &= L_x f_1 - L_x f_6 + L_y f_4
\end{aligned}
\tag{3.3}
$$

3.2.2 Small-Scale Propulsor Assembly

An overview of the standalone small-scale propulsor assembly is shown in Fig. 3.11.

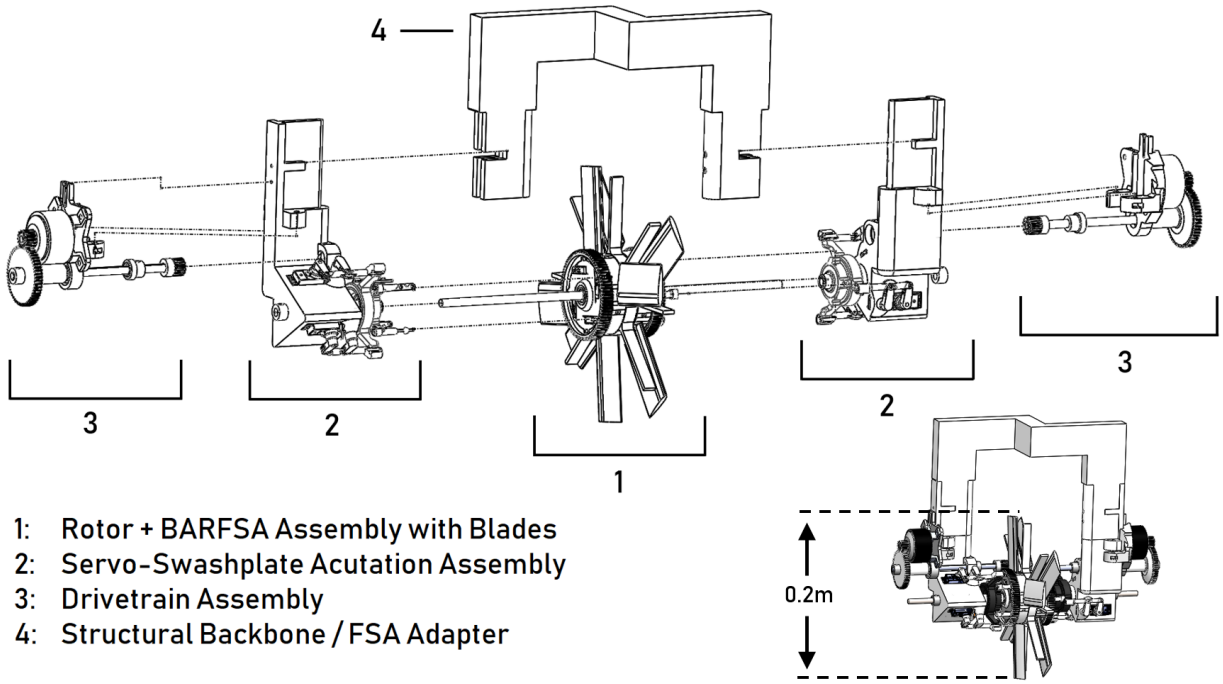

Figure 3.11. Subcomponents of the small-scale propulsor.

Because the small-scale force-validation model is never intended to physically accelerate, the overall design process is simplified, allowing the small-scale model to be economical and predominantly 3D-printed without mass-related limitations. Design emphasis is now focused primarily on clearing space around the rotating blades rather than compacting and streamlining the entire subassembly area. Unlike in the full-scale model, small-scale subassemblies are then encouraged to be placed much further from the dynamic rotors, greatly simplifying the design as a whole.

Drivetrain and Rotor Mechanism

In the drivetrain mechanism, for example, the motors and obtrusive gears are as far away from the dynamic rotors as possible so as to not disrupt the generated forces and moments. The drivetrain must provide independent torque to each rotor while locking relative rotor alignment and be able to support the stationary flaps responsible for limiting unwanted flow. Fortunately, geometric exploits allow for a relatively simple design solution. An engineering diagram of the entire drivetrain mechanism is shown in Fig. 3.12.

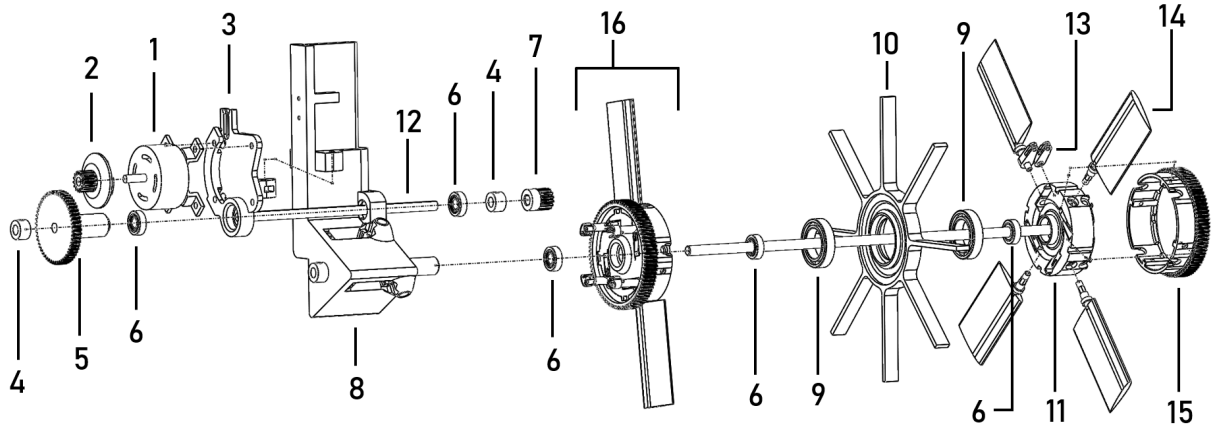

Figure 3.12. Small-scale drivetrain and rotor assembly.

The drivetrain on each rotor is powered by a Hobbyking ST3508-730kv brushless motor. These inexpensive motors are chosen for their exceptional torque, power, size, and material-based bearing design which allows for corrosion resistance uncommon for motors of their

size. Their significant torque output (≥1.1 N-m stall) is aided by a further 15:1 gear reduction in the drivechain. With the rotors spanning only 0.2m total diameter, we expect minimal rotation rate loss due to the drag from the blades alone. Fluid compression and churning losses on the submerged gearing [14, 12], especially at the motor location, are expected to have the largest influence on rotation rate drop.

Many of the parts in or near the motor housing are not exceptionally rigid, raising concerns for potential gear slipping. A solution for slipping is implemented which firmly compresses all gears in the drivetrain onto one-another. Fig. 3.13 elaborates the gear-slip solution through a cut-out of the completed drive assembly.

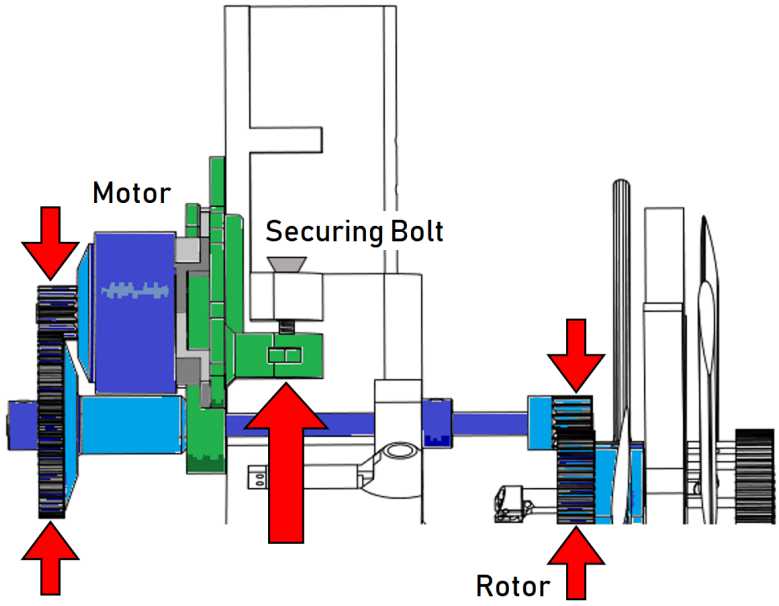

Figure 3.13. Anti-slip solution via intentionally misaligned driveshaft. 3D printed gears are shown in light blue, while metal parts are shown in dark blue. The motor housing (green) slides vertically, allowing a single bolt to re-orientate the driveshaft and thoroughly compress all gear linkages in the drivetrain.

To prevent unwanted physical blade interactions, rotors are locked in alignment about their respective axes through the blade-axis re-enforcing flap adapter (BARFA). The BARFA allows the rotors to push against one-another without touching, and contains the station-

ary blades responsible for reducing unwanted flow (Fig. 3.6) during the sway maneuver. Fig. 3.14 highlights the BARFA mechanism used in the small-scale model.

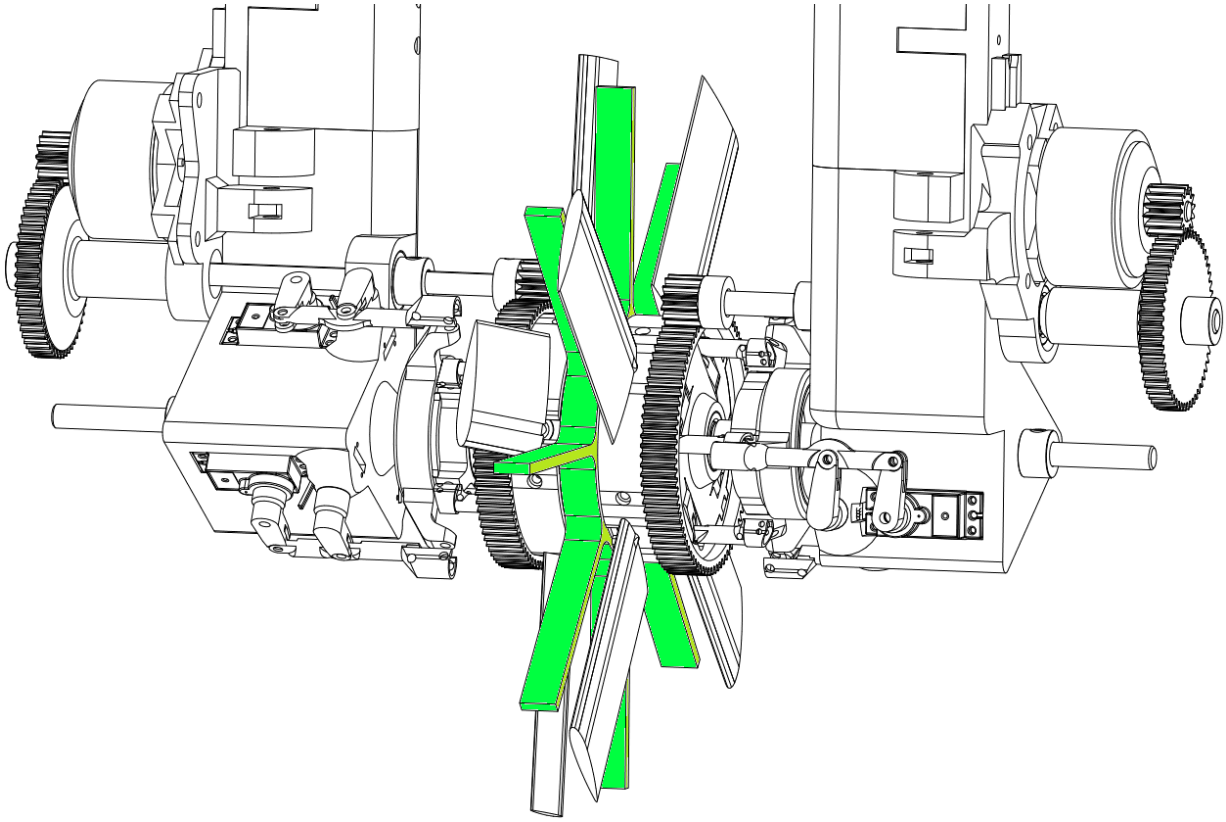

Figure 3.14. The BARFA mechanism for eliminating unwanted fluid flow and securing rotor alignment (highlighted).

Servo-Swashplate Actuation Mechanism

The servo-swashplate actuation mechanism (SSPAM) must quickly and accurately manipulate the pitch of spinning blades in a manner independent of rotation rate, as discussed in Section 3.1. The design consists of two SSPAM assemblies. Each SSPAM links a set of three Savox SW0250MG waterproof servos to four blades through a swashplate mechanism.

All blades must remain phase-locked with the swashplate to allow the swashplate to both pull and push on blade pivots. To ensure blade-swashplate phase-alignment, blade pivot arms are arranged as four-bar linkages to lock their alignment with the primary hull axis. Fig. 3.15 projects an expanded SSPAM assembly in its entirety.

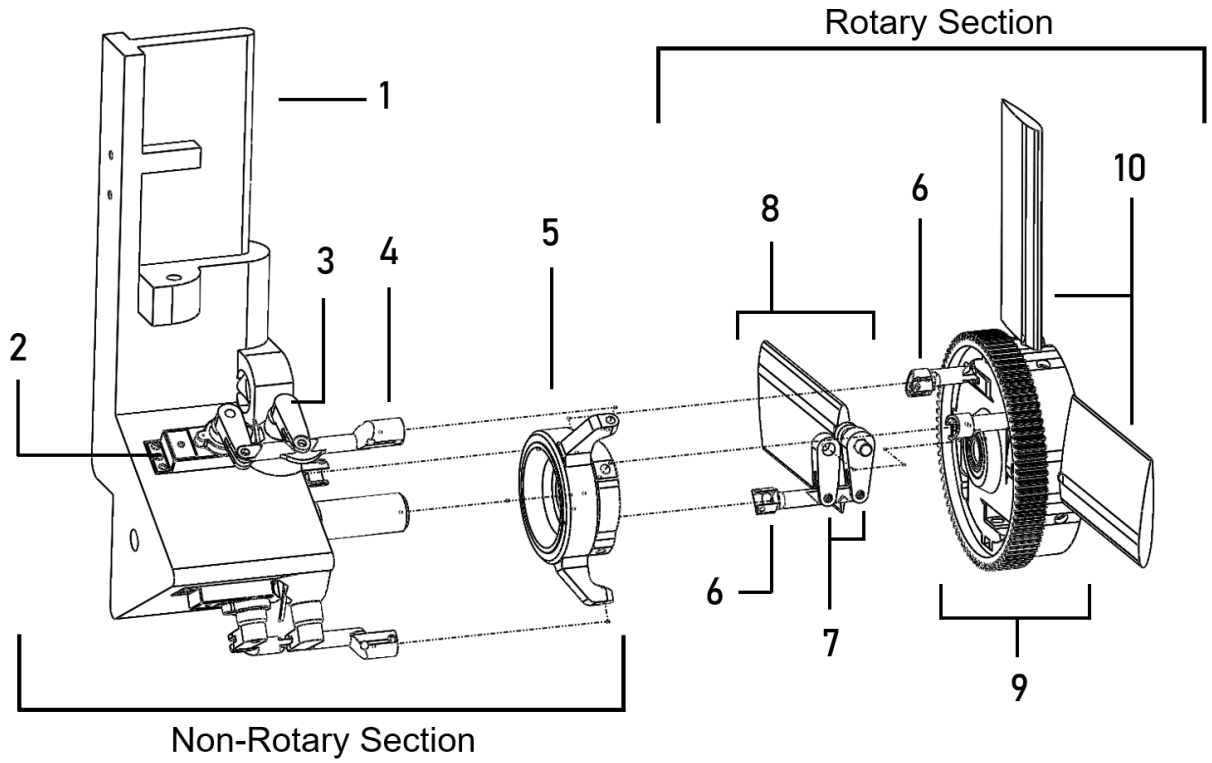

1. Servo Housing
2. SW 0250MG Waterproof Digital Servos
3. Servo-Swashlate Phase-Lock Hinges
4. Servo-Swashplate Linkages
5. Trex 700E CCPM Swashplate
6. Rotor-Swashplate Linkages
7. Dynamic Blade Actuation Arms and Arm Supports
8. Dynamic Blade 4-bar Linkages for Swashplate Phase Lock
9. Single Rotor
10. Dynamic Blades (3 of 8 shown)

Figure 3.15. Small-scale actuation mechanism assembly.

3.2.3 Electronic Setup

An economical Arduino-based setup is constructed which routes isolated power to appropriate subsystems while remaining simple and safe to operate. The setup is powered by a 4s LiPo battery feeding directly to the two main ESCs, as well as to three separate Buck converters which independently provide power to the servos and a central Arduino MEGA 2560. Fig. 3.16 details the electrical layout.

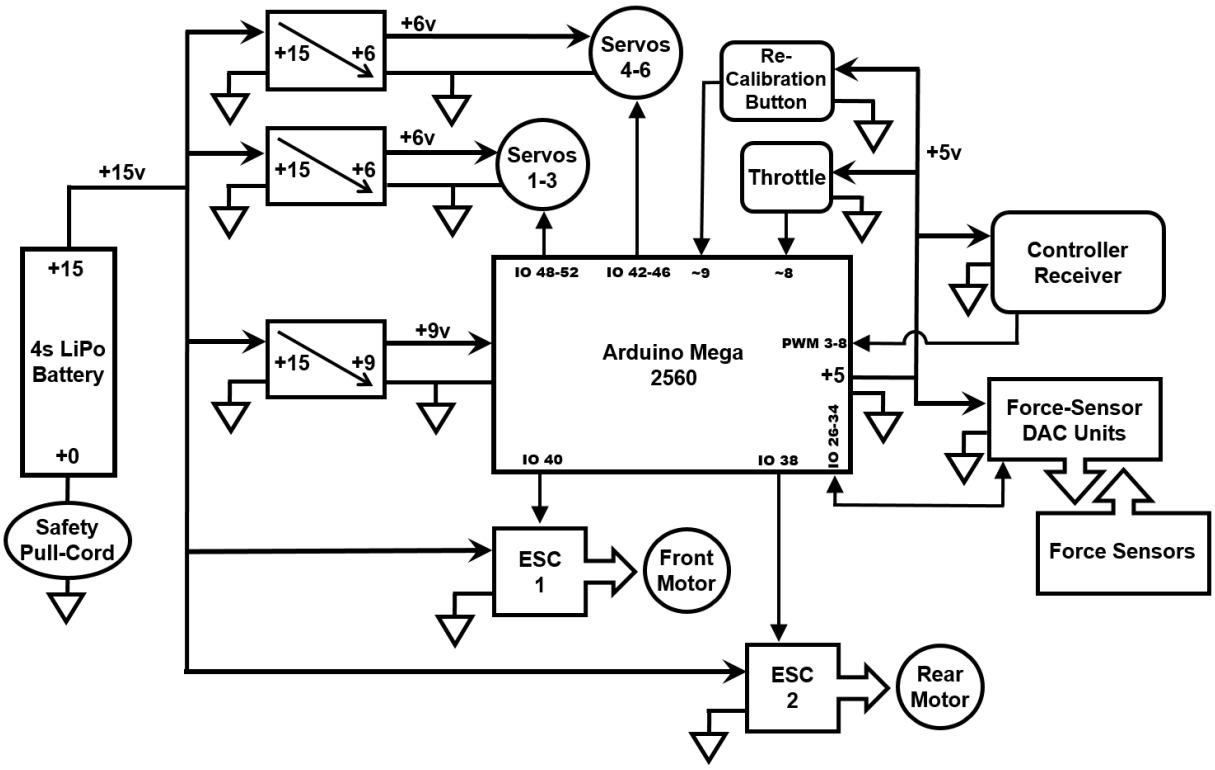

Figure 3.16. Layout of electronics used in experimentation.

As a first level of safety against a runaway propulsor, the Arduino's throttle command is read from an analog voltage divider that is itself powered by the Arduino. If at any point the analog throttle signal is lost or disconnected while the Arduino is operating correctly, the motors will shut down. As a final level of safety against any malfunction, the setup contains a killswitch pullplug located on the battery's ground lead, which can be pulled

from a safe distance to reliably cut power to all systems.

The Arduino reads and reports values from the force-sensing apparatus while also controlling the actuators and brushless ESCs. Control mode commands α, Γ_y, Γ_z, δ, β_y, and β_z are interpreted from PWM inputs from an external controller. The Arduino's single-threaded nature prohibits it from simultaneously executing these control mode commands while reading force sensors. Due to the required cool-down time between force-sensor readings, the Arduino's operating loop must update actuator commands every iteration, while only reading from force sensors every fourth iteration. The Arduino then reports the last known sensor readings on iterations between updates. This may cause small illusory input-output delays between control mode commands and sensor readings, but is extremely cost effective- maximizing recorded data with inexpensive hardware. Illusory delays can be upwards of 0.2 seconds.

3.3 Experimental Results and Analysis

At various motor efforts, different control commands are tested and compared against measured forces to gauge validity of the operating theory. Control commands are physically manifested as pitch changes onto the moving blades. Design geometries ensure that the magnitude of respective pitch change is directly proportional to the magnitude of control command change. For the Wortmann FX 76-100 hydrofoil blade profile used in the mechanism, lift forces generated are linear with blade angle of attack (AoA), hence with pitch and therefore control commands, until around 15^o AoA [49]. Even as the actuators rotate to achieve 15^o pitch, the increasing fluid inflow velocity decreases the effective AoA on the blades. In turn, the linear pitch regime is actually expanded beyond 15^o and is expected to encompass the full operating range of the servos. Control commands may then be pushed well past their normal $(^-10^o, 10^o)$ restrictions during signal-maneuver tests, but should still

be selectively limited to maintain force-command linearity.

Due to safety concerns, motor effort is never brought past 50% during our study. The brushless motors still operate under some hydrodynamic load, so direct motor effort commands to ESCs are expected to manifest more as torque than speed inputs [19]. Because generated rotor forces are typically linear with torque [50], we can expect forces generated from any particular command to also be linear with motor effort.

3.3.1 Pure Surge (α)

The surge-force F_{surge} generated from the surge command α, for example, should then take the form

$$F_{\text{surge}} = \text{K}_\alpha(\text{Motor Effort - Motor Offset}) \cdot \alpha \tag{3.4}$$

where K_α is a scaling factor that links command α to the output force F_{surge} and encompasses all constant unknown hydrodynamic and motor-rate properties. Motor Effort describes the throttle command percent read to the ESCs and imposed on the rotors, while Motor Offset describes the smallest value at which the ESCs actually spin the motors. For the small-scale model, the Motor Offset value is expected to be around 13% effort.

At various motor efforts, different magnitudes of command α are tested and surge forces are recorded. These forces are normalized by their corresponding α commands and plotted against motor effort. To validate the form of (3.4) and our operating principles as a whole, the plot should reveal a clear linear trend between normalized forces and motor efforts, with an x-axis crossing at around 13% motor effort. Normalized surge forces are plotted against motor effort in Fig. 3.17.

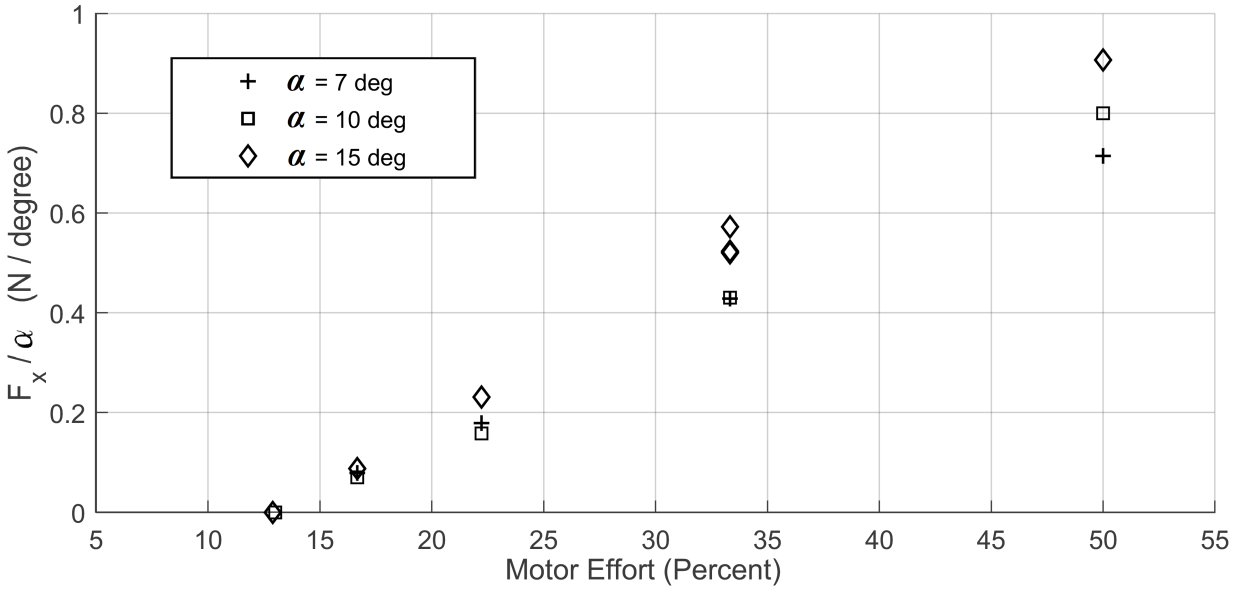

Figure 3.17. Surge forces normalized by α at various motor efforts.

The surge force model hypothesis is clearly validated in Fig. 3.17, with $K_\alpha = 2.37E^{-2}$. We can expect the small-scale propulsor to generate around 32N thrust at 100% motor effort for surge ($\alpha = 15^o$). For completeness, results from a pure-surge test with 15^o step commands at various motor efforts are presented in Fig. 3.18.

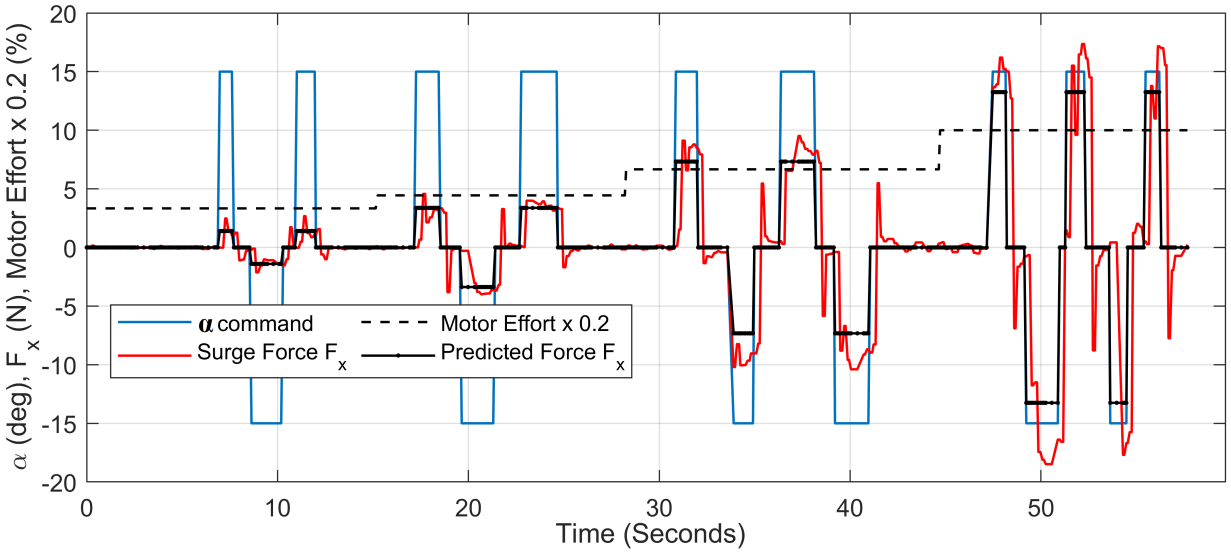

Figure 3.18. Pure-surge forces with $\alpha \pm 15^o$ at 16, 22, 33, and 50% motor effort.

As explained in Section 3.2.3, perceived delays between input-commands and output-forces in Fig. 3.18 are caused primarily by force-sensor update lag. The process of thoroughly deducting the cause of the perceived lag is fairly straightforward. With everything considered, it is understood that the perceived 200ms+ delays are caused by some combination of any or all of the following possible sources:

1. The material flexibility of the apparatus somehow causing a measurable delay between force generation and sensor readings.

   The force sensing apparatus is tightly coupled to the propulsor, but with small yet nonzero flexibility. The flexibility is emergent from the springs and finite rigidity of all components in the assembly. Any delays between the chassis deflection and tension near the gauges would thereby be defined only through speed of sound of the assembly components: ABS and steel. The speed of sound in ABS is 2200m/s, while the speed of sound of steel is approximately 6000m/s. Steel spans most of the 0.4m distance to the gauges. Even if assuming all ABS, mechanical flexibilities would at worst cause delays of less than 1ms, far outside the range of the delays observed.

2. The overall Arduino single-threaded loop delays, composed of:

   (a) Calculation, controller read, and servo/ESC/serial write times (∼80-120ms)

   (b) Tension sensor reading delays (∼100ms, once every 2 iterations)

   (c) Tension sensor cool-down delays (∼500-600ms, once every 32 iterations)

   By observing the overall operating loop times and delays between samples in Fig. 3.19, this proves to be a decisive culprit for the delays shown between force sensor readings and input commands from Fig. 3.18.

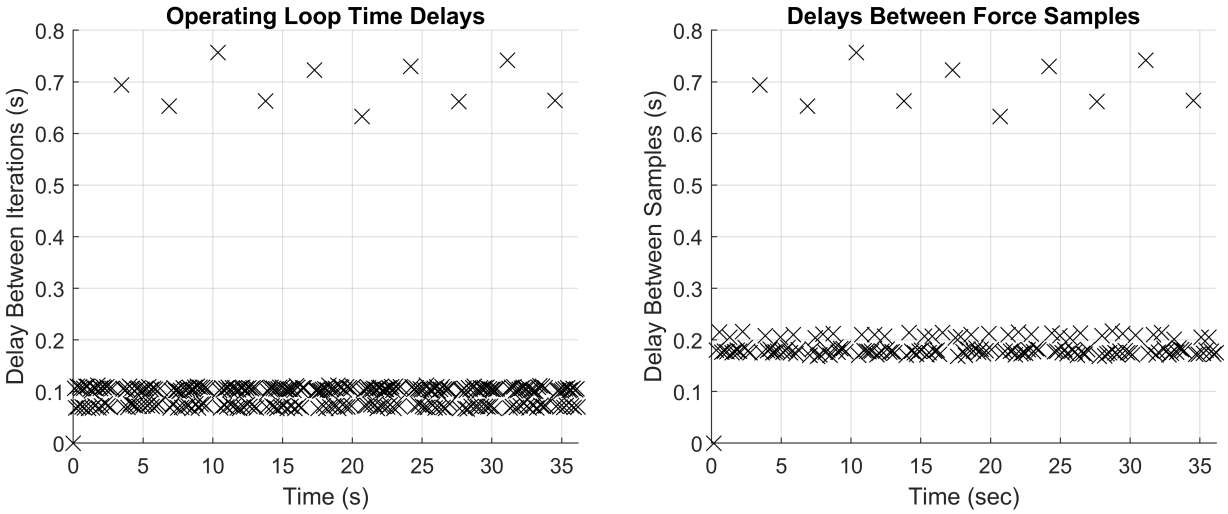

Figure 3.19. Operating loop and sample-time delays during a pure-alpha test.

3. Hydrodynamic delays between actuation onset and force output, which could undermine the operating theory.

   This possibility is already negated by the measured forces lingering for the same amount of time as the onset delay, which is not possible hydrodynamically. To further investigate and eliminate this potential cause, we recognize that the attached propulsor must physically deflect a small amount before the sensors can generate readings, which can be exploited to analyze the propulsor's true reaction time using slow-motion capture. The start time is taken at the instant the servos start moving. Any hydrodynamic force delays are shown to be less than even the 20ms rise-time of the pitch-actuating servos through slow-motion analysis, as presented in Fig. 3.20. Deflection of the chassis is understood to coincide directly with actual sensor tension via Hooke's law.

Therefore, the lag exemplified in Fig. 3.18 can decisively be reduced to delays caused by the electronic setup, and not the mechanism itself. These are loosely referred to as "software" delays.

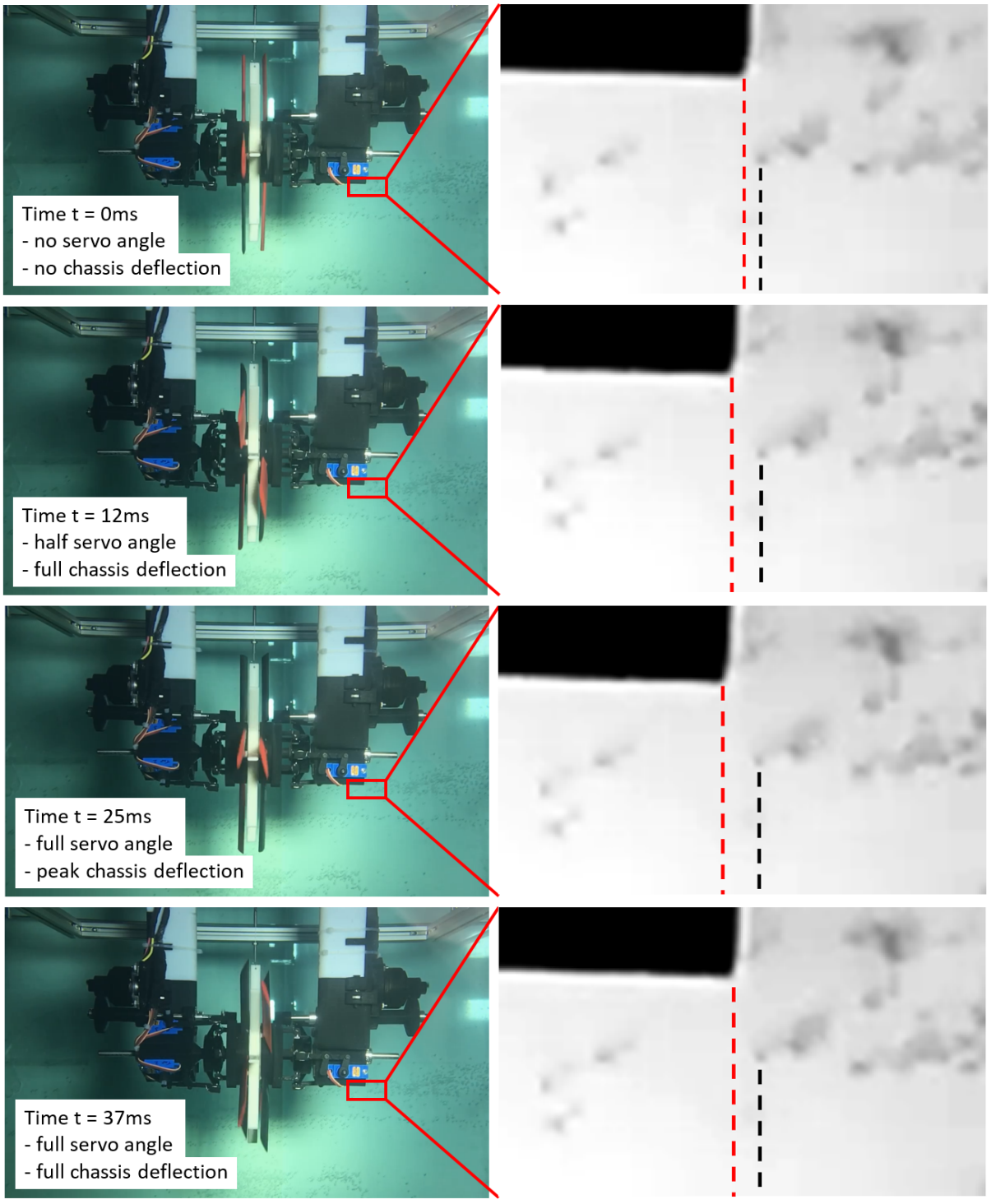

Figure 3.20. Slow-motion analysis on chassis deflection for gauging true input-output time delay. Imperfections in testing tank glass are used for relative unitless position.

3.3.2 Yaw (β)

Both kinematically and hydrodynamically, the yaw maneuver is understood to be very similar to the surge maneuver. While the surge maneuver generates surge force, the yaw maneuver similarly generates yaw moment. The lack of moment-arm due to the limited rotor span on the small-scale model greatly reduces the magnitude of moments measured, but this is understood. For the purposes of this study, the yaw maneuver need only be tested for existence and shown to be decoupled between the two different yaw-axes. Simultaneous β_y and β_z maneuvers are shown to be achievable and decoupled in Fig. 3.21. The test was conducted with 33% motor effort at β magnitudes of only $\pm 10^o$.

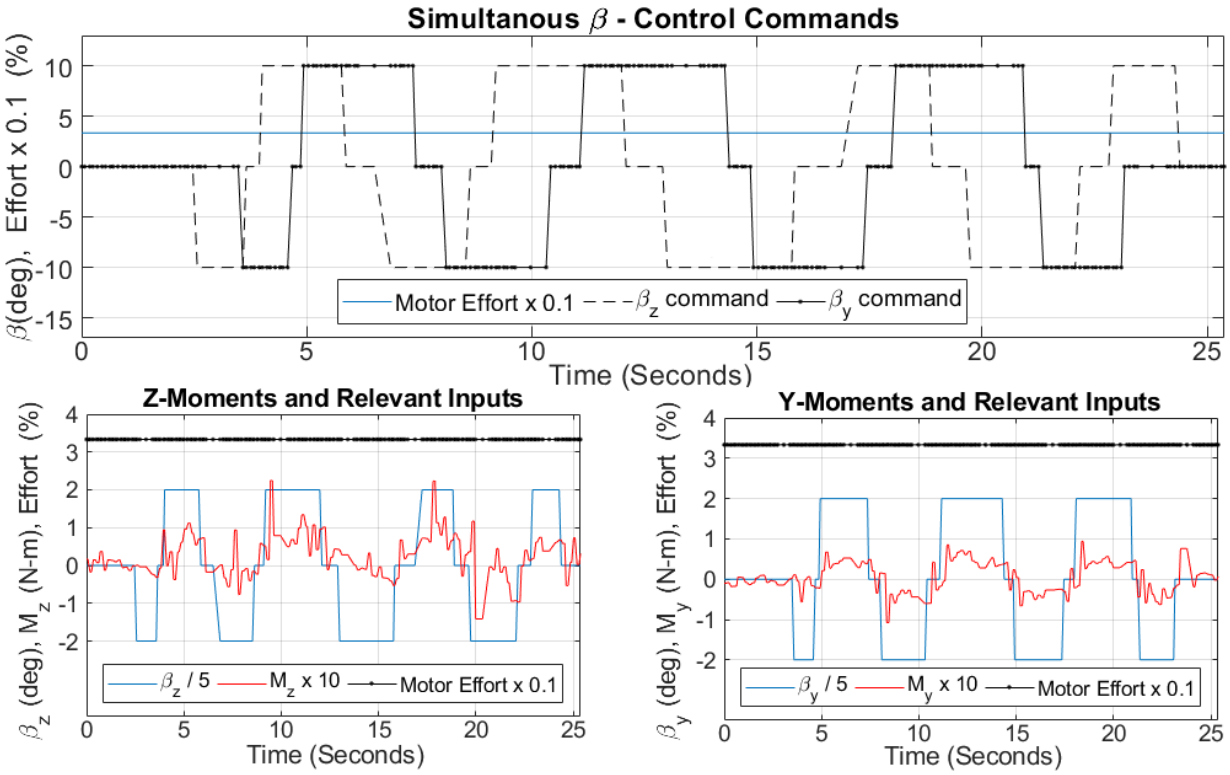

Figure 3.21. Simultaneous mixed-yaw forces with $\beta \pm 10^o$.

The yaw maneuver is already understood to be kinematically and hydrodynamically similar to the pure-surge maneuver and behave accordingly, so for the purposes of this study, the yaw maneuver need only be tested for existence and shown to be decoupled between the two different yaw-axes. Furthermore, due to the lack of moment-arm on the blade span, yaw-moments generated are also understood to be small in magnitude, providing a level of difficulty in accurate measurement. Recall that during signal-maneuver tests, control-commands may be pushed well past their normal $(-10^{o}, 10^{o})$ restrictions initially set to prevent servo-range saturation by allocating space for other maneuvers. As such, a pure-yaw test is run with β_z-step commands exceeding 10^{o} in magnitude for a somewhat cleaner input-output mapping. For completeness, data from a single-axis pure-yaw test with 20^{o} β_z-step commands at 33% motor effort is presented in Fig. 3.22.

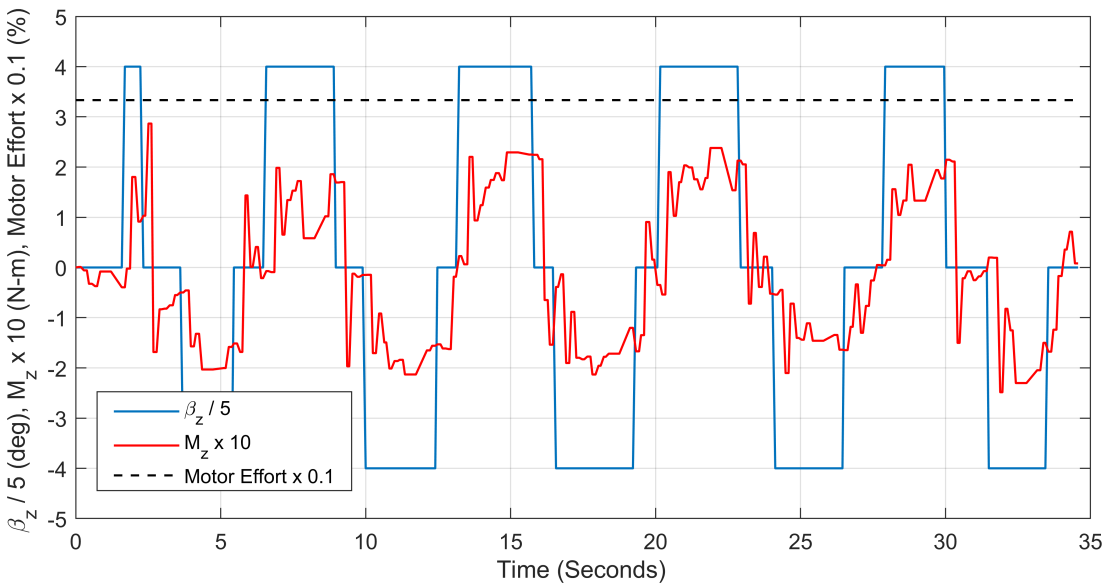

Figure 3.22. Pure-yaw forces with $\beta_z \pm 20^{o}$.

3.3.3 Sway (Γ)

One of the primary objectives of this study is to gauge the validity of the novel sway maneuver principle. Our current model assumes the force response to sway behaves in a similar manner to surge. Like surge, the sway-force F_{sway} generated from sway command Γ should scale as

$$F_{\text{sway}} = \text{K}_\Gamma(\text{Motor Effort - Motor Offset}) \cdot \Gamma \tag{3.5}$$

where K_Γ is a scaling factor which links sway-command Γ to the output force F_{sway} and encompasses all constant unknown hydrodynamic and motor-rate properties. For the small-scale model, the *offset* value is expected to be around 13% effort.

At various motor efforts, different magnitudes of command Γ_{y} are tested and sway forces F_{y} are recorded. These forces are normalized by their corresponding Γ_{y} commands and plotted against motor effort. To validate the form of (3.5) and our operating principles as a whole, the plot should reveal a clear linear trend between normalized forces and motor efforts, with an x-axis crossing at around 13% motor effort. Normalized sway forces are plotted against motor effort in Fig. 3.23.

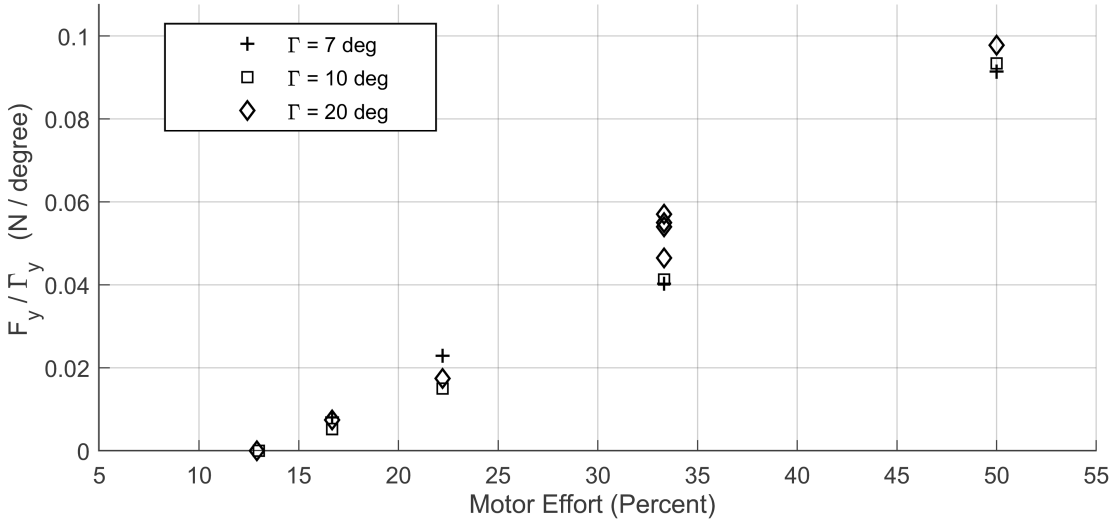

Figure 3.23. Sway forces normalized by Γ at various motor efforts.

The sway force model hypothesis is clearly validated in Fig. 3.23, with $K_\Gamma = 2.67E^{-3}$. The model predicts the small-scale propulsor to generate around 4.6N at 100% motor effort for sway ($\Gamma = 20^o$). For completeness, results from a pure-sway test with 20^o step commands at various motor efforts are presented in Fig. 3.24.

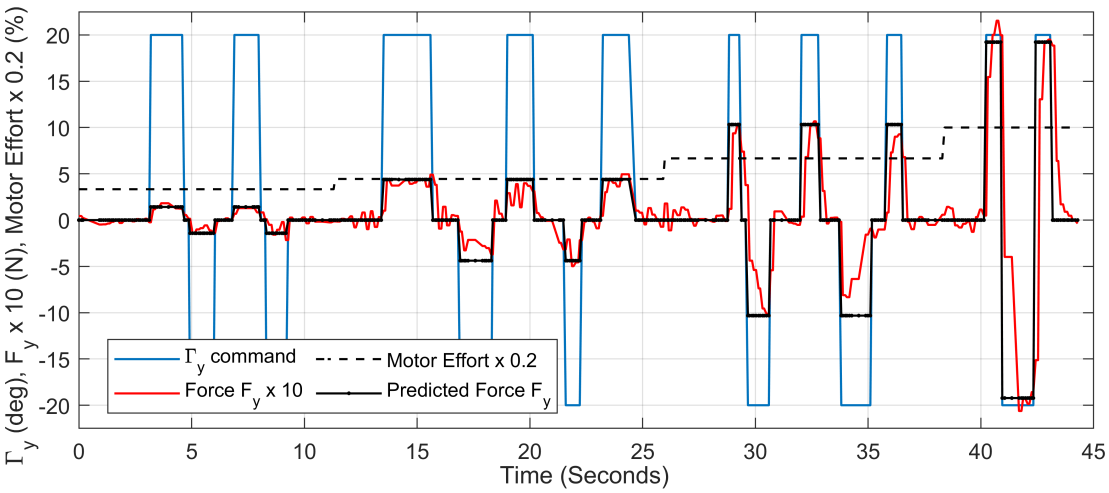

Figure 3.24. Pure-sway forces with $\Gamma_y \pm 20^o$ at 16, 22, 33, and 50% motor effort.

Simultaneous Γ_y and Γ_z maneuvers are shown to be achievable and decoupled in Fig. 3.25. The test was conducted with 33% and 50% motor effort at Γ-command magnitudes of only $\pm 10^o$.

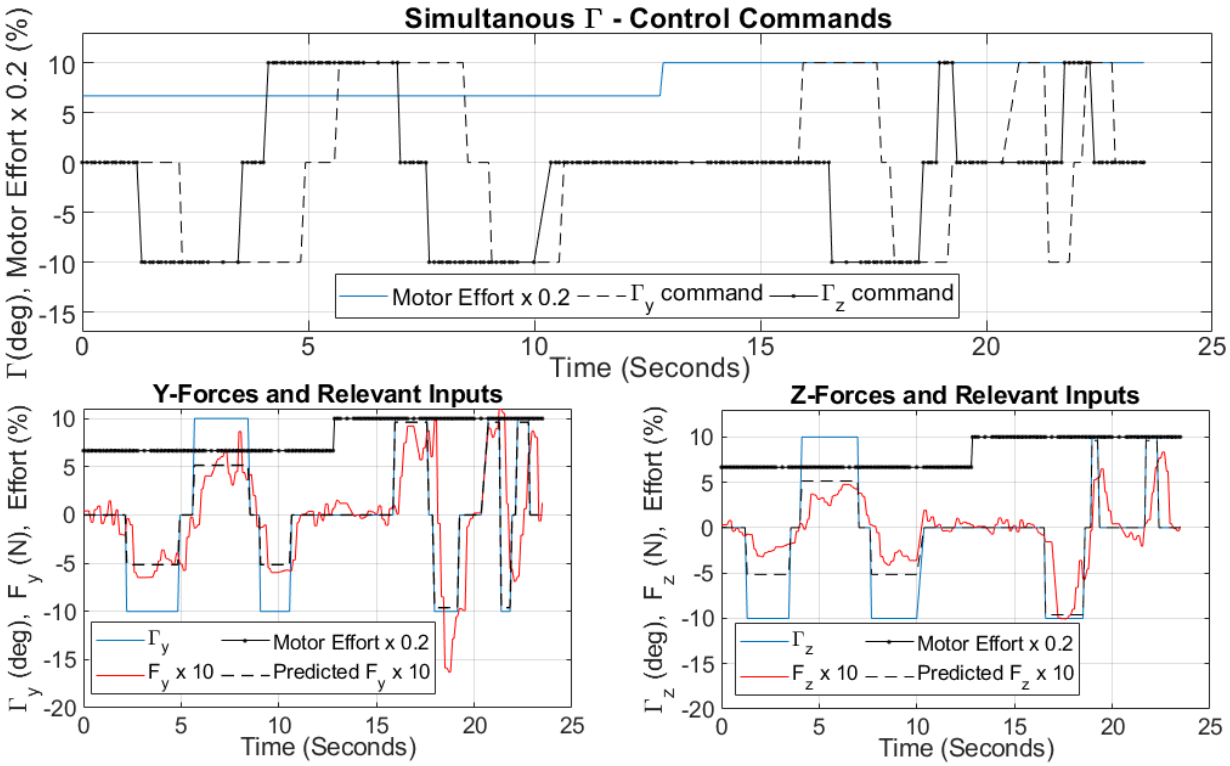

Figure 3.25. Simultaneous mixed-sway forces with $\Gamma \pm 10^{o}$.

3.3.4 Control-Command Interactions

Control command combinations (α, β), and (β, Γ) are tested and confirmed to be decoupled. Testing of the combination (α, Γ) reveals some cross-planar coupling, which can be explained through blade drag analysis and then compensated for in a straightforward manner. Forces from an $\alpha + \Gamma$ test are presented in Fig. 3.26 which show the unwanted cross-planar interference.

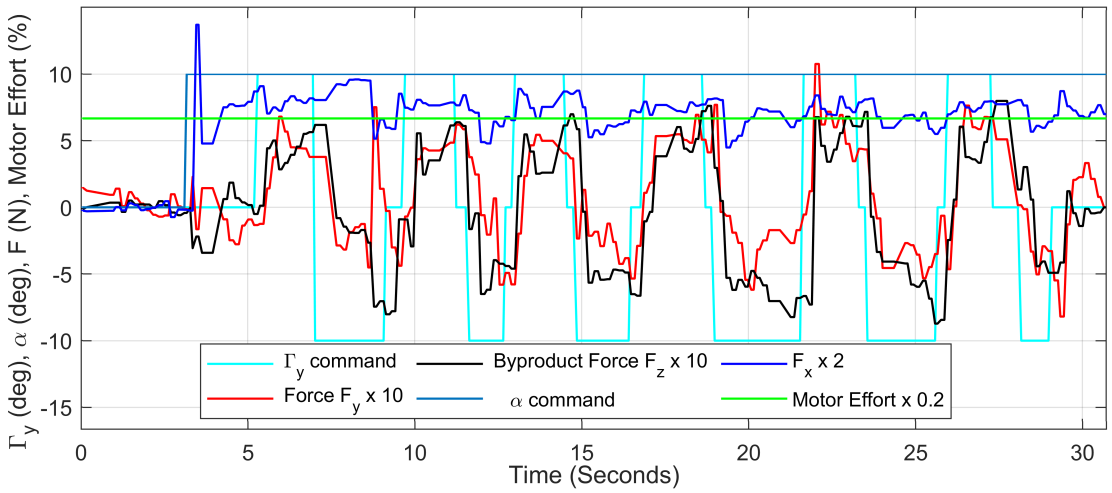

Figure 3.26. Cross-planar lateral-force coupling through simultaneous Γ and α commands.

3.3.5 Compensation for $\alpha + \Gamma$ Cross-Planar Coupling

Drag-forces on rotating blades can induce coupling between maneuvers on separate planes. Returning to the 2D planar representation of blade angles from Fig. 3.3, Fig. 3.27 presents the total pitches of blades as they pass through four quadrants, as well as their respective drag forces into or out of the page. Blade drag projected from the xy-plane manifests as unwanted sway force in the xz-plane.

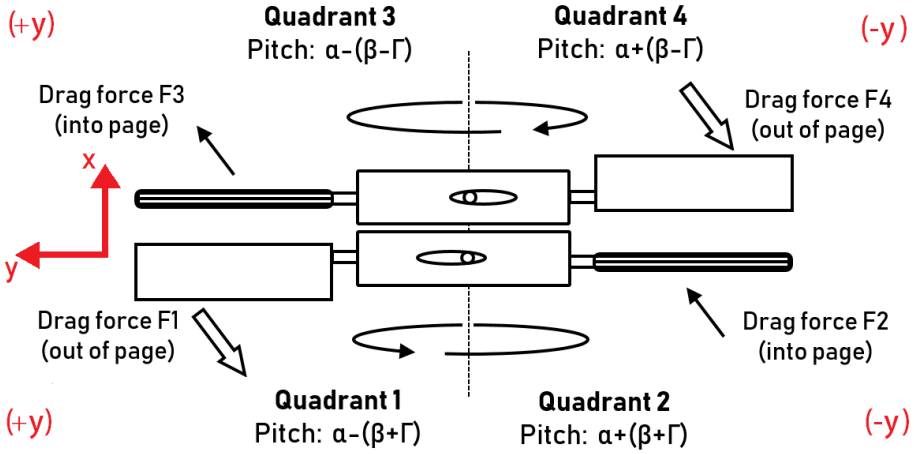

Figure 3.27. Two-dimensional representation of final blade angles with resulting drag forces.

The total drag force into or out of the page is calculated with the understanding that drag scales with pitch angle *squared* [49]. The total force into the page is then

$$\begin{aligned} F_{\text{tangential plane}} &= (F_2 - F_1) - (F_4 - F_3) \\ &\propto \left((\alpha + (\beta + \Gamma))^2 - (\alpha - (\beta + \Gamma))^2\right) - \left((\alpha + (\beta - \Gamma))^2 - (\alpha - (\beta - \Gamma))^2\right) = 8\alpha\Gamma \\ &\propto \alpha\Gamma \end{aligned} \tag{3.6}$$

where the β command cancels out, ensuring that any unwanted cross-planar force is proportional only to the product of commands α and Γ and is independent of β.

It is possible to compensate for this unwanted cross-planar sway force through a Γ-sway command in the other plane. Recall that the command α is shared across all servos in both planes and motor effort is also shared everywhere. Any desired sway force $F_{\text{wanted}} = \mathrm{K}_1\Gamma$ in one plane generates an unwanted byproduct sway force $F_{\text{unwanted}} = \mathrm{K}_2\alpha\Gamma$ in the other. So long as the ratio between unwanted byproduct force and desired force $\frac{\mathrm{K}_2\alpha\Gamma}{\mathrm{K}_1\Gamma} \triangleq \mathrm{K}_3\alpha$ is known, cross-planar coupling can be compensated for straightforwardly. The compensation process actually amplifies the desired sway forces generated, because the coupling only alters the effective direction of applied sway force while increasing its magnitude. For any desired commands $\Gamma_{\text{y, des}}$, $\Gamma_{\text{z, des}}$, and α, the final compensated sway commands $\Gamma_{\text{y, fin}}$ and $\Gamma_{\text{z, fin}}$ are derived through a system of equations linking the two planes

$$\left.\begin{aligned} \mathrm{K}_1\Gamma_{\text{y, fin}} - \mathrm{K}_2\alpha\Gamma_{\text{z, fin}} &= \mathrm{K}_1\Gamma_{\text{y, des}} \\ \mathrm{K}_1\Gamma_{\text{z, fin}} + \mathrm{K}_2\alpha\Gamma_{\text{y, fin}} &= \mathrm{K}_1\Gamma_{\text{z, des}} \end{aligned}\right\} \quad \begin{aligned} \Gamma_{\text{y, fin}} &= \frac{\Gamma_{\text{y, des}} + \mathrm{K}_3\alpha\Gamma_{\text{z, des}}}{1 + (\mathrm{K}_3\alpha)^2} \\ \Gamma_{\text{z, fin}} &= \frac{\Gamma_{\text{z, des}} - \mathrm{K}_3\alpha\Gamma_{\text{y, des}}}{1 + (\mathrm{K}_3\alpha)^2} \end{aligned} \tag{3.7}$$

effectively decoupling the two axes and eliminating cross-planar interference. From Fig. 3.26, K_3 is approximately $0.1\frac{N}{(N - deg\alpha)}$. Final commands $\Gamma_{\text{y, fin}}$ and $\Gamma_{\text{z, fin}}$ are read directly to actuators through (3.2). Desired commands $\Gamma_{\text{y, des}}$ and $\Gamma_{\text{z, des}}$ are used for control and will be referred to as Γ_{y} and Γ_{z}, respectively.

Figure 3.28 maps how desired commands Γ_{des} link to final Γ commands imposed on the actuators, for $K_3 = 0.1$ at $\alpha = 15^{\text{o}}$.

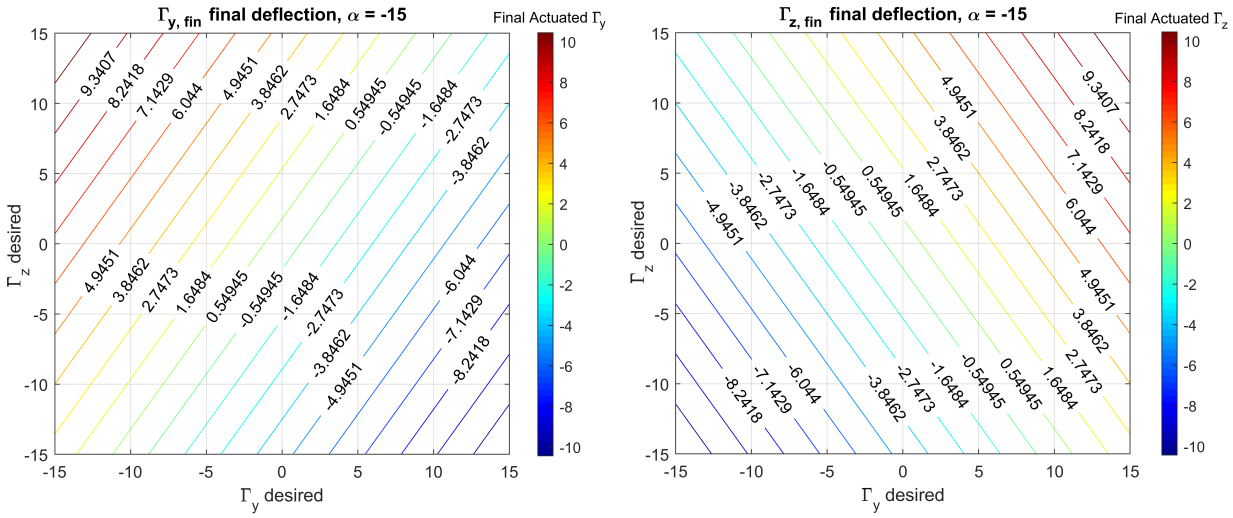

Figure 3.28. Map of final Γ_{fin} actuated values from superimposed $\Gamma_{(\text{x,y})\ \text{des}}$ inputs for $K_3 = 0.1$ at $\alpha = 15^{\text{o}}$.

Figure 3.28 adequately illustrates how compensation for the cross-planar forces actually *reduces* final actuator effort substantially, allowing for significantly larger desired commands to be achieved simultaneously before saturating the physical actuator limits. As such, the small-scale $(\alpha + \Gamma)$ experiment is re-run, with the cross-planar interference compensation algorithm implemented in accordance with Eqn. 3.7, and Γ_y-control steps of $\pm 20^{\text{o}}$. The results of the compensator-enabled $(\alpha + \Gamma)$ experiment are presented in Fig. 3.29.

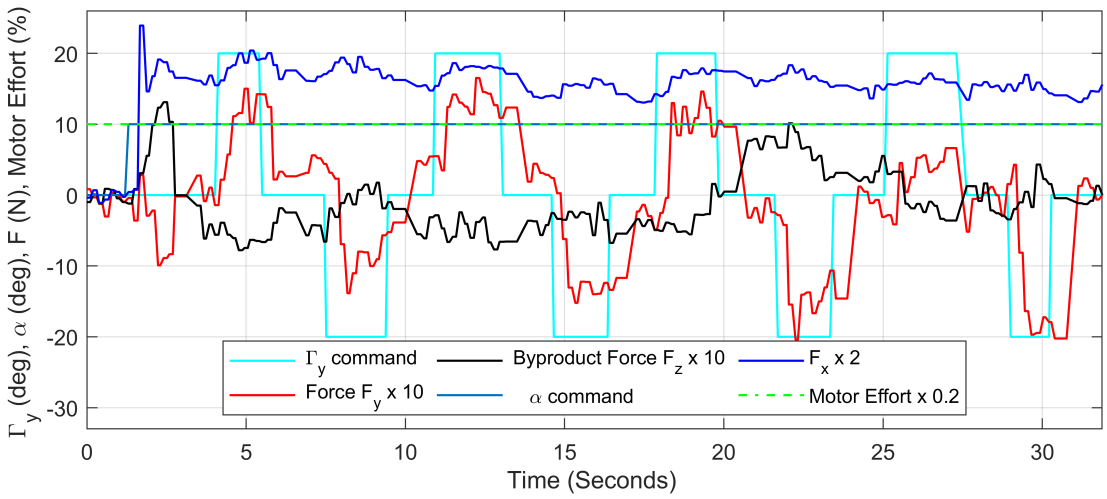

Figure 3.29. Compensation for cross-planar lateral-force coupling during simultaneous Γ and α commands.

The test was carried out in a somewhat smaller tank due to COVID-19 restrictions, adding noise to the forces measured, but the results of the experiment are clear. It is possible to compensate for cross-planar interference trivially during surge+sway maneuvers by understanding its behavior, exploiting the predictability of the re-directed lateral forces, and adjusting actuators accordingly. By successfully eliminating cross-planar interference, we have demonstrated how Eqn. 3.7 effectively decouples the two lateral axes and thereby allows for an uncoupled omnidirectional thrust controller.

For the small-scale model operating at 50% motor effort, open-loop control parameters are mapped to forces and torques as follows:

$$\begin{bmatrix} F_x \\ F_{\mathrm{y}} \\ F_{\mathrm{z}} \\ T_x \\ T_{\mathrm{y}} \\ T_{\mathrm{z}} \end{bmatrix} = \begin{bmatrix} F_{\mathrm{surge}} \\ F_{\mathrm{sway}} \\ F_{\mathrm{heave}} \\ T_{\mathrm{roll}} \\ T_{\mathrm{pitch}} \\ T_{\mathrm{yaw}} \end{bmatrix} = \begin{bmatrix} 8.9\mathrm{E}^{-1} & 0 & 0 & 0 & 0 & 0 \\ 0 & 9.6\mathrm{E}^{-2} & 0 & 0 & 0 & 0 \\ 0 & 0 & 9.6\mathrm{E}^{-2} & 0 & 0 & 0 \\ 0 & 0 & 0 & 7.1\mathrm{E}^{-4} & 0 & 0 \\ 0 & 0 & 0 & 0 & 2.2\mathrm{E}^{-2} & 0 \\ 0 & 0 & 0 & 0 & 0 & 2.2\mathrm{E}^{-2} \end{bmatrix} \begin{bmatrix} \alpha \\ \Gamma_{\mathrm{y}} \\ \Gamma_{\mathrm{z}} \\ \delta \\ \beta_{\mathrm{y}} \\ \beta_{\mathrm{z}} \end{bmatrix} \tag{3.8}$$

3.4 Conclusions

This chapter validates the underlying concepts behind an omnidirectional vehicle with speed and agility sufficient enough to work in turbulent environments inaccessible to traditional craft, as would be seen in many shallow marine environments that require inspection. The propulsor exploits properties emerging from continuous counter-rotating blades to generate near-instantaneous forces and moments in six degrees of freedom of considerable magnitude, and is designed to allow each DOF to be controlled independently by one of six decoupled control parameters. A small-scale model was built to verify different sets of maneuvers that would be used in any full-scale model. Slow-motion analysis confirms the instantaneous reaction time. Our novel method to generate lateral sway force underwater was originally simulated using STARCCM+ CFD software. Simulations suggested that the propulsor could generate sway thrust at a magnitude near 10-20% surge thrust capability [33], which was validated through the small-scale physical tests presented in this study.

A straightforward method for reorienting lateral forces resulting from blade drag was presented and demonstrated, and a basic open-loop controller was designed linking all open-loop control parameters for surge, yaw, and roll to desired output forces and moments on the small-scale model. We have shown that omnidirectional ROV propulsion can be achieved through a fully-actuated counter-rotating blade mechanism to potential speeds well beyond anything achieved through traditional ROV thrusters [3], and have validated the feasibility of producing instantaneous sway force using this mechanism.

Chapter 4

Full-Scale Propulsor Design and Simulation

This chapter details the design and simulation of the full-scale adaptation of the omni-directional propulsor. Using thrust estimations derived in Sections 4.2 and 4.3.2, the performance of disturbance and turbulence rejection is first modeled and compared against other ROVs. The mechanical design and kinematic analysis of each subsystem are then presented, followed by kinematic and hydrodynamic analysis of the hull and surrounding fluid forces during various blade maneuvers. Special maneuvers are verified using Computational Fluid Dynamic (CFD) software. Finally, an open-loop state-space model is constructed linking control-parameters to forces in each degree of freedom for the full-scale model.

This chapter is largely adapted from a conference paper [33] submitted to the ASME IDETC/CIE in 2019. The contents and simulations presented here were completed *prior* to the physical testing in Chapter 3, which verified the underlying principles and bolstered the CFD findings in this chapter.

4.1 Full-Scale Propulsor Design

We propose a small craft capable of true omnidirectionality at high speed. The proposed design consists of two sets of highly-actuated counter-rotating blades centered around a hollow tubing framework. The diameter of said tubing is chosen to allow for the safe wiring of four 670-watt brushless motors operating at maximum load. Designed mostly around pre-manufactured parts, the outer hull has a main diameter of 0.14m (5.5in) and length of 0.41m (16in) without nose attachments. Figure 4.1 presents an overview of the design.

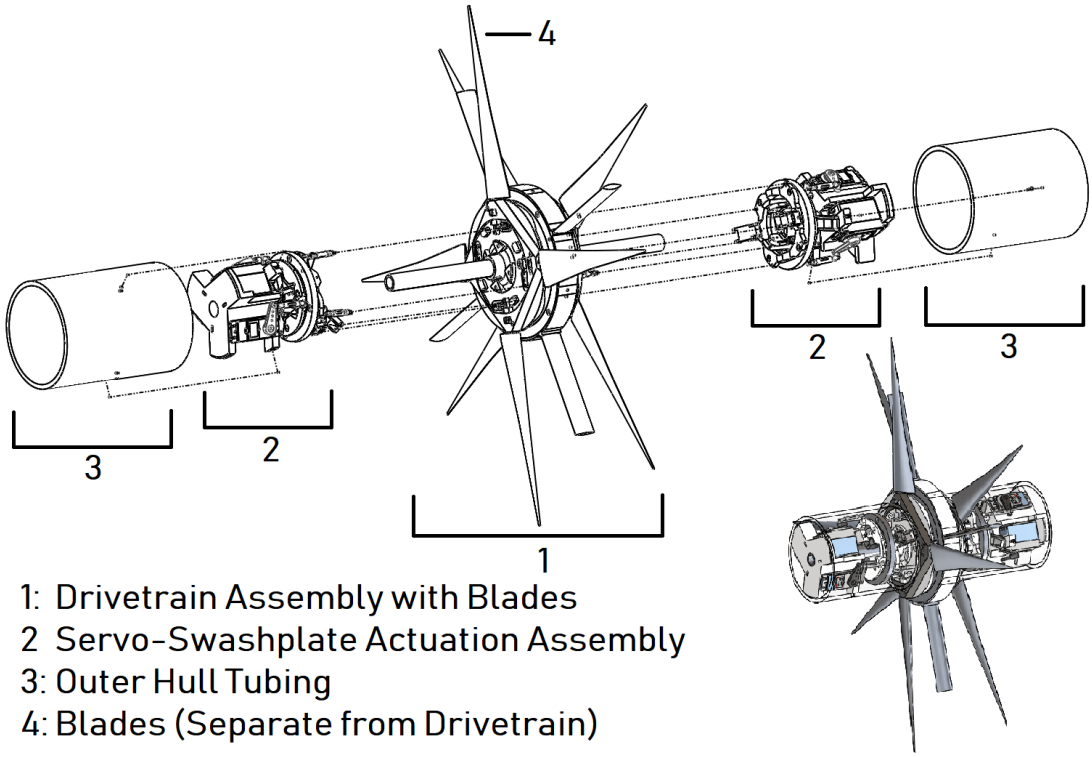

Figure 4.1. Overview of all subassemblies to be discussed.

The hull is designed to be largely free-flowing for required motor cooling and quick deployment. Such cooling is made necessary by the considerable power-to-volume ratio of the motors.

4.1.1 Drive Mechanism and Dynamic Rotor Torque Input

The drive mechanism must provide independent torque to the system's rotors while locking their relative alignment and be able to support the stationary flaps responsible for limiting unwanted flow. It must also keep unwanted torques from its main bearings while staying rigid and strong at primary blade attachment points. Fortunately, geometric exploits allow for a relatively simple design solution. An engineering diagram of the entire drivetrain mechanism is shown in Fig. 4.2.

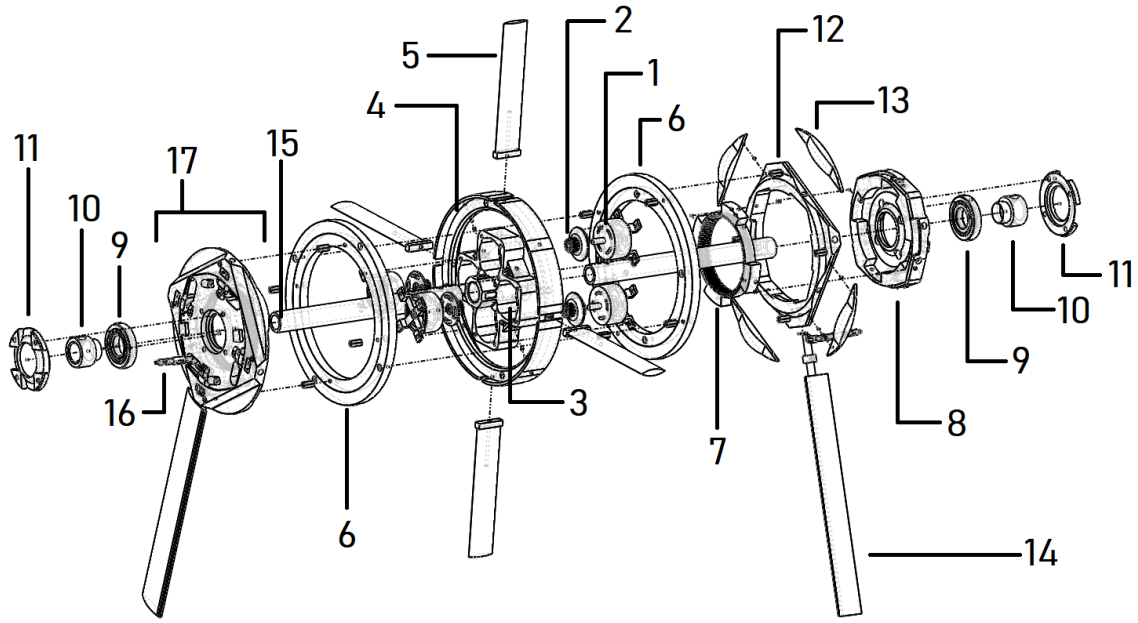

1: HK- ST4010 Brushless Motor
2: Motor-Gear Attachment
3: Motor Holder
4: Blade-Axis Re-enforcing Susan Bearing Adapter
5: Stationary Backflow Control Flaps
6: 300mm Lazy Susan Bearing
7: Direct-Transmission Gear
8: Gear/Bearing/Pitch-Ctrl Adapter
9: Corrosion-Resistant Bearing
10: Bearing-Bk.Bone Adapter
11: Ctrl Adapter-Bearing Lock
12: Blade to Transmission Coupler and Shock Buffer
13: Shock Buffer Flow Corrector
14: Dynamic Blades (only 2 of 8 shown)
15: Structural Tubing
16: Dyn. Blade Pivot Adapter
17: Assembled Parts (7, 8, 12, 13, 14)

Figure 4.2. The exploded drivetrain of proposed design. Two dynamic blades and structural tubing are included for reference.

The drivetrain is powered by two pairs of Hobbyking ST-4010-820kv brushless motors. These $15 motors are chosen for their exceptional torque, power, size, and material-based bearing design that allows for corrosion resistance rare for motors of their size. A standard brushless motor torque-frequency linearity is constructed from data collected on Hobbyking.com regarding the motor's performance at maximum power under load in Fig. 4.3.

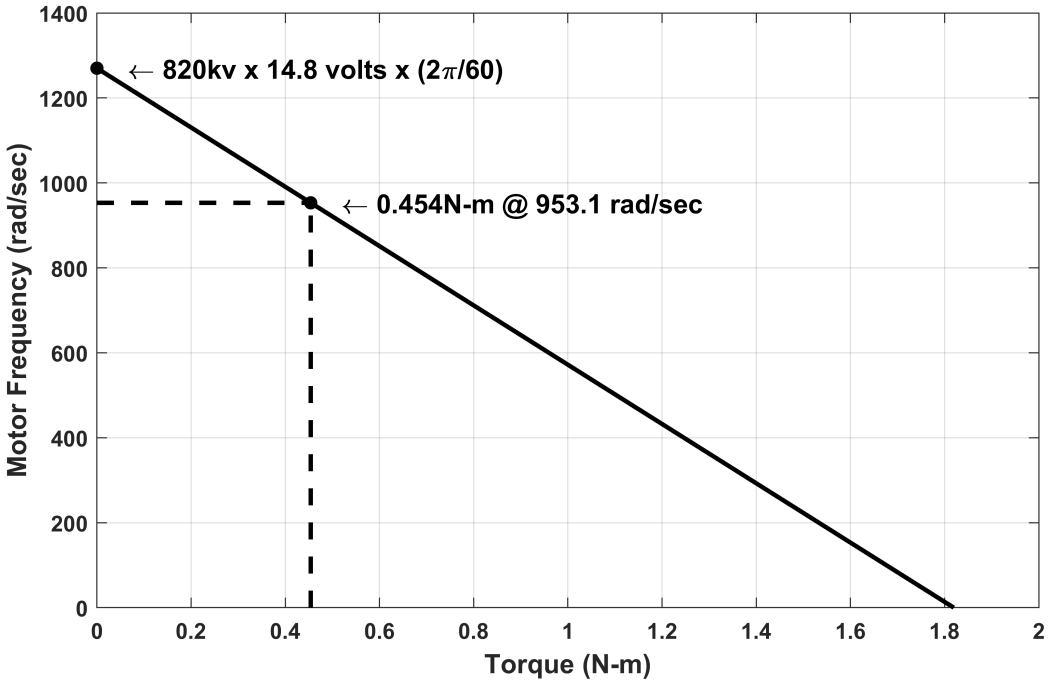

Figure 4.3. Torque-frequency chart for the Hobbyking ST-4010-820kv brushless motor.

From the chart, the relation between rotary frequency and output torque for each individual motor is constructed:

$$Motor\ Torque = (1270 - Motor\ Freq.)(\frac{0.454}{1270 - 953.1}) \tag{4.1}$$

where $Motor\ Torque$ is measured in $N \cdot m$, and $Motor\ Freq.$ is measured in $\frac{rad}{sec}$. From this, stall torque was calculated to be 1.82 N-m per motor, from which gears were designed to withstand the resulting 343.22N at the teeth. With a 14:132 gear-reduction from motor

to rotor, and two motors per rotor, the net torque on each rotor is related to blade rotation frequency:

$$T = -0.2547\dot{\theta}_{\text{rot}} + 34.3094 \tag{4.2}$$

where T is the *rotor* torque and $\dot{\theta}_{\text{rot}}$ is the corresponding rate of rotation. Despite the trivial torque advantage of putting two motors on each rotor, the primary reason for motor pairing is to prevent gear slipping, as many of the parts in or near the motor housing are not exceptionally rigid. Fig. 4.4 elaborates this concept while presenting a cut-out of the completed drive assembly to show where the motors are housed.

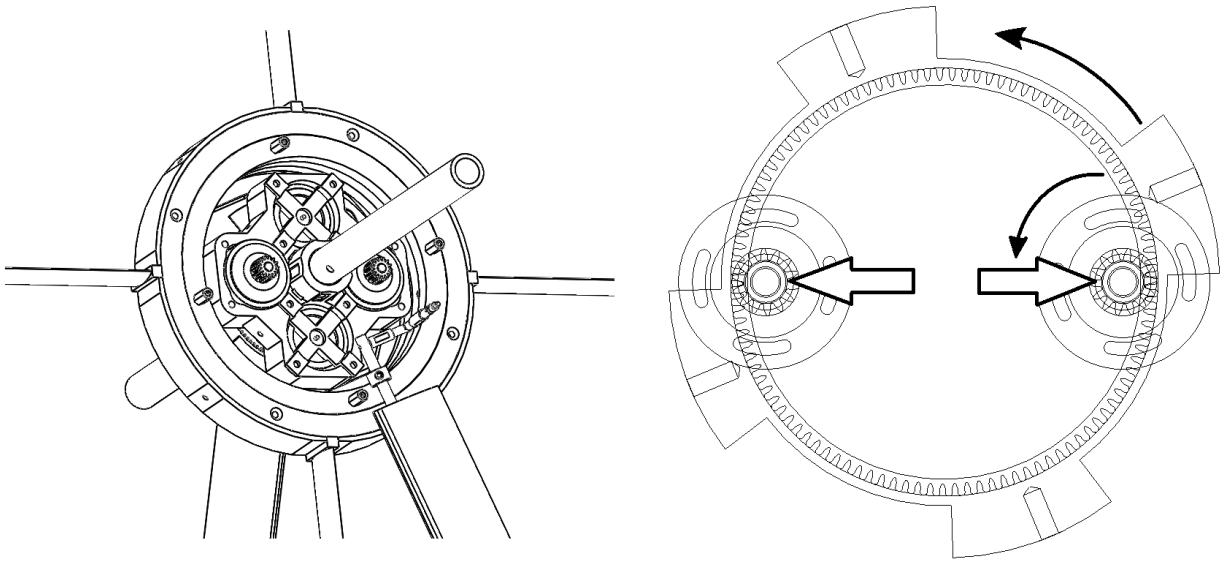

Figure 4.4. Anti-slip solution via force-balancing of twin-motor gear setup. Paired motors re-enforce each-other with respect to their shared midpoint, preventing gear slipping by greatly reducing warping in the direction of said midpoint.

Rotors are decoupled from one-another to allow for simple roll control via torque-balancing. As the effective input to each rotor is torque, not speed, roll-torque remains balanced regardless of blade parameters and relative speed, as rotation rate is simply a byproduct of the torque input. This allows for roll control via a single parameter δ, effectively decoupled from all other parameters and realized merely by varying the relative

effort between the two rotors. The separate rotors are read $\{90\%$ effort $\pm\delta\}$, where $\delta \in (-10\%, 10\%)$. Rotors can alternatively be read $\{100\%$ effort $\pm\delta(1 \mp \text{sign}(\delta))\}$ with no limitations on δ.

To prevent unwanted physical blade interactions, rotors are locked in alignment about their respective axes through the blade-axis re-enforcing double bearing adapter. This allows the rotors to push against one-another without touching and thereby lock axially. The same mechanism also eliminates unwanted torques on the underlying rotor bearings though the use of perpendicularly-locked standoffs, while allowing for the attachment of the stationary blades responsible for reducing unwanted flow. Fig. 4.5 details the blade-axis re-enforcing double bearing adapter.

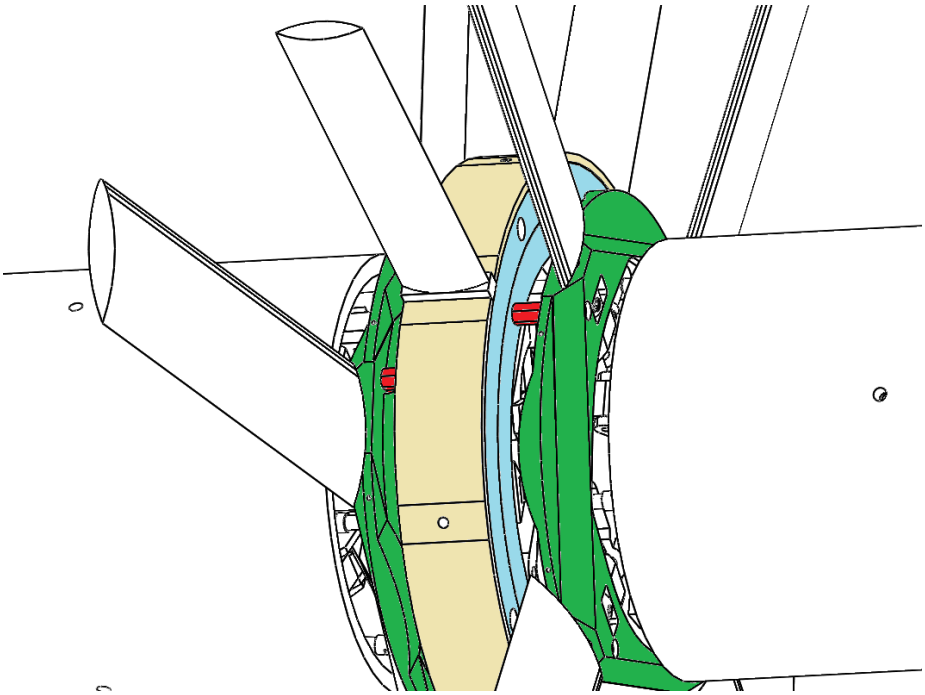

Figure 4.5. The blade-axis re-enforcing flap adapter (BARFA). The BARFA consists of two 300mm lazy susan bearings (one shown in blue) connected to a central stationary section (yellow) from which stationary flaps can attach. Through perpendicular standoffs (red), the bearings attach directly to the aluminum blade adapters (green) that comprise the structural integrity of each rotor. Because the rotors are already locked on each-other's axes, the perpendicularity of the standoffs geometrically locks the rotors about the axis of the hull.

The central piece of the BARFSA also attaches to the underlying motor housings with four 2-inch number 6 screws. These screws prevent the back-flow flaps from drifting about the roll-axis, and alleviate shear forces from the underlying rotor bearings.

4.1.2 Servo-Swashplate Actuator Mechanism

The design consists of two servo-swash plate actuation mechanism (SSPAM) assemblies, each connecting to its own set of four blades. Each SSPAM must quickly and accurately manipulate the pitch of spinning blades in a manner independent of rotation rate, such that blade pitch becomes some function of angle θ_{rot}. This is made possible by altering the planar projection of a wide bearing assembly (swashplate) connected to the trailing edge of each blade. Dimensions are set such that the blades rotate 10^{o} when all actuators rotate 10^{o}, with linear proportionality. Fig. 4.6 projects the expanded mechanism of a single SSPAM in its entirety.

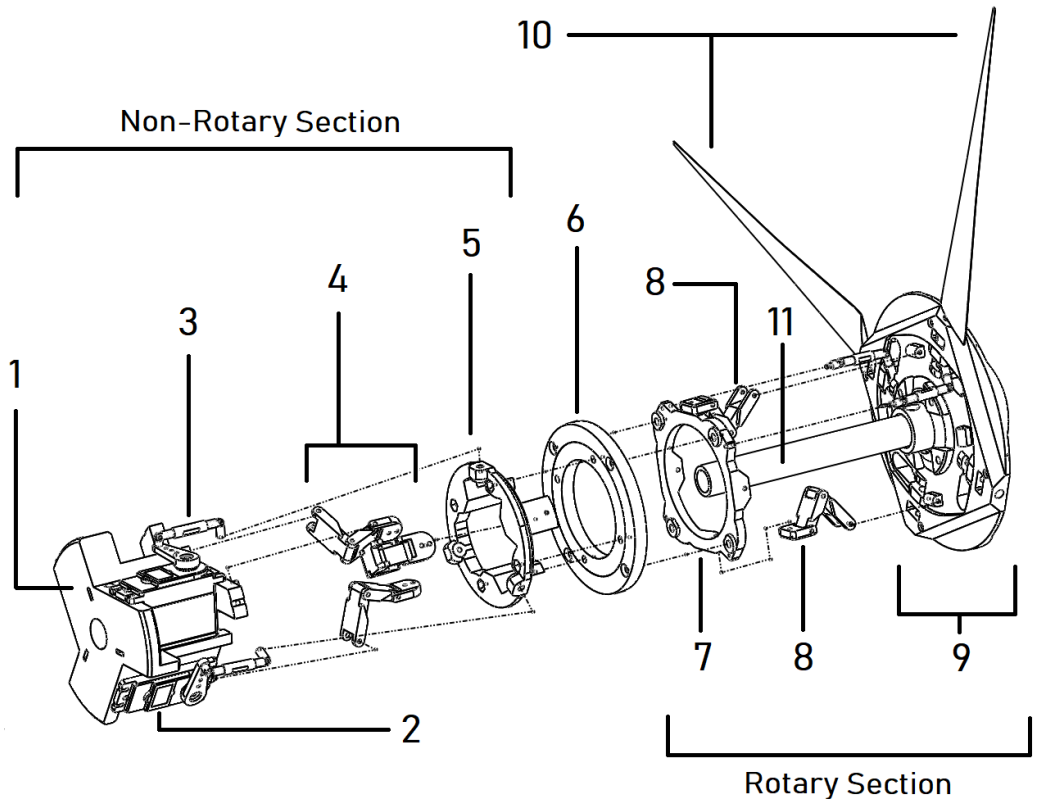

Figure 4.6. The servo-swashplate actuator mechanism of proposed design. There are two in total. One rotor with two blades and central tubing are shown as a visual reference.

Three servos manipulate the forward offset and planar orientation of a lazy-susan bearing. The relative horizontal angle of the swashplate orientation varies the relative tug on the blade edges between the right and left half of the hull, while the relative vertical angle varies the tug between top and bottom. The net forward offset of the swashplate

thus pushes and pulls on the average pitch of *all* blades regardless of plate orientation, controlling surge. Hinges on the servo mount connect to the stationary side of the plate mechanism and bear the torsional load of rotary friction within the plate while allowing for orientation changes. Similar hinges align the spinning rotors with the dynamic end of the plate, bearing the torsional load of the blade-pivot connectors and allowing for pivots to push rather than only pull. These dynamic hinges must attach to the plate on the same geometric plane where the stationary hinges connect to actually allow for the plate to adjust its orientation.

KST BLS662WP servos were chosen to drive this mechanism for their high torque, high speed, and waterproof nature at low depth. The radial alignment of these servos to was chosen to minimize total hull radius while maintaining structural integrity, detailed in Fig. 4.7.

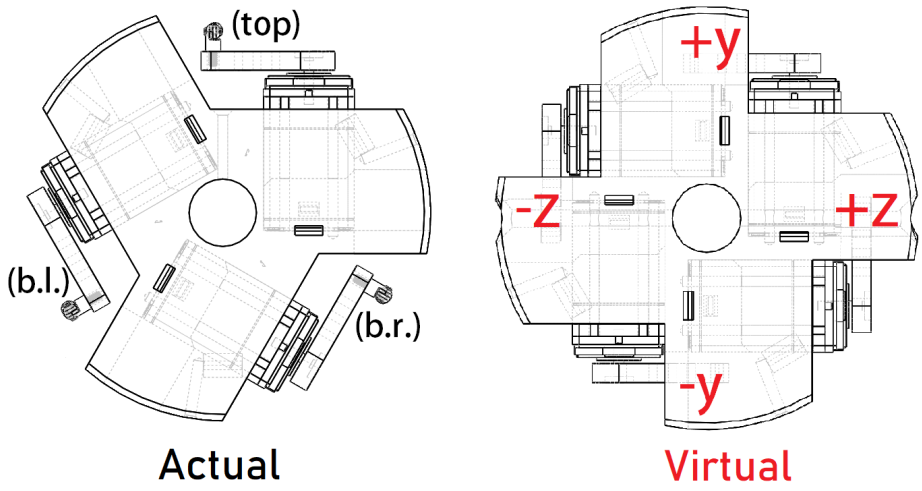

Figure 4.7. Alignment of the BLS662 servos for swashplate actuation. This configuration has a maximum diameter of 4.7 inches, allowing the hull to be composed of 5in PVC tubing.

As with the small-scale model, control-commands are represented in a virtual four-servo configuration, while physically executed through the physical three-servo configuration.

4.2 Blade Design and Surge Thrust Estimation

The Wortmann FX 76-100 hydrofoil profile was chosen for its bidirectionality, wide linear regime, and exceptional lift/drag performance. Its lift-to-drag (C_l to C_d) coefficient ratio peaks at an attack angle of 6.5 degrees, where $C_l = 0.75$ and $C_d = 0.018$ [49]. Fig. 4.8 shows the dimensionless FX76-100 profile.

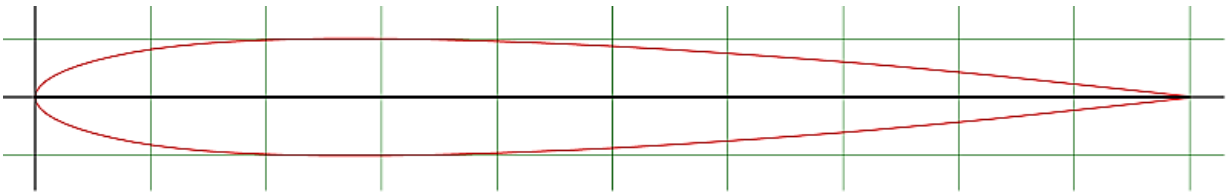

Figure 4.8. The WORTMANN FX 76-100 bi-directional hydrofoil profile. This hydrofoil peaks in lift/drag at 6.5 degrees, where it is expected to produce maximum thrust in all fluids.

4.2.1 Thrust and Torque

The lift force dF and drag force $d\mathrm{D}$ across a single hydrofoil cross-section of thickness $d\mathrm{r}$ and cord-length C are given:

$$dF = \frac{1}{2}\rho C C_l \mathrm{V}^2 d\mathrm{r} \qquad d\mathrm{D} = \frac{1}{2}\rho C C_d \mathrm{V}^2 d\mathrm{r} \tag{4.3}$$

If the hydrofoil spans in the direction of r such that cord length $C = C(\mathrm{r})$ from $\mathrm{r} = R_i$ to $\mathrm{r} = R_o$, and the attack velocity V varies across r such that $\mathrm{V} = \mathrm{V}(\mathrm{r})$, the net force on the blade is

$$F = \int_{R_i}^{R_o} \frac{1}{2}\rho C(\mathrm{r}) C_l \mathrm{V}^2(\mathrm{r}) d\mathrm{r} \tag{4.4}$$

while the corresponding drag is

$$\mathrm{D} = \int_{R_i}^{R_o} \frac{1}{2}\rho C(\mathrm{r}) C_d \mathrm{V}^2(\mathrm{r}) d\mathrm{r} \tag{4.5}$$

Rather than moving in a straight line, we assume the hydrofoil is instead rotating around an axis with positive radial offset R_i alongside three others sharing the same axis and torque, as with our setup. The resulting thrust from all four hydrofoils that make up the rotor is

$$F = 4\int_{R_i}^{R_o} \frac{1}{2}\rho C_l C(\mathrm{r}) \mathrm{r}^2 \dot{\theta}_{\mathrm{rot}}^2 d\mathrm{r} \tag{4.6}$$

while the resulting roll torque equates to

$$T = 4\int_{R_i}^{R_o} \frac{1}{2}\rho C_d C(\mathrm{r}) \mathrm{r}^3 \dot{\theta}_{\mathrm{rot}}^2 d\mathrm{r} \tag{4.7}$$

where F is the net thrust of the rotor, T is the net torque, r is the distance from the central axis, R_i is the rotor's inner radius where blades begin, R_o is the outer radius of the rotor where the blades end, ρ is the density of salt water, and $\dot{\theta}_{\mathrm{rot}}$ is the angular rate of rotation. Physical design constraints render R_i equal to 0.09m, and the base cord-length $C(R_i) \equiv C_i$ equal to 0.05m. The hydrofoil attack angle ϕ_{b} is set to 6.5 degrees, where the thrust is expected to peak if limited by torque.

Recall the angular velocity of each rotor (and hence each blade) is linked to motor-induced rotor-torque limitations through Eqn. 4.2. Though Eqn. 4.2 is derived from motor performance specifications, it still holds true for evaluating blade-induced hydrodynamic torque limitations, provided the rotation rate $\dot{\theta}_{\mathrm{rot}}$. For any particular rotation rate $\dot{\theta}_{\mathrm{rot}}$ and blade profile $C(\mathrm{r})$, the thrust solution resulting from Eqn. 4.6 is valid for our proposed design so long as

$$T = 4\int_{0.09}^{R_o} \frac{1}{2}\rho(0.018)C(\mathrm{r})\mathrm{r}^3\dot{\theta}_{\mathrm{rot}}^2 d\mathrm{r} \leq -0.2547\dot{\theta}_{\mathrm{rot}} + 34.3094 \tag{4.8}$$

assuming a hydrofoil attack angle ϕ_{b} of 6.5 degrees, where the thrust is expected to peak if limited by torque. Through MATLAB, many combinations of $C(\mathrm{r})$, R_o, and $\dot{\theta}_{\mathrm{rot}}$ are tested and their thrusts evaluated. Whenever the Eqn. 4.8 torque inequality fails, the datapoint is considered invalid and effectively thrown out. It quickly becomes apparent the best $C(\mathrm{r})$ cord-length function that results in the highest valid thrust outputs is a linear decrease in cord length from C_i to as small a length as possible at the blade tip C_o. Cord at the tip C_o is then set to 2mm (0.002m) such that the blade profile $C(\mathrm{r})$ is effectively triangular:

$$C(r) = C_i(R_o - r)/(R_o - R_i) \tag{4.9}$$

With $C(\mathrm{r})$ now defined, a MATLAB script is run to map the combinations of R_o and $\dot{\theta}_{\mathrm{rot}}$ that yield the highest thrusts given the Eqn. 4.8 torque constraint. Fig. 4.9 details the output.

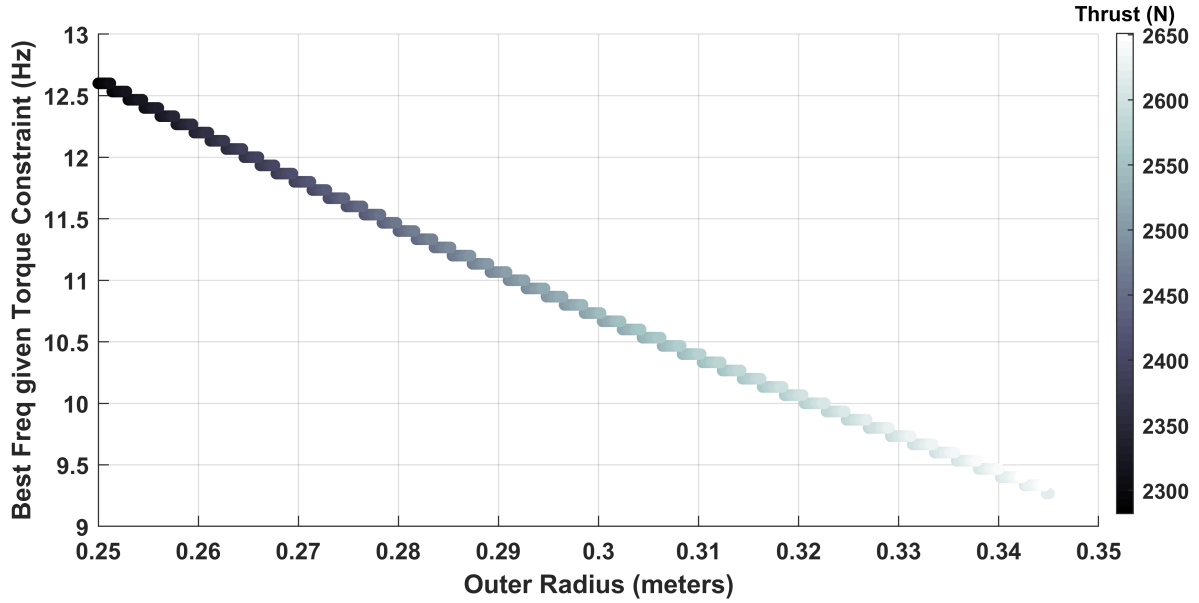

Figure 4.9. Dual-rotor performance given torque constraints as a function of frequency, assuming 50% efficiency. Many combinations of R_o and $\dot{\theta}_{\mathrm{rot}}$ are tested. Thrust is only evaluated and plotted if torque limitations are satisfied. 10Hz equates to 80Hz blade overlap frequency.

Elastic Blade Deformation

Such a short tip length C_o raises concerns as to tip deflection and warping under differential force. With the force profile along r defined in Eqn. 4.3 and assuming $\mathrm{V(r)} = \mathrm{r}\dot{\theta}_{\mathrm{rot}}$, these concerns are easily tested with a fundamental mechanics formula for beam deflection Y. We impose a total thrust of 625N with a force-profile proportional to cord-length and to r^2, spanning the length $\mathrm{r} = R_i$ to R_o. We also assume carbon-fiber composition and that $R_o = 0.33$m, the same as the disk used in CFD simulations to model the sway maneuver (see 4.3). The final deflection Y at the blade tip in the axial direction of the rotor is

$$\mathrm{Y}(r = R_o) = \int_{R_i}^{R_o} \int_{\mathrm{r}^*}^{R_o} \frac{M_r(\mathrm{r})}{EI(\mathrm{r})} d\mathrm{r} d\mathrm{r}^* \Big|_{\mathrm{r}=R_o}, \quad \frac{d\mathrm{Y}}{d\mathrm{r}}\Big|_{\mathrm{r}=R_i} = 0, \quad \mathrm{Y}(r = R_i) = 0 \tag{4.10}$$

$$\mathrm{Y}(r = R_o) = 21.1224 \cdot \int_{R_i}^{R_o} \int_{\mathrm{r}^*}^{R_o} \frac{\frac{R_o \mathrm{r}^3}{3(R_o - R_i)} - \frac{\mathrm{r}^4}{4(R_o - R_i)}}{(\frac{R_o - \mathrm{r}}{R_o - R_i})^4} d\mathrm{r} d\mathrm{r}^* \Big|_{\mathrm{r}=R_o} \approx 6mm$$

where E is the elastic modulus of the fiber composite and $M_r(\mathrm{r})$ is the bending moment down the length of the blade. The value $I(\mathrm{r})$ is the area moment of inertia of the hydrofoil's cross-section S evaluated at r, such that $I(\mathrm{r}) = \iint_S y^2 dC' dy$ when y is distance tangential to the maximum cordlength/centerline, and $C' = C'(y)$ is effective cord-length evaluated at said offset y.

Although attack velocity increases with radius, the decreasing hydrofoil cord length evidently ensures force distribution does not also increase with radius, bolstering the results of Eqn. 4.10. The tip deflection problem is thus negated with the reassurance that re-enforcement rings can be trivially implemented on all blade tips. To address safety concerns and prevent damage to the tether or physical testing environment, such outer rings may be implemented anyways.

4.2.2 Final Blade Profile

Hydrofoils such as the WORTMANN FX 76-100 have a property where it takes little to no torque to rotate them about some pivot point located approximately 30% up the cord length, for small attack angles ϕ_b in the linear regime of the foil under load[22]. Fig. 4.10 outlines the final blade design, showing where the hydrofoil pivots are located to exploit the pivot-torque property and minimize force on the actuating servos.[1]

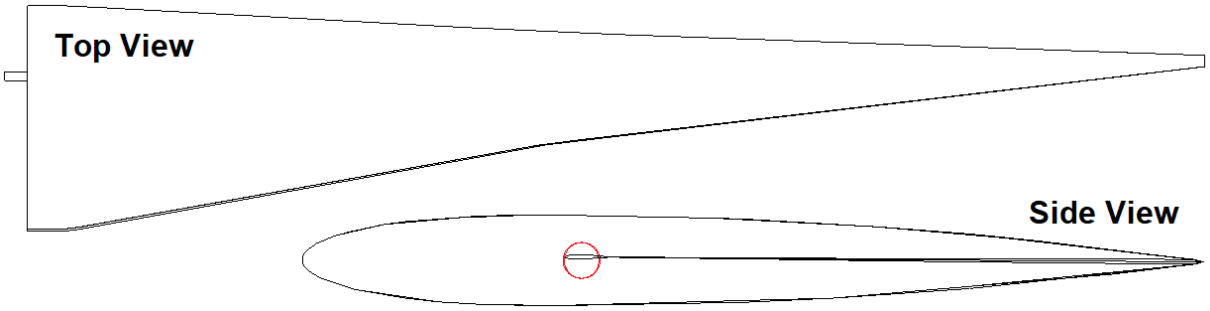

Figure 4.10. Final blade profile of proposed design. The cord profile (top view) of the blade is made mostly triangular to maximize thrust according to MATLAB simulation, while all cross-sections pivot about a point approximately 30% down the cord line, alleviating flow-based back-force on the servos that actuate them.

4.3 Simulated Sway Performance

It is important to note that the full CFD modeling of roll, surge, and yaw maneuvers was determined to have lesser relevance in testing practicality of the proposed mechanism. For example, in no reasonable scenario will pulling *all* blade pitches forward *not* cause the craft to surge as intended if properly programmed with servo limits considered. Yaw and roll control parameters are similarly straightforward. These maneuvers are practically identical to the operational foundation of all dual-blade rotorcraft, such as the Kamov-52 Helicopter shown in Fig. 4.11.

[1] If necessary, the pivot point in Fig.4.10 can be slightly shifted to induce light stability around $\phi_b = 0^o$, easily overcome by the KST BLS662 servos, but solving problems regarding instability from servo margin of error, and also allowing for servo duty-cycle and voltage modulation for thrust precision (see 6.2).

Figure 4.11. [45] Russian Airforce Kamov-52 attack helicopter. Rotorcraft such as this are often favored for the superior safety of the coaxial rotor design and lack of high frequency vibration, making them ideal for targeting systems on military aircraft [37].

A report by the Kamov Helicopter Company [37] explains the superior qualities of coaxial models, ranging from greatly reduced flight hazards to the simplicity of turning via decoupled torque and increased control authority. For coaxial helicopters, the mechanical complexities arising from dual-motor, dual-swashplate systems bypass the need for a tail rotor, so the agility and safety benefits alone make them ideal for Kamov's military rotorcraft.

4.3.1 Interactions Between Rotors

A fundamental difference between the yaw maneuver of areal coaxial rotorcraft and that of the proposed design is the incompressibility of water, which raises concerns as to blade-interaction for maneuvers requiring rotors to push or pull against one-another in certain quadrants. Decreasing the complexity in simulation parameters allows for such

an experiment to be fully tested in CFD using STARCCM+ software. Simplified blades of constant 1" cord length are modeled and forced to a testing frequency of 10Hz with unlimited torque and oriented to push against one-another. It is then assumed that any thrust or force spikes measured are much higher than those on the design's actual blades, do to their wide dimensions and lack of torque limitations. Fig. 4.12 presents results from the CFD simulation on rotor interactions.

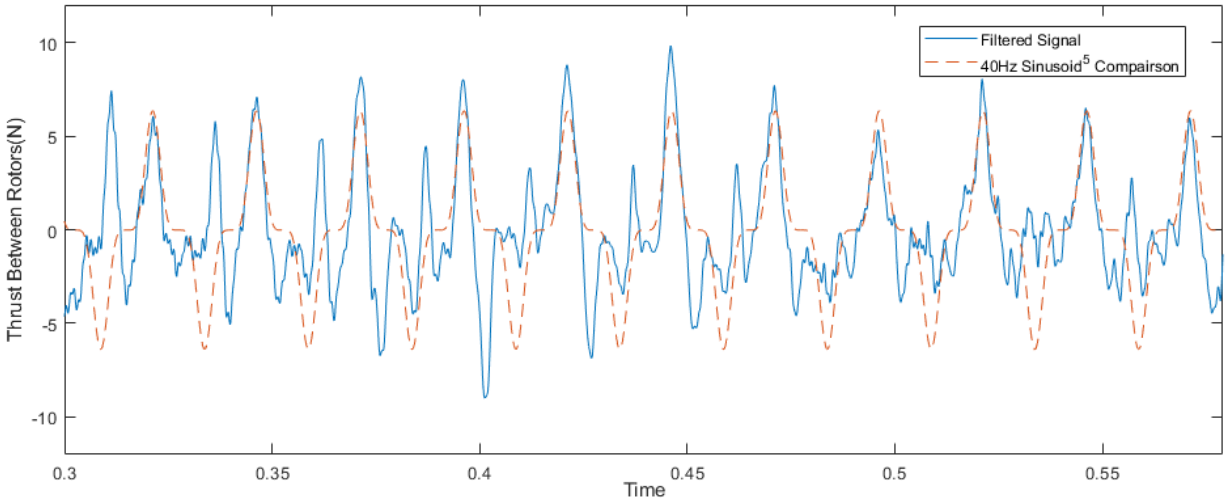

Figure 4.12. Filtered force output measured between rotors pushing in opposite directions. Only one rotor in the simulation is actually spinning at 10Hz (40Hz overlap), which would equate to both rotors spinning at 5Hz with some fluid rotation rate and thrust offset. Force is measured on the rotating rotor alone.

The force oscillation amplitude between rotors never surpasses nine newtons at 5-10Hz, which is minuscule in comparison to design thrusts and still larger than any force oscillations on the smaller, finalized blades of the proposed design. From this, we conclude blade interactions may affect IMU measurements but will not damage the hull, blades, or drive mechanism. The affect on the torque of each passing blade about its pitch axis was not measured, but is still assumed to be far less than the 300N·cm required to overwhelm the BLS662 servos.

4.3.2 CFD Sway-Force Approximation and Simulation

Due to particularly small geometries near the blade tips, and highly-pronounced torque implications that result from any reduced accuracy, pure CAD-based CFD propeller simulations have proven to be impractical and unwieldy, where a highly-accurate simplified approach to blade simulation should be taken instead. First, we define two cylindrical regions with the same outer radii R_o as our rotor. A central cutout of radius R_i is assigned to each region, and each cylinder is given a thickness equal to the maximum blade projection possible in the direction of the hull axis. As these disks represent the regions the blades will cover along their rotation, we then implement the relative force intensity of thrust as a function of position (Eqn. 4.6) that we derived from hydrodynamic properties of the finalized blade design along the surface of each virtual disk. We also include knowledge that for the sway (and yaw) maneuver, blade pitch ϕ_{b} is linked to the blade angular position about the hull of the craft θ_{rot} through proportionality with $\sin(\theta_{\mathrm{rot}})$. The thrust-force intensity should then also be proportional to $\sin(\theta_{\mathrm{rot}})$.

CFD input forces are reduced by a factor K to allow for CFD simulation convergence, with the assumption that output force magnitude can be re-multiplied by the factor K to approximate full-scale forces on the craft. We arrive at a formula for the force intensity $[N/m^2]$ at any point (x, y) on the disk, where $\mathrm{r} \triangleq \sqrt{x^2+y^2}$, using $\frac{dF}{d\mathrm{r}}$ as defined in Eqns. 4.3 and 4.6, with $C(\mathrm{r},C_i)$ in Eqn. 4.9. Our rotor-force simulation failure limit was around 40N, but is generalized here as $F_{RotorLim}$.

$$
\begin{aligned}
F_{BladeLim} = \frac{F_{RotorLim}}{4} &= (\mathrm{K}) \cdot 2 \int_0^{\pi} \int_{R_i}^{R_o} \frac{dF}{d\mathrm{r}} sin(\theta_{\mathrm{rot}}) \mathrm{r} d\mathrm{r} d\theta_{\mathrm{rot}} \\
&= \mathrm{K}\rho C_l C_i \dot{\theta}_{\mathrm{rot}}^2 \int_0^{\pi} \int_{R_i}^{R_o} \frac{R_o - \mathrm{r}}{R_o - R_i} \mathrm{r}^3 sin(\theta_{\mathrm{rot}}) d\mathrm{r} d\theta_{\mathrm{rot}}
\end{aligned}
$$

$$\mathrm{K} = \frac{2.5(R_o - R_i)F_{RotorLim}}{\rho C_l C_i \dot{\theta}_{\mathrm{rot}}^2 (R_o^5 + 5R_i^5 - 5R_o R_i^4)}$$

$$\frac{dF}{dA}(x,y) = \mathrm{K}\rho C_l C_i \dot{\theta}_{\mathrm{rot}}^2 \frac{R_o - \mathrm{r}}{R_o - R_i}\mathrm{r}^2 sin(\theta_{\mathrm{rot}}) = \frac{2.5F_{RotorLim}(R_o - \mathrm{r})\mathrm{r}\cdot y}{R_o^5 + 5R_i^5 - 5R_o R_i^4} \tag{4.11}$$

The pressure distribution $\frac{dF}{dA}$ from Eqn. 4.11 imposed by a rotor during the sway maneuver is then plotted across the sweep area, shown in Figure 4.13. The force intensity shown in Figure 4.13 assumes blades are working at maximum rotor force capability for CFD simulation convergence- only 40N per rotor.

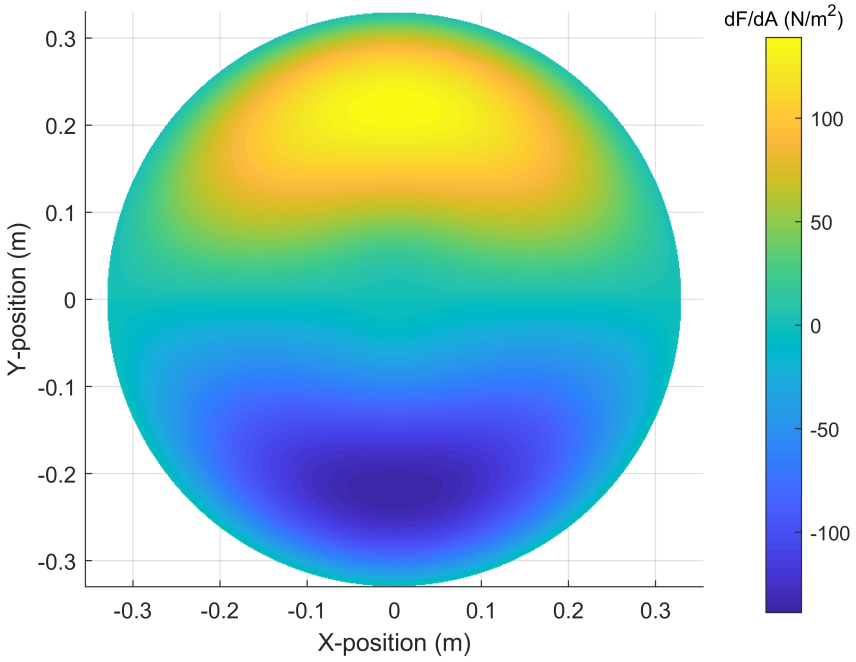

Figure 4.13. Imposed pressure distribution $\frac{dF}{dA}$ across swept wing area during the sway maneuver by a single rotor.

With the virtual blade regions now fully defined, a simplified version of the hull with back-flow flaps can be inserted between the disks in the CFD sway simulation. In this simplification, the backflow control flaps are allowed to extend slightly into the disk regions to simulate the presence of blades inside the disk region. Results of this simulation are shown in Fig. 4.14.

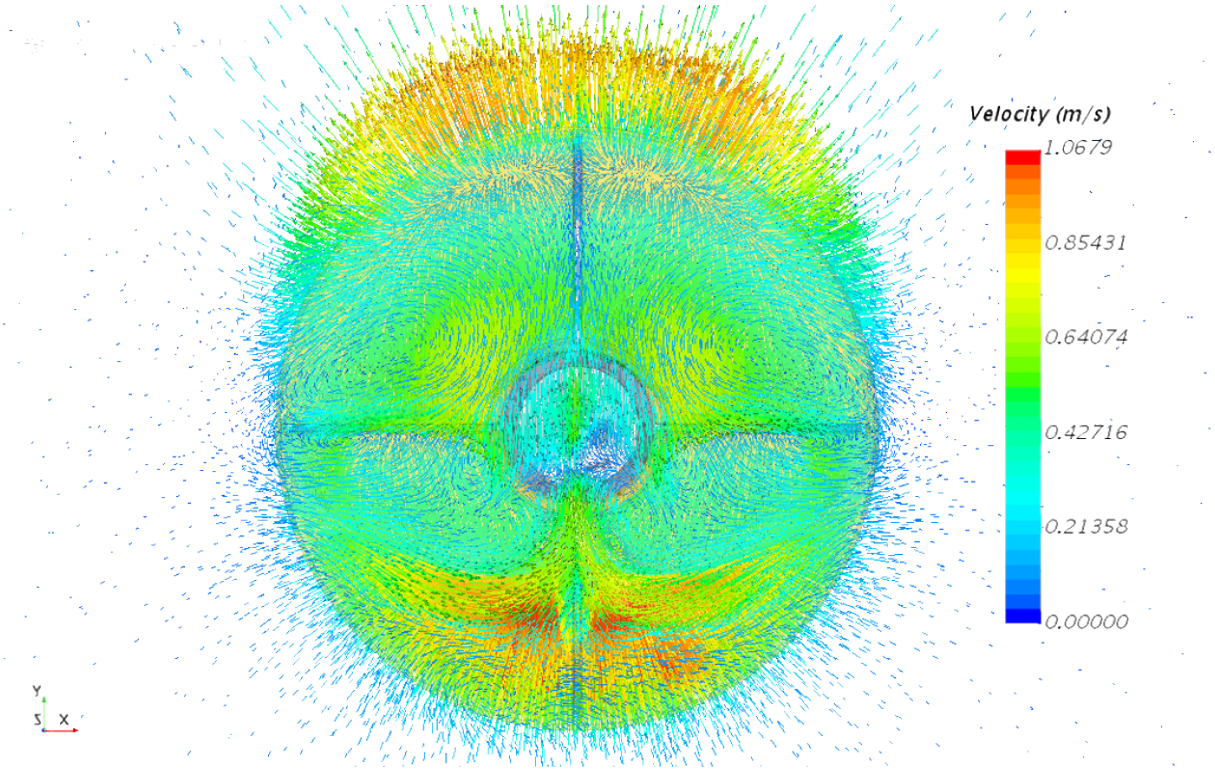

Figure 4.14. Vector graphic of dual-disk simulation for the sway maneuver. Color indicates the magnitude of velocity, though vectors generally point in the +y direction.

To actually measure the force output from the CFD sway simulation, we define a virtual box [8] of side-length L around the craft in CFD. All sides of this virtual box have walls of very small but finite volume and are comprised of CFD cells. The y-force due solely to

fluid momentum on each wall of the box in the direction $\hat{y}$ is

$$F_{\text{wall}} = \sum_{\text{all cells}} \frac{\rho \forall_{\text{cell}} |\mathrm{V}_y| \mathrm{V}_y L^2 \text{sign}(\mathrm{V}_{\vec{n}})}{\forall_{\text{wall}}} \tag{4.12}$$

where $\mathrm{V}_{\vec{n}}$ is the velocity component normal to the outer box surface, and *all* sources of fluid momentum in the system are contained within the virtual box. The two sides of the box aligned with $\pm y$ present an added force component due to the pressure difference between them, which is trivially calculated by multiplying the mean pressure difference by L^2. Fig. 4.15 details a virtual box and the results of the sway maneuver test.

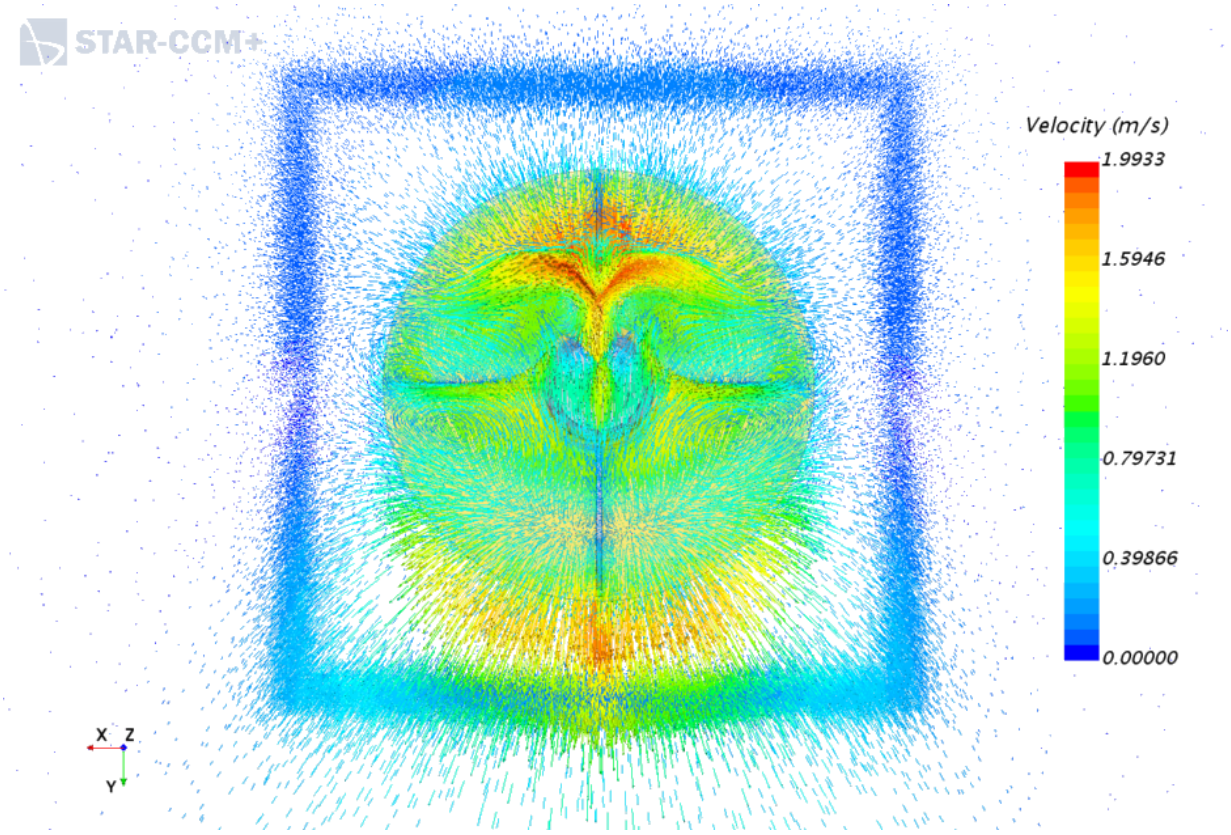

Figure 4.15. Vector graphic of dual-disk simulation with the virtual box for the sway maneuver.

From the CFD simulations, the total sway forces measured suggested the full-scale craft can output between 10% and 20% force in the sway direction that it can in the surge direction. This was confirmed through the physical force-validation model in Chapter 3.

4.4 Yaw and Roll-Moment Calculation

The larger significance of this chapter resides in the potential for the full-scale propulsor to generate *sway*-force on-demand, but it is still worth noting how we calculate the potential for the propulsor to generate *yaw* and *roll*-moments.

4.4.1 Yaw Moment

The yaw maneuver produces an identical input thrust distribution on each rotor as the sway maneuver, but the lack of significant hydrodynamic interference allows for any generated moment to be calculated directly from the input thrust distribution $\frac{dF}{dA}$ (Eqn. 4.11). This is done trivially by multiplying all points by lever-arm y before integrating across dA and setting $F_{RotorLim} = 1250$N. More specifically, the yaw-moment partial from *both* combined rotors is

$$dT_{yaw} = 2y \cdot dF \tag{4.13}$$

such that maximum yaw-moment T_{yaw} from both rotors is calculated through $\frac{dF}{dA}$ (Eqn. 4.11), but scaled to the maximum achievable surge-equivalent total thrust (thereby satisfying average torque equivalency per sweep) per rotor. The maximum achievable yaw-moment is

$$\begin{aligned} T_{yaw} &= 2 \iint_A y \frac{dF}{dA} dA = 4 \int_0^{\pi} \int_{R_i}^{R_o} \frac{dF}{dA} \sin(\theta_{\text{rot}}) \text{r}^2 d\text{r} d\theta_{\text{rot}} \\ &= 10 \int_0^{\pi} \int_{R_i}^{R_o} \frac{F_{RotorLim}(R_o - \text{r})}{R_o^5 + 5R_i^5 - 5R_o R_i^4} \sin^2(\theta_{\text{rot}}) \text{r}^4 d\text{r} d\theta_{\text{rot}} \approx 221.4 \text{ N-m} \end{aligned} \tag{4.14}$$

which should occur at command $\Gamma = 6.5\frac{\pi}{2} \approx 10.2$ degrees.

4.4.2 Roll Moment

The moment T_{roll} generated from command δ is, by definition, 2% the torque generated by each rotor under operating conditions, which is known to be 0.34 N-m per degree of δ.

4.5 Implementing Full-Scale Controller Modes

CFD simulations have provided enough information to construct a rudimentary 6-DOF open-loop model with unique parameters for each DOF on the full-scale propulsor. A 6-DOF controller based on this model is presented in Chapter 5. Open-loop control parameters are mapped to forces and torques for the full-scale propulsor:

$$\begin{bmatrix} F_{\mathrm{x}} \\ F_{\mathrm{y}} \\ F_{\mathrm{z}} \\ T_{\mathrm{x}} \\ T_{\mathrm{y}} \\ T_{\mathrm{z}} \end{bmatrix} = \begin{bmatrix} F_{surge} \\ F_{sway} \\ F_{heave} \\ T_{roll} \\ T_{pitch} \\ T_{yaw} \end{bmatrix} = \begin{bmatrix} 385 & 0 & 0 & 0 & 0 & 0 \\ 0 & 50 & 0 & 0 & 0 & 0 \\ 0 & 0 & 50 & 0 & 0 & 0 \\ 0 & 0 & 0 & 0.34 & 0 & 0 \\ 0 & 0 & 0 & 0 & 22.1 & 0 \\ 0 & 0 & 0 & 0 & 0 & 22.1 \end{bmatrix} \begin{bmatrix} \alpha \\ \Gamma_y \\ \Gamma_z \\ \delta \\ \beta_y \\ \beta_z \end{bmatrix} \tag{4.15}$$

We implement knowledge that the static Rotor Effort offset rests at 90% and all servos have a 90^o offset, and that all (-x) servos are fed the negative of their respective control angles. All control parameters are thus mapped to physical actuator commands:

$$\begin{bmatrix} +x \text{ Rotor Effort} \\ -x \text{ Rotor Effort} \\ +x \text{ “top” Servo Angle} \\ +x \text{ “b.r.” Servo Angle} \\ +x \text{ “b.l.” Servo Angle} \\ -x \text{ “top” Servo Angle} \\ -x \text{ “b.r.” Servo Angle} \\ -x \text{ “b.l.” Servo Angle} \end{bmatrix} = \begin{bmatrix} 90\% \\ 90\% \\ 90^{\mathrm{o}} \\ 90^{\mathrm{o}} \\ 90^{\mathrm{o}} \\ 90^{\mathrm{o}} \\ 90^{\mathrm{o}} \\ 90^{\mathrm{o}} \end{bmatrix} + \begin{bmatrix} 0 & 0 & 0 & -1 & 0 & 0 \\ 0 & 0 & 0 & 1 & 0 & 0 \\ 1 & 0 & -1 & 0 & 0 & -1 \\ 1 & \frac{\sqrt{3}}{2} & \frac{1}{2} & 0 & -\frac{\sqrt{3}}{2} & \frac{1}{2} \\ 1 & -\frac{\sqrt{3}}{2} & \frac{1}{2} & 0 & \frac{\sqrt{3}}{2} & \frac{1}{2} \\ -1 & 0 & -1 & 0 & 1 & 0 \\ -1 & -\frac{\sqrt{3}}{2} & \frac{1}{2} & 0 & \frac{-1}{2} & -\frac{\sqrt{3}}{2} \\ -1 & \frac{\sqrt{3}}{2} & \frac{1}{2} & 0 & \frac{-1}{2} & \frac{\sqrt{3}}{2} \end{bmatrix} \begin{bmatrix} \alpha \\ \Gamma_{\mathrm{y}} \\ \Gamma_{\mathrm{z}} \\ \delta \\ \beta_{\mathrm{y}} \\ \beta_{\mathrm{z}} \end{bmatrix}$$

The same control-parameter mapping is used in the physical small-scale force validation model, but was first conceived for the full-scale propulsor.

4.6 Conclusions

This chapter details the design and simulation of the full-scale omnidirectional UUV implementation, and gauges its ability to perform in turbulent environments inaccessible to traditional craft, as would be seen in many shallow environments that require inspection. Bi-directional blades were designed to maximize thrust while staying lengthy enough to exploit properties emerging from continuous counter-rotation, and generate lateral thrust as a standalone control parameter. This lateral control parameter was verified using STAR-CCM+ CFD software. Finally, an open-loop state-space model was designed linking all six control parameters to desired output forces and moments. These control parameters were also mapped to physical actuator outputs. The CFD simulations performed in this chapter were run prior to the physical testing of the small-scale model in Chapter 3, which verified the working principles behind their results.

Chapter 5

Underwater Vehicle Dynamics and Control

This chapter details how to thoroughly model and simulate trajectory for a full-scale UUV equipped with the proposed mechanism. Research involving methods for identifying hydrodynamic properties of AUV-profiled submersibles for simulation and control, as well as basic controller implementation are presented in this chapter. Some of the parameter-estimation methods presented utilize control surface deflection as controller input, which is typical for standard AUVs, but can be used for an omnidirectional UUV that is heavily optimized for performance at some particular nonzero design speed. Though our proposed propulsion device bypasses control surface-based force commands, it still possesses fundamental hydrodynamic hull-properties which must be calculated through the geometric and CFD-based methods provided in this chapter. Furthermore, while the proposed mechanism possesses a known 6-DOF uncoupled force controller, this chapter details the kinematics and dynamics behind actually plotting a trajectory for our design in an open environment. In this chapter, we demonstrate how full six-DOF simulation of the mechanism can be achieved in a straightforward manner through the work presented on AUV dynamics and kinematics.

Much of the content in this chapter was completed under the Virginia Tech Center for Marine Autonomy and Robotics and iSHIP lab with the intent of publication. Professors Stefano Brizzolara and Daniel Stilwell also hold publishing right to the content within this chapter, which can and should be published elsewhere. Some of the work is also adapted from [35] and [36].

5.1 Coordinate Systems

The coordinate systems and motion-states used throughout this study are shown in Figure 5.1. All motion-states are to be assumed in the body-frame of the craft. Dynamic equations of motion relating forces and moments to velocities and accelerations are also assumed in the craft's local body-frame, while the position and trajectory are in the world-frame. Direction z is oriented downwards in the world-frame, while sway-force Y acts in the craft's starboard direction . Body-frame velocities (u, v, w) are measured in m/s, while angular rates (p, q, r) are measured in rad/s.

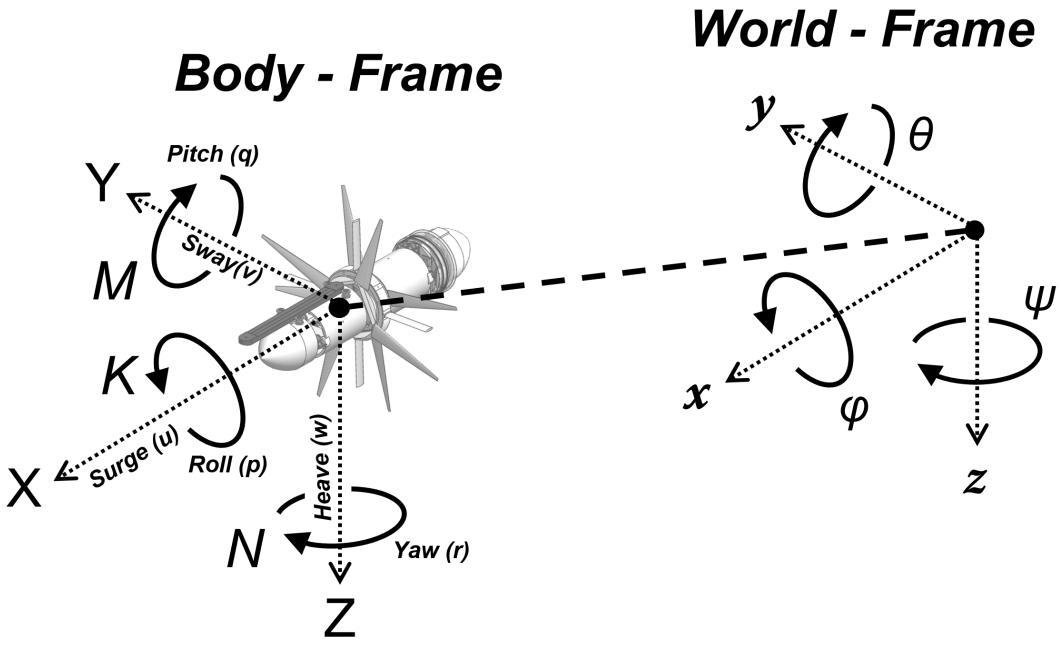

Figure 5.1. Coordinate systems and motion-state definitions.

A rudder command in the horizontal plane is defined as a single rudder angle δ_{r}. The physical implementation of yaw command onto multiple rear fins in various configurations is discussed later in Section 5.2.3. The sign-convention of virtual rudder angle δ_{r} [16] and horizontal side-slip trajectory angle ψ_{drift} are shown in Figure 5.2, which presents a top-view of an AUV.

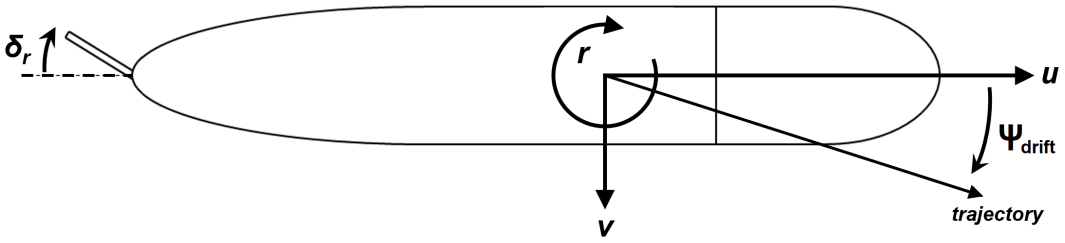

Figure 5.2. Top view of a moving AUV.

An elevator command in the vertical plane is defined as a single rudder angle δ_{e}. This may be aided by a supplemental elevator command δ_{c} sent to the canards. The physical implementation of pitch command δ_{e} onto multiple fins in various configurations is discussed later in Section 2.1. The sign-conventions of virtual rudder angles δ_{e} and δ_{c}, and the vertical side-slip trajectory angle θ_{drift} are presented in Figure 5.3 through a starboard-side view of a moving AUV.

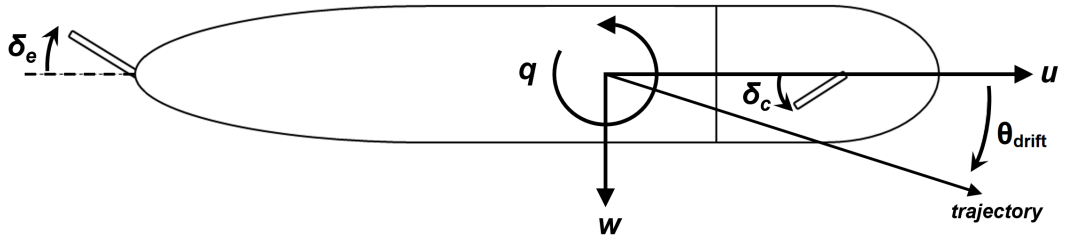

Figure 5.3. Starboard-side view of a moving AUV.

5.2 Fin-Angle Sign Convention and Implementation with Reference to Traditional Control-Commands, for any Number of Fins Protruding from a UUV

5.2.1 Control Surfaces and Omnidirectional UUVs

As is, the full-scale omnidirectional design presented in this study is completely optimized around bullard pull, as to be equally responsive along any two opposite directions. This particular omnidirectional vehicle design is therefore unlikely to benefit from adding control surfaces to its hull. However, rear fins and canards may bolster maneuverability

for an underwater rotorcraft optimized for movement *at speed*, at the expense of full omnidirectionality and agility under idle conditions. The use of added control surfaces on an omnidirectional UUV at speed may also help with noise reduction from the dynamic blades, and prove useful for stability at cruise velocity. Depending on the application and controller complexity, a future underwater rotorcraft design may benefit from some extent of control surfaces to improve maneuverability at some specific nonzero design velocity, while sacrificing low-speed agility.

A similar principle applies and is exploited by several dual blade rotorcraft, such as the Kamov Ka-25 dual-rotor attack helicopter shown in Figure 5.4.

Figure 5.4. [1] Control surfaces on the Kamov Ka-25 coaxial dual-rotor attack helicopter, assisting with maneuverability at speed at the expense of zero-speed turning agility.

As such, this chapter details how to thoroughly model and simulate *any* streamlined UUV from first-principles, and also explains how to implement and utilize control-surfaces. It is possible to simulate the trajectory of any UUV from the contents within this chapter.

5.2.2 Universal Sign Convention for Control Surface Actuation

For any control surface on the craft, positive angular deflection is defined via right-hand rule protruding from the craft. This principle is elaborated in Figure 5.5.

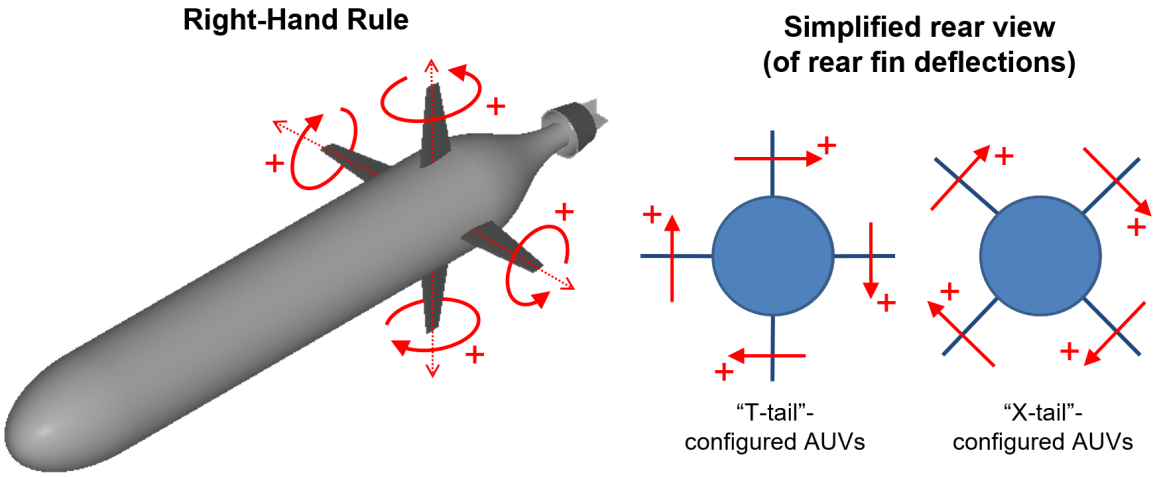

Figure 5.5. Sign convention for control surface angular deflections.

5.2.3 Implementation of Traditional Rudder Commands onto Rear Fins

On an X or T-tailed craft, any control-surface command causes all rear fins to deflect by the same angle δ given by the command, in the appropriate directions for the task. Figure 5.6 shows the simplified rear views (of rear fin deflections) during different control-commands on an X-tailed craft, detailing the implementation from controller commands to fin rotation.

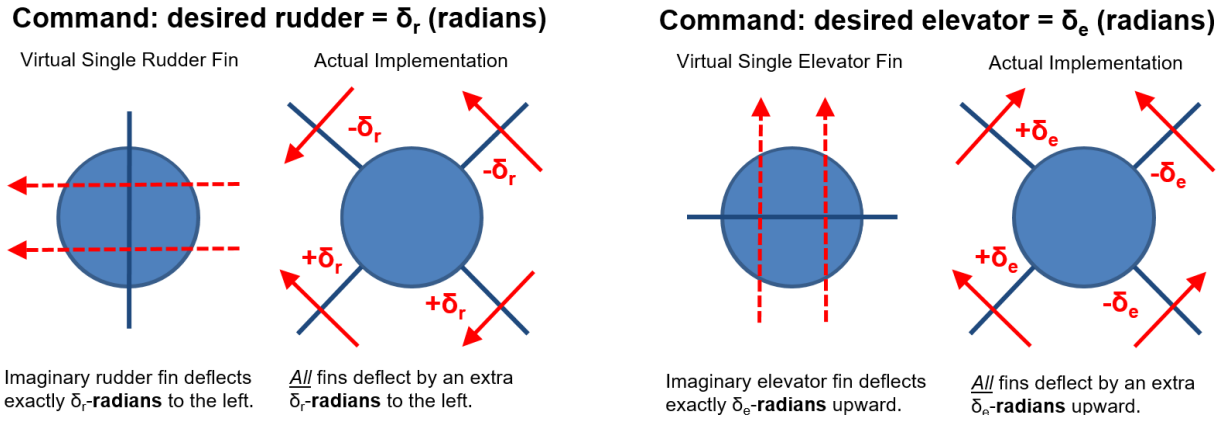

Figure 5.6. Implementation of δ_r and δ_e onto rear fins in an X-tailed UUV.

This trivial methodology for control surface actuation is used for the X and T-tail AUV

configurations presented in our study. For generic n-finned underwater vehicles, a universal approach is presented later in Section 5.2.8.

5.2.4 Rudder Command Roll Compensation (as Opposed to Roll Control)

We present a scenario where the trajectory needs to turn to the left and upward, but the craft has rolled by a nonzero angle ϕ. For any command combination ($\delta_{\text{r,desired}}$, $\delta_{\text{e,desired}}$), the roll can be compensated for in the body-frame to maneuver properly in the world-frame, as illustrated in Figure 5.7. Any "desired" turning command directions are in the world frame, while "actual" final turning commands are effectuated in the body frame of the craft.

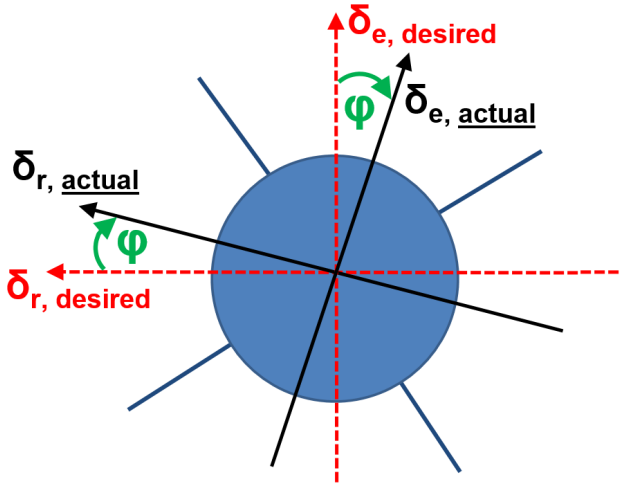

Figure 5.7. Simplified rear view of roll compensation in turning.

The final commands (δ_{r}, δ_{e}, δ_{c}) interpreted by the craft for control surface actuation are then

$$\delta_{\text{r}} = \delta_{\text{r,actual}} = \delta_{\text{r,desired}} \cos\phi - \delta_{\text{e,desired}} \sin\phi \tag{5.1}$$

$$\delta_{\text{e}} = \delta_{\text{e,actual}} = \delta_{\text{r,desired}} \sin\phi + \delta_{\text{e,desired}} \cos\phi$$

$$\delta_{\text{c}} = \delta_{\text{c,actual}} = \delta_{\text{c,desired}} \cos\phi$$

5.2.5 Roll Control

We can also control roll by adding a new parameter δ_{roll}. Unlike δ_{r} and δ_{e}, δ_{roll} is independent of current roll orientation ($\delta_{\text{roll}} = \delta_{\text{roll,desired}} = \delta_{\text{roll,actual}}$, always). Roll parameter δ_{roll} is manifested by deflecting all rear fins an extra δ_{roll} radians clockwise. A new coefficient $K_{uu\delta\text{roll}}$ is developed to describe the roll-moment on the craft due to roll-command δ_{roll}. $K_{uu\delta\text{roll}}$ is always defined as negative. The implementation of δ_{roll} onto control surfaces is shown in Figure 5.8.

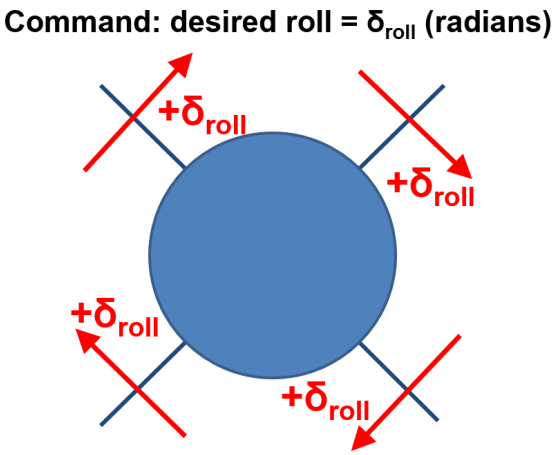

Figure 5.8. Implementation of roll control parameter δ_{roll} on rear control surfaces.

5.2.6 Control-Command Superposition on Rear Fins

Lateral forces and hull-moments from the rear fins scale linearly with fin deflection angle. Likewise, the net elevator force resulting from δ_{e} does not interfere with the net rudder force resulting from δ_{r}. The addition of constant offset δ_{roll} also does not interfere the total control surface forces resulting from δ_{r} and δ_{e}. Therefore, the fin deflections from δ_{r}, δ_{e}, and δ_{roll} can be superimposed to achieve yaw, pitch, and roll control simultaneously, as shown in Figure 5.9:

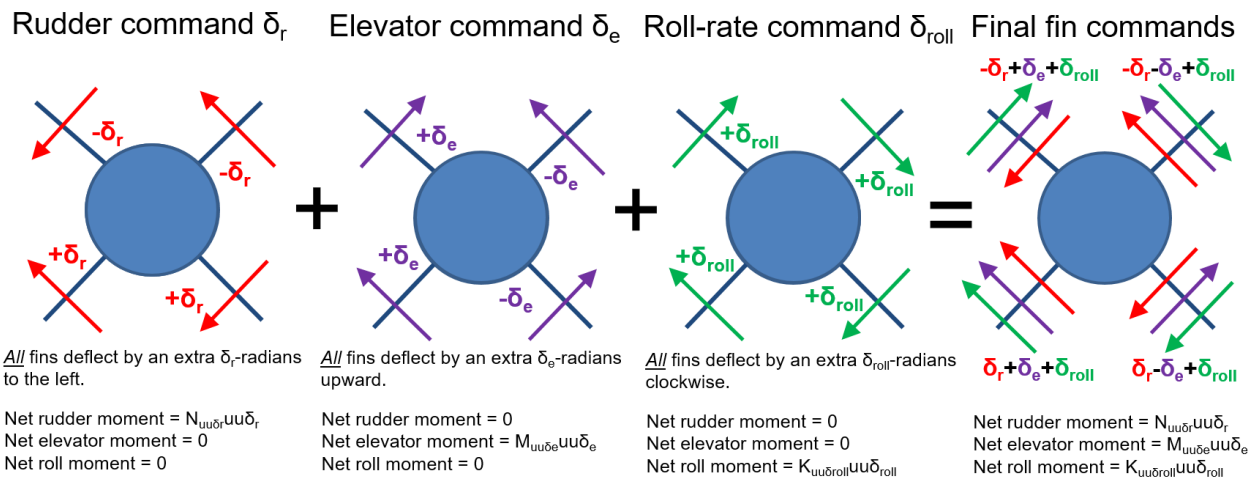

Figure 5.9. Implementation of simultaneous δ_{r}, δ_{e}, and δ_{roll} commands via superposition.

A superposition example is presented where the roll parameter is ignored for explanation purposes. If $\delta_{\mathrm{r}} = \delta_{\mathrm{e}} = 10$ degrees, we observe how pitch and yaw commands superimpose in Figure 5.10:

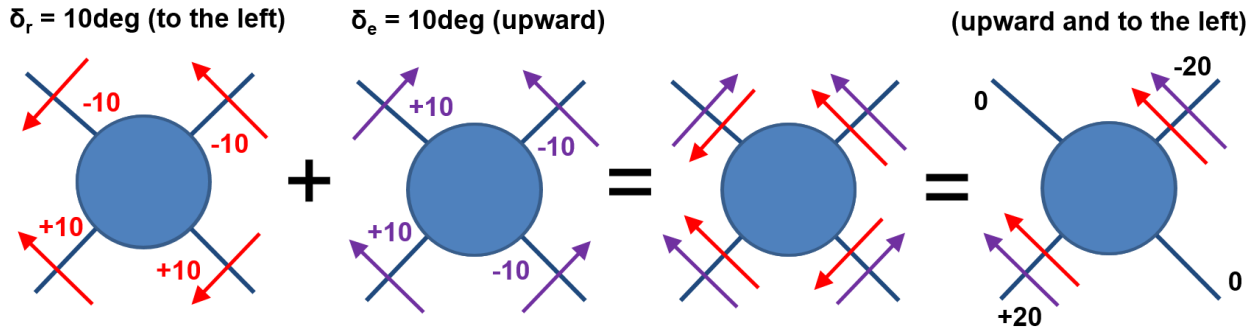

Figure 5.10. Conceptual example of simultaneous maneuvers $\delta_{\mathrm{r}} = \delta_{\mathrm{e}} = 10$ degrees.

Any fin angles exceeding the maximum allowable physical deflection saturate at the maximum allowable angle. Figure 5.11 presents pseudo-code that implements and saturates the final fin angles from control-commands on a four-fin X-tail configuration.

```
% Initially superimpose angle commands accordingly
% If X-tail Configuration                          % If T-tail Configuration
Top_Portside_Fin_Angle = -δr + δe + δroll           Top_Fin_Angle = -δr + δroll
Top_Starboard_Fin_Angle = -δr - δe + δroll          Bottom_Fin_Angle = δr + δroll
Bottom_Portside_Fin_Angle = δr + δe + δroll         Portside_Fin_Angle = δe + δroll
Bottom_Starboard_Fin_Angle = δr - δe + δroll        Starboard_Fin_Angle = - δe + δroll

% Then clip any angles surpassing an allowed limit
if   abs(fin_angle) >= (maximum_allowed_angle)
        fin_angle = sign(fin_angle)*maximum_allowed_angle
end
```

Figure 5.11. Pseudo-code implementation of δ_{r}, δ_{e}, and δ_{roll} commands onto control surfaces.

5.2.7 Reconstructing δ_{r}, δ_{e}, and δ_{roll} from Clipped Command Angles

The final effective commands δ_{r}, δ_{e}, and δ_{roll} must be reconstructed from clipped fin angles for control-force estimation. Because all the rudder forces (except along $\hat{x}$ in the body-frame) are linear with rudder angle, the final commands can be calculated straightforwardly, as shown for an X-tail configuration in Figure 5.12. This would be done for simulation and modelling purposes, as control forces and moments on the hull are calculated from δ-commands.

```
δr = mean([-Top_Portside_Fin_Angle, -Top_Starboard_Fin_Angle, Bottom_Portside_Fin_Angle, Bottom_Starboard_Fin_Angle]);
δe = mean([Top_Portside_Fin_Angle, -Top_Starboard_Fin_Angle, Bottom_Portside_Fin_Angle, -Bottom_Starboard_Fin_Angle]);
δroll = mean([Top_Portside_Fin_Angle, Top_Starboard_Fin_Angle, Bottom_Portside_Fin_Angle, Bottom_Starboard_Fin_Angle]);
```

Figure 5.12. Pseudo-code of the extraction of δ_{r}, δ_{e}, and δ_{roll} commands from clipped control-surface angles on an X-tailed UUV.

Likewise, pseudo-code for extracting δ-commands from clipped fin angles for a T-tailed UUV is shown in Figure 5.13:

```
δr = mean([-Top_Fin_Angle, Bottom_Fin_Angle]);
δe = mean([Portside_Fin_Angle, -Starboard_Fin_Angle]);
δroll = mean([Top_Fin_Angle, Bottom_Fin_Angle, Portside_Fin_Angle, Starboard_Fin_Angle]);
```

Figure 5.13. Pseudo-code of the extraction of δ_{r}, δ_{e}, and δ_{roll} commands from clipped control-surface angles on a T-tailed UUV.

Then lastly, we calculate the new X-forces by summing together the drag forces from each individual rear fin, as the X-force from each fin scales with the square the deflection angle. Assuming there are n rear-fins total, the force along $\hat{x}$ from any individual fin i with net angular deflection deflection δ_i is

$$\frac{1}{\mathrm{n}} X_{uu\delta\delta} u|u| \delta_i^2 \tag{5.2}$$

where the total control surface force along $\hat{x}$ due to all angular fin and canard deflections is then

$$\frac{1}{\mathrm{n}} X_{uu\delta\delta} u|u| \sum_{i=1}^{\mathrm{n}} \delta_i^2 + X_{uu\delta\delta_c} u|u| \delta_{\mathrm{c}}^2 \tag{5.3}$$

5.2.8 Generic Approach to Control-Command Implementation

A universal approach can be used to implement rudder commands onto rear fins in any arrangement. This generic methodology still applies if the number of tail fins n is odd or greater than 4, and is identical to our current T-tail control implementation. It would also work in replacement for our current X-tail control strategy. Parameters for the generalized approach for rudder-command implementation onto rear fins are outlined in Figure 5.14.

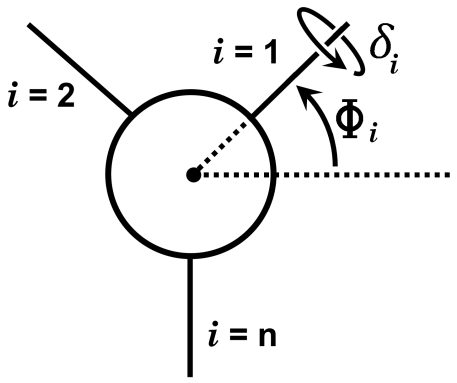

Figure 5.14. Simplified rear view and sign convention of a generic n-finned vehicle.

Before fin angle limits are considered, the angular deflection δ_i of any tail fin i is implemented as

$$\delta_i = -\delta_{\mathrm{r}} \sin(\Phi_i) - \delta_{\mathrm{e}} \cos(\Phi_i) + \delta_{\mathrm{roll}} \tag{5.4}$$

After fin angle saturation and clipping, control commands δ_{r}, δ_{e}, and δ_{roll} can be reconstructed from *relevant* clipped control-surface angles δ_i on any AUV tail configuration using the generalized approach.

$$\delta_{\mathrm{r}} = -\frac{1}{\mathrm{n_r}} \sum_{i=1}^{\mathrm{n}} \delta_i \csc(\Phi_i), \;\; \Phi_i \notin \{0, \pi\} \tag{5.5}$$

$$\delta_{\mathrm{e}} = -\frac{1}{\mathrm{n_e}} \sum_{i=1}^{\mathrm{n}} \delta_i \sec(\Phi_i), \;\; \Phi_i \notin \{\frac{\pi}{2}, \frac{3\pi}{2}\} \tag{5.6}$$

$$\delta_{\mathrm{roll}} = -\frac{1}{\mathrm{n}} \sum_{i=1}^{\mathrm{n}} \delta_i \tag{5.7}$$

where $\mathrm{n_r}$ is the number of rear fins that are not positioned at $\Phi_i = 0$ or $\Phi_i = \pi$, and $\mathrm{n_e}$ is the number of rear fins that are not positioned at $\Phi_i = \frac{\pi}{2}$ or $\Phi_i = \frac{3\pi}{2}$.

5.3 Kinematics

Referring back to Figure 5.1, the position of the AUV is now described with $\eta = [\eta_1^\top, \eta_2^\top]^\top$ where $\eta_1 = [x, y, z]$ is the location of the center of buoyancy of the AUV in an world reference frame and $\eta_2 = [\phi, \theta, \psi]$ is the set of Euler angles roll, pitch, and yaw that define orientation of the AUV relative to the world reference frame. The world-frame position vector η is then

$$\eta = [x, y, z, \phi, \theta, \psi]^\top \tag{5.8}$$

The velocity of the AUV is $\nu = [\nu_1^\top, \nu_2^\top]^\top$ where $\nu_1 = [u, v, w]$ is the set of body-relative velocities surge, sway, and heave, and $\nu_2 = [p, q, r]$ is the set of right-handed angular velocities about the positive X, Y, and Z axes of the body reference frame. The body-frame motion state vector ν is then

$$\nu = [u, v, w, p, q, r]^\top \tag{5.9}$$

In modeling and simulation, world-frame position vector η is integrated from $\dot{\eta}$. The derivative $\dot{\eta}$ is calculated and updated from the current body-frame motion-states vector ν and the last known orientation-components of η from the previous timestep (ϕ, θ, ψ):

$$J_1 := \begin{bmatrix} \cos(\psi)\cos(\theta) & \cos(\psi)\sin(\varphi)\sin(\theta) - \cos(\varphi)\sin(\psi) & \sin(\varphi)\sin(\psi) + \cos(\varphi)\cos(\psi)\sin(\theta) \\ \cos(\theta)\sin(\psi) & \cos(\varphi)\cos(\psi) + \sin(\varphi)\sin(\psi)\sin(\theta) & \cos(\varphi)\sin(\psi)\sin(\theta) - \cos(\psi)\sin(\varphi) \\ -\sin(\theta) & \cos(\theta)\sin(\varphi) & \cos(\varphi)\cos(\theta) \end{bmatrix}$$

$$J_2 := \begin{bmatrix} 1 & \sin(\varphi)\tan(\theta) & \cos(\varphi)\tan(\theta) \\ 0 & \cos(\varphi) & -\sin(\varphi) \\ 0 & \frac{\sin(\varphi)}{\cos(\theta)} & \frac{\cos(\varphi)}{\cos(\theta)} \end{bmatrix}$$

$$\dot{\eta} = \begin{bmatrix} J_1 & [\,0\,] \\ [\,0\,] & J_2 \end{bmatrix} \nu \tag{5.10}$$

5.4 Dynamics

The six-degree of freedom (DOF) equations of motion (EOM) [18] for the vehicle are

$$\underbrace{\big(M_{RB} - M_A\big)\dot{\nu}}_{\text{Mass + Added Mass}} + \underbrace{\big(C_{RB}(\nu) - C_A(\nu)\big)\nu}_{\text{Coriolis + Added Coriolis}} + \overbrace{D(\nu)\nu}^{\text{Friction + Damping}} + \underbrace{G(\eta)}_{\text{Gravitational Forces}} = \overbrace{\tau}^{\text{Control Forces}} \tag{5.11}$$

where the $M_{RB}\dot{\nu} + C_{RB}(\nu)\nu$ represents rigid-body dynamics. The terms $M_A\dot{\nu} + C_A(\nu)\nu$ are due to added mass, $D(\nu)\nu$ is due to hydrodynamic damping, $G(\eta)$ is due to gravity and buoyancy, and τ is due to control surfaces and propulsion.

5.4.1 Rigid-body Dynamics

From [17], the mass matrix M_{RB} in (5.11) is expressed

$$M_{RB} = \begin{bmatrix} m & 0 & 0 & 0 & mz_G & -my_G \\ 0 & m & 0 & -mz_G & 0 & mx_G \\ 0 & 0 & m & my_G & -mx_G & 0 \\ 0 & -mz_G & my_G & I_x & -I_{xy} & -I_{xz} \\ mz_G & 0 & -mx_G & -I_{yx} & I_y & -I_{yz} \\ -my_G & mx_G & 0 & -I_{zx} & -I_{zy} & I_z \end{bmatrix} \tag{5.12}$$

where m is the mass of the AUV and $C_G = [x_G, y_G, z_G]^\top$ is the center of mass of the vehicle with respect to the center of buoyancy. The moment of inertia components I_{ij} are computed directly using CAD software and vehicle geometries. If unavailable, the moments of inertia for a cylinder can instead be used to roughly approximate the moments of inertia of the vehicle body [4], from which $I_x = \frac{1}{2}m\mathrm{r}^2$, and $I_y = I_z = \frac{1}{12}m(3\mathrm{r}^2 + L^2)$ where r is the radius of the cylinder, L is the length, and the off-axis I_{ij} terms are ignored.

The Coriolis matrix $C_{RB}(\nu)$ in (5.11) is expressed

$$C_{RB}(\nu) = \begin{bmatrix} 0 & 0 & 0 & m(y_G q + z_G r) & -m(x_G q - w) & -m(x_G r + v) \\ 0 & 0 & 0 & -m(y_G p + w) & m(z_G r + x_G p) & -m(y_G r - u) \\ 0 & 0 & 0 & -m(z_G p - v) & -m(z_G q + u) & m(x_G p + y_G q) \\ -m(y_G q + z_G r) & m(y_G q) & m(z_G p) & 0 & -I_{yz} q - I_{xz} p + I_z r & I_{yz} r + I_{xy} p - I_y q \\ m(x_G q) & -m(z_G r + x_G p) & m(z_G q) & -I_{yz} q + I_{xz} p - I_z r & 0 & -I_{xz} r - I_{xy} q + I_x p \\ m(x_G r) & m(y_G r) & -m(x_G p + y_G q) & -I_{yz} r - I_{xy} p + I_y q & I_{xz} r - I_{xy} q - I_x p & 0 \end{bmatrix} \tag{5.13}$$

5.4.2 Added Inertia Dynamics

Under the assumption of approximate port/starboard symmetry and loose top/bottom symmetry, the only non-zero or non-negligible coefficients used for added inertia are

$$\{X_{\dot{u}}, Y_{\dot{v}}, Z_{\dot{w}}, K_{\dot{p}}, M_{\dot{q}}, N_{\dot{r}}, Y_{\dot{r}}, Z_{\dot{q}}\} \tag{5.14}$$

The added inertia matrix M_A in (5.11) is then

$$M_A = \begin{bmatrix} X_{\dot{u}} & 0 & 0 & 0 & 0 & 0 \\ 0 & Y_{\dot{v}} & 0 & 0 & 0 & Y_{\dot{r}} \\ 0 & 0 & Z_{\dot{w}} & 0 & Z_{\dot{q}} & 0 \\ 0 & 0 & 0 & K_{\dot{p}} & 0 & 0 \\ 0 & 0 & M_{\dot{w}} & 0 & M_{\dot{q}} & 0 \\ 0 & N_{\dot{v}} & 0 & 0 & 0 & N_{\dot{r}} \end{bmatrix} \tag{5.15}$$

From the way many of the coefficients are estimated, the star-coefficients in $D(\nu)$ that are derived via VPMM (see Section 5.5) already account for many of the commonly referenced terms in the added-Coriolis matrix C_A. For example, the term N^*_{ur} already accounts for all components multiplying $u \cdot r$ into N. Under the same loose symmetry assumptions used in M_A, while also avoiding force redundancies from $D(\nu)$, the added Coriolis matrix $C_A(\nu)$ in (5.11) is

$$C_A(\nu) = \begin{bmatrix} 0 & 0 & 0 & 0 & 0 & 0 \\ 0 & 0 & 0 & Z_{\dot{w}}w + Z_{\dot{q}}q & 0 & 0 \\ 0 & 0 & 0 & -Y_{\dot{v}}v - Y_{\dot{r}}r & 0 & 0 \\ 0 & -Z_{\dot{w}}w - Z_{\dot{q}}q & Y_{\dot{v}}v + Y_{\dot{r}}r & 0 & -N_{\dot{v}}v - N_{\dot{r}}r & M_{\dot{w}}w + M_{\dot{q}}q \\ 0 & 0 & 0 & N_{\dot{v}}v + N_{\dot{r}}r & 0 & -K_{\dot{p}}p \\ 0 & 0 & 0 & -M_{\dot{w}}w - M_{\dot{q}}q & K_{\dot{p}}p & 0 \end{bmatrix} \tag{5.16}$$

5.4.3 Hydrodynamic damping

Forces τ_D due to hydrodynamic damping in (5.11) are expressed $\tau_D = D(\nu)\nu$ where due to the assumptions of approximate top/bottom symmetry and loose port/starboard symmetry, the matrix of coefficients can be simplified to

$$D(\nu) = -\begin{bmatrix} X_{uu}|u| & 0 & 0 & 0 & 0 & 0 \\ 0 & Y_{vv}|v| + Y_{uv}u & 0 & 0 & 0 & Y_{rr}|r| + Y^*_{ur}u \\ 0 & 0 & Z_{ww}|w| + Z_{uw}u & 0 & Z_{qq}|q| + Z^*_{uq}u & 0 \\ 0 & 0 & 0 & K_{pp}|p| + K_{up}u & 0 & 0 \\ 0 & 0 & M_{ww}|w| + M^*_{uw}u & 0 & M_{qq}|q| + M^*_{uq}u & 0 \\ 0 & N_{vv}|v| + N^*_{uv}u & 0 & 0 & 0 & N_{rr}|r| + N^*_{ur}u \end{bmatrix} \tag{5.17}$$

5.4.4 Gravitational Restoring Forces and Moments

The effects of gravity and buoyancy are modelled

$$G(\eta) = 9.81 \cdot \begin{bmatrix} (m-B)\sin(\theta) \\ -(m-B)\cos(\theta)\sin(\phi) \\ -(m-B)\cos(\theta)\cos(\phi) \\ -(y_G m - y_B B)\cos(\theta)\cos(\phi) + (z_G m - z_B B)\cos(\theta)\sin(\phi) \\ (z_G m - z_B B)\sin(\theta) + (x_G m - x_B B)\cos(\theta)\cos(\phi) \\ -(x_G m - x_B B)\cos(\theta)\sin(\phi) - (y_G m - y_B B)\sin(\theta) \end{bmatrix} \tag{5.18}$$

where m is the mass of the submerged body, B is the buoyant displacement, $[x_G, y_G, z_G]^\top$ is the location of the center of gravity in the body frame, and $[x_B, y_B, z_B]^\top$ is the center of buoyancy in the body frame.

5.4.5 Control Forces and Moments

For control surfaces in any configuration, the effects of control surfaces and of the propulsor are modelled as

$$\tau = \begin{bmatrix} (\text{thrust}) + \frac{1}{\text{n}} X_{uu\delta\delta} u|u| \sum_{i=1}^{\text{n}} \delta_i^2 + X_{uu\delta\delta c} u|u|\delta_c^2 \\ Y_{uu\delta_r} u|u|\delta_{\text{r}} \\ Z_{uu\delta_e} u|u|\delta_{\text{e}} + Z_{uu\delta_c} u|u|\delta_{\text{e}} \\ K_{uu\delta\text{roll}} u|u|\delta_{\text{roll}} \\ M_{uu\delta_e} u|u|\delta_{\text{e}} + M_{uu\delta_c} u|u|\delta_{\text{e}} \\ N_{uu\delta_r} u|u|\delta_{\text{r}} \end{bmatrix} \tag{5.19}$$

where the virtual control surfaces δ_{r}, δ_{e}, and δ_{roll} have been reconstructed from physical fin deflections in accordance with Section 5.2.7. Constant n represents the number of rear control surfaces, and δ_i is the deflection angle of an individual rear control surface indexed i, also described in Section 5.2.7. Virtual control surface δ_{e} is the canard angle deflection command sent to all canards, described in Section 5.1. This implementation of τ is intended to also work along -u, accounting for potential vehicle bidirectionally.

5.4.6 Mass and Payload Distribution

Our UUVs are designed to be on the order of 0.2% buoyant. Any encapsulated water in the craft (inside pockets, etc.) is considered to be part of the hull dynamically, so enclosed water is treated as part of rigid-body mass and moment of inertia. The center of buoyancy should be above the center of gravity for proper orientation-restoring forces, and the [0,0,0] point is located at the center of buoyancy, not gravity, of the craft. Making the separation distance between buoyancy and gravity centers too large primarily hinders maximum pitch capability, while minimally affecting yaw-axis performance.

5.4.7 Final Update Laws

The final update laws used in dynamic modeling are then constructed from Equations (5.10) and (5.11):

$$\dot{\nu} = \big[M_{RB} - M_A\big]^{-1}\big[\big(C_A(\nu) - C_{RB}(\nu)\big)\nu - D(\nu)\nu - G(\eta) + \tau\big] \tag{5.20}$$

$$\dot{\eta} = \begin{bmatrix} J_1(\eta) & [\ 0\ ] \\ [\ 0\ ] & J_2(\eta) \end{bmatrix} \nu$$

where $J_1(\eta)$ and $J_2(\eta)$ are defined in Equation (5.10).

5.5 Hydrodynamic Coefficient Estimation

Hydrodynamic 6-DOF hull coefficient estimation is based primarily on virtual maneuvers performed in the isolated horizontal plane (yaw axis). Although some of the pitch-axis coefficients are symmetric with their yaw-axis counterparts, pitch axis hull coefficients are estimated by preforming the same yaw-axis maneuvers with the craft listed 90° on its side. The process for estimating horizontal plane coefficient estimation will be detailed thoroughly, followed by a straightforward method to repeat the process for pitch-axis coefficient estimation. In restricting our attention to maneuvers in the horizontal plane, only three differential equations are written for the three degrees of freedom in that plane: surge, sway and yaw.

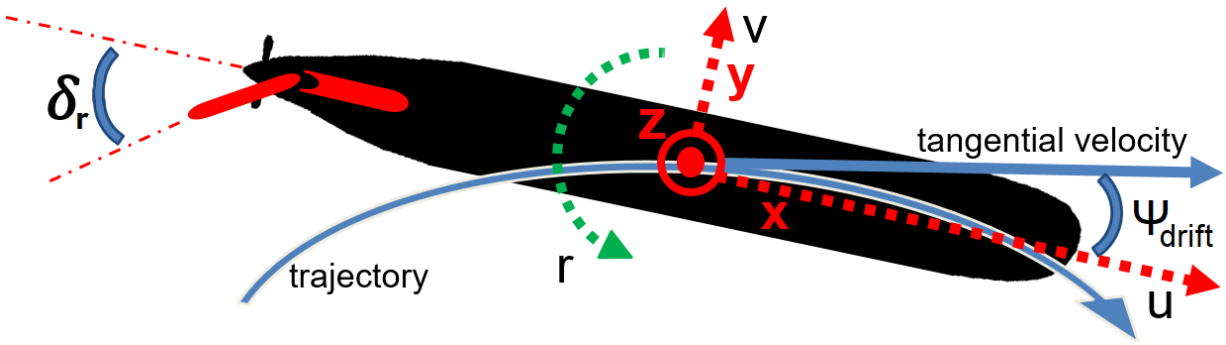

Figure 5.15. Overview of relevant planar-motion parameters.

Surge velocity u is defined along the x body axis direction, sway velocity v is along y, and yaw rotation rate r is about z. The body reference frame is centered in the vehicle center of buoyancy.

The motion of a UUV confined to the horizontal plane [27, 18] can be represented with the following system of lumped-parameter differential equations:

$$(\dot{u} - vr - x_G r^2)M = X_{ext} + X_{\dot{u}}\dot{u} + X_{uu}u|u| + X_{uu\delta\delta}u|u|\delta_{\mathrm{r}}^2 \tag{5.21}$$

$$\begin{aligned}(\dot{v} + ur)M = {} & Y_{ext} + Y_{uv}uv + Y_{vv}v|v| + Y_{\dot{v}}\dot{v} + Y^*_{ur}ur \\ & + Y_{rr}r|r| + Y_{\dot{r}}\dot{r} + Y_{uu\delta_r}u|u|\delta_{\mathrm{r}}\end{aligned} \tag{5.22}$$

$$\begin{aligned}\dot{r}I_{zz} + (\dot{v} + ru)Mx_G = {} & N_{ext} + N^*_{uv}uv + N_{vv}v|v| + N_{\dot{v}}\dot{v} + N^*_{ur}ur \\ & + N_{rr}r|r| + N_{\dot{r}}\dot{r} + N_{uu\delta_r}u|u|\delta_{\mathrm{r}}\end{aligned} \tag{5.23}$$

where x_G is the x-coordinate of the center of gravity, and in this case the only additional external force is X_{ext} equal to the thrust delivered by the propeller, approximated to a constant magnitude equal to the drag at 4 knots, i.e. $X_{ext} = -X_{uu}2.06^2$. Coefficient Y^*_{ur} is the summation of all elements multiplying $u \cdot r$ into Y, accounting for both added-Coriolis and viscous damping effects. The sub-components of Y^*_{ur} are uncoupled from one-another in estimation and lumped-parameter model (LPM) implementation, allowing for such parameter grouping. Likewise, coefficients N^*_{ur} and N^*_{uv} comprise of all elements multiplying $u \cdot r$ and $u \cdot v$ into N, respectively.

5.5.1 Estimation of Hull Coefficients

Hull coefficients are estimated using virtual planar mechanism simulations, which are first-order unsteady CFD simulations [24] that replicate the maneuvers performed in captive tests on ship models in towing tanks using planar motion mechanisms (PMMs). *Virtual* PMM (VPMM) tests are conducted using time-resolved viscous flow K-Epsilon solvers, with the ability to consider for moving meshes, by prescribing body motions and calculating hydrodynamic pressure and shear force and moments on the moving body. Because the motion is prescribed, dry mass m and rotary inertia I_{zz} are not relevant for these tests.

Pure-Sway

Estimation of coefficients Y_{uv}, Y_{vv}, $Y_{\dot{v}}$, N^*_{uv}, N_{vv}, and $N_{\dot{v}}$ is based on measurement of lateral force Y and moment N in the captive *pure-sway* VPMM test, where the AUV hull (with appendages) is prescribed a constant surge velocity u and a pure sinusoidal sway motion with velocity $v(t)$. Yaw rotation rate r is fixed to zero. The magnitude of the sway oscillation amplitude is chosen to be on the order of a few percent of the AUV length, and the frequency is chosen to be 0.667Hz [11, 38]. The PMM frequency was chosen based in part on the results from a study performed in 2007 [38] that analyzed different VPMM oscillation frequencies for a craft of similar length and design speed. This oscillation frequency is low enough to circumvent frequency-dependence and is used in all VPMM tests. A timestep of 1ms guarantees sufficient samples per oscillation period. A snapshot of the pure-sway VPMM test is presented in Fig. 5.16.

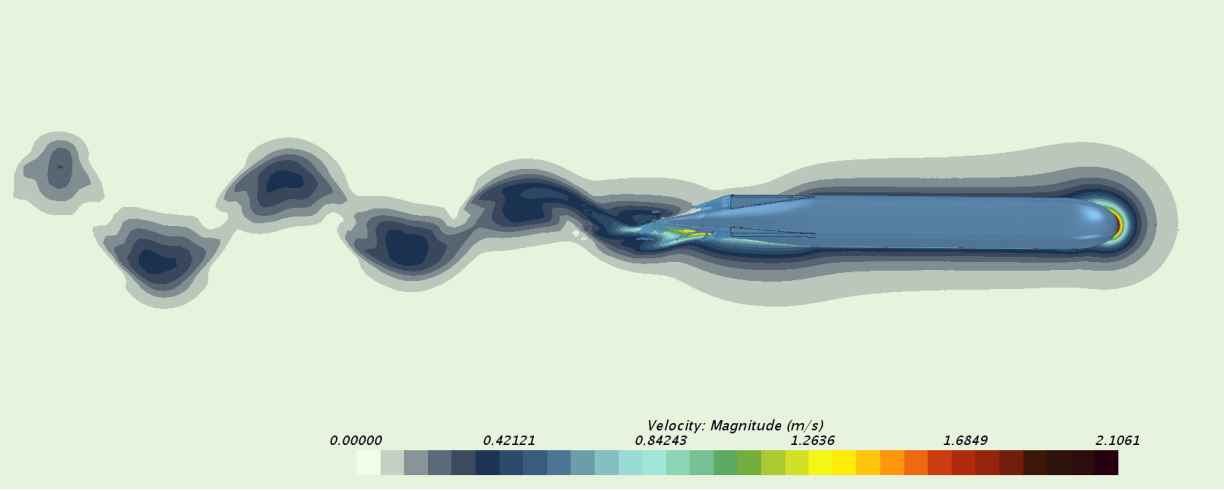

Figure 5.16. Induced velocity field (horizontal plane) in the fluid excited by the HII concept AUV undergoing the 10cm-amplitude pure-sway VPMM test.

The pure-sway VPMM is also run on our omnidirectional vehicle to estimate corresponding coefficients. A snapshot from the CFD pure-sway maneuver on the simplified

omnidirectional UUV hull is shown in Fig. 5.17.

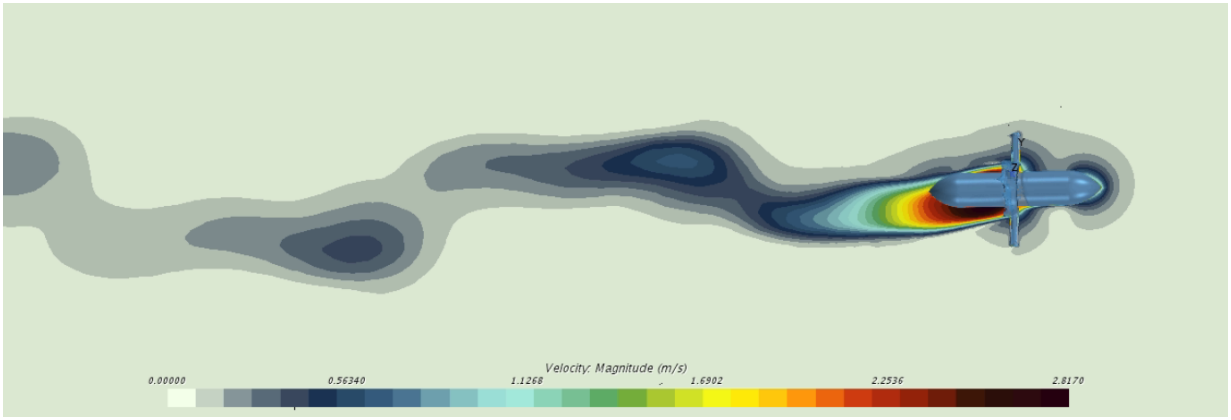

Figure 5.17. Induced velocity field (horizontal plane) in the fluid excited by the omnidirectional UUV undergoing the 3cm-amplitude pure-sway VPMM test.

For captive pure-sway VPMM tests, AUV dynamics (Eqs. 5.21-5.23) simplify to

$$Y_{\text{meas}}(t) = Y_{uv}u(t)v(t) + Y_{vv}v(t)|v(t)| + Y_{\dot{v}}(t)\dot{v}(t) \tag{5.24}$$

$$N_{\text{meas}}(t) = N^{*}_{uv}u(t)v(t) + N_{vv}v(t)|v(t)| + N_{\dot{v}}(t)\dot{v}(t) \tag{5.25}$$

where $Y_{\text{meas}}(t)$ is the unsteady hydrodynamic force component measured in the sway direction and $N_{\text{meas}}(t)$ is the unsteady moment induced by the hydrodynamic force in the yaw direction. In the sequel, explicit dependence on t is suppressed in our notation where doing so does not diminish clarity.

Pure sway VPMM tests are conducted for three separate sway amplitudes for better recursion during coefficient estimation. Figure 5.18 shows the concatenated output for the HII conceptual AUV.

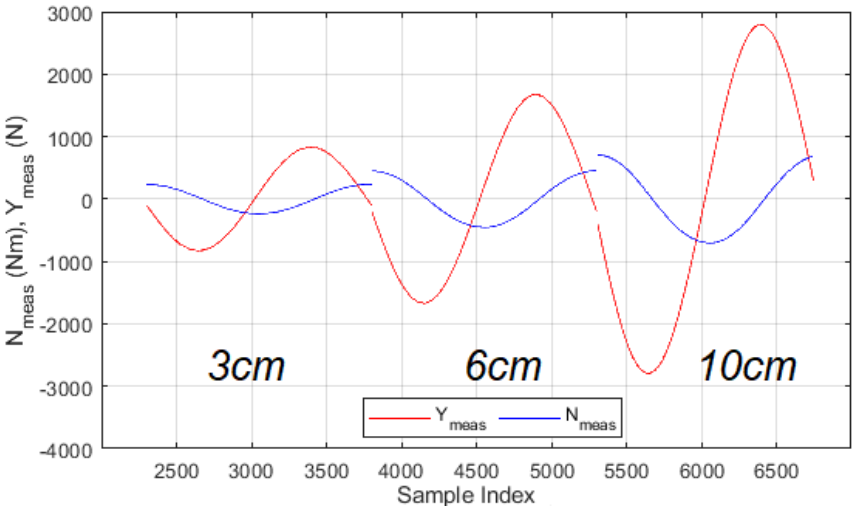

Figure 5.18. Pure-sway VPMM tests with three amplitudes (indicated in cm on the graph): calculated side force and yaw moment.

Data vectors corresponding to the time history of Y_{meas}, N_{meas}, uv, $v|v|$, and $\dot{v}$ are created by sampling each signal n times for each amplitude. The data vectors are then arranged with their three amplitude series concatenated one after another, in order to form 5 individual column vectors each with $3n$ elements $\overrightarrow{Y}_{\text{meas}}$, $\overrightarrow{N}_{\text{meas}}$, $\overrightarrow{uv}$, $\overrightarrow{v|v|}$, $\overrightarrow{\dot{v}}$, each in $\mathbb{R}^{3n}$. A new matrix V is created arranging the motion-state vectors one beside the other. Specifically, $V = \left[\overrightarrow{uv},\ \overrightarrow{v|v|},\ \overrightarrow{\dot{v}}\right] \in \mathbb{R}^{3nx3}$. The hydrodynamic coefficients are estimated

$$[Y_{uv}\ \ Y_{vv}\ \ Y_{\dot{v}}]^{\mathsf{T}} = V^{\dagger}\overrightarrow{Y}_{\text{meas}} \tag{5.26}$$

$$[N^{*}_{uv}\ \ N_{vv}\ \ N_{\dot{v}}]^{\mathsf{T}} = V^{\dagger}\overrightarrow{N}_{\text{meas}} \tag{5.27}$$

where $V^{\dagger} := (V^{\mathsf{T}}V)^{-1}V^{\mathsf{T}}$ is the pseudo-inverse of non-square matrix V.

The coefficients can be used to reconstruct Y and N to visualize the accuracy of the reduced-order AUV dynamics. In Fig. 5.19, measured forces and moments are compared with their coefficient-reconstructed counterparts.

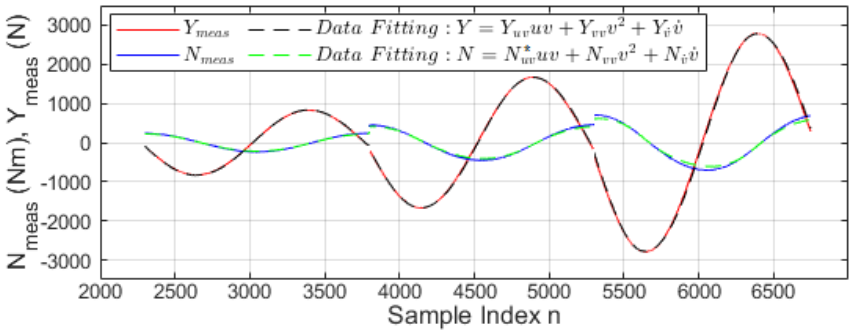

Figure 5.19. Pure-sway VPMM tests with three amplitudes.

Pure-Yaw

The hydrodynamic parameters that are dependent on the yaw rate, Y^*_{ur}, Y_{rr}, $Y_{\dot{r}}$, N^*_{ur}, N_{rr}, and $N_{\dot{r}}$, are identified from the *pure-yaw* VPMM test. This maneuver uses the same constant surge velocity with the same sinusoidal body-frame origin trajectory as the pure-surge maneuver, but a sinusoidal rotational speed is also prescribed such that the *sway* velocity v (measured in the body-frame) is always zero. Equivalently, the x-axis of the body-frame (see Fig. 5.15) remains tangent to the trajectory of the body-frame origin at all times. A snapshot of the pure-yaw VPMM test is presented in Fig. 5.20 for the HII concept AUV:

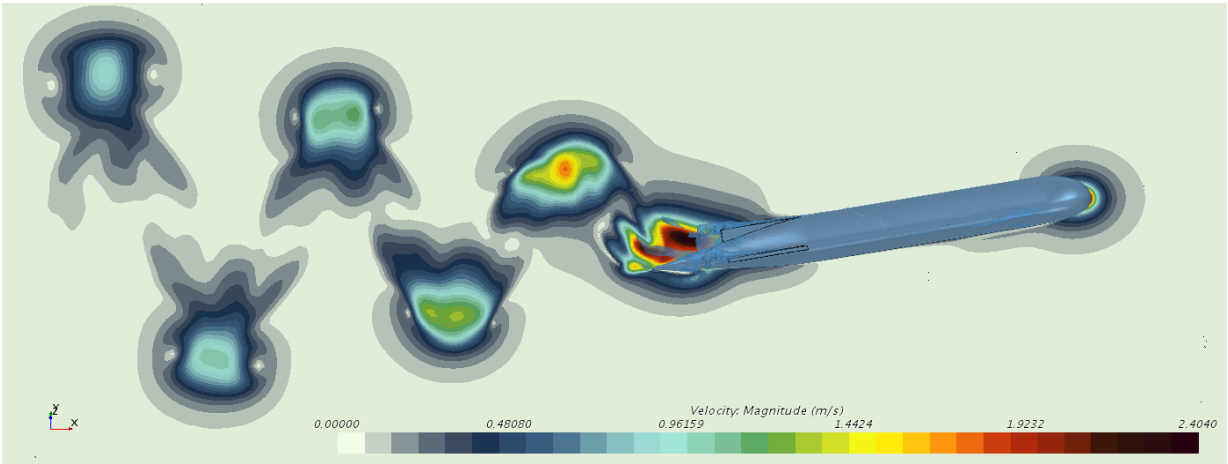

Figure 5.20. Induced velocity field (horizontal symmetry plane) in the fluid excited by the HII concept AUV undergoing the 10cm-amplitude pure-yaw VPMM test.

The pure-yaw VPMM is also run on our omnidirectional vehicle to estimate corresponding coefficients. A snapshot from the CFD pure-yaw maneuver on the simplified omnidirectional UUV hull is shown in Fig. 5.21.

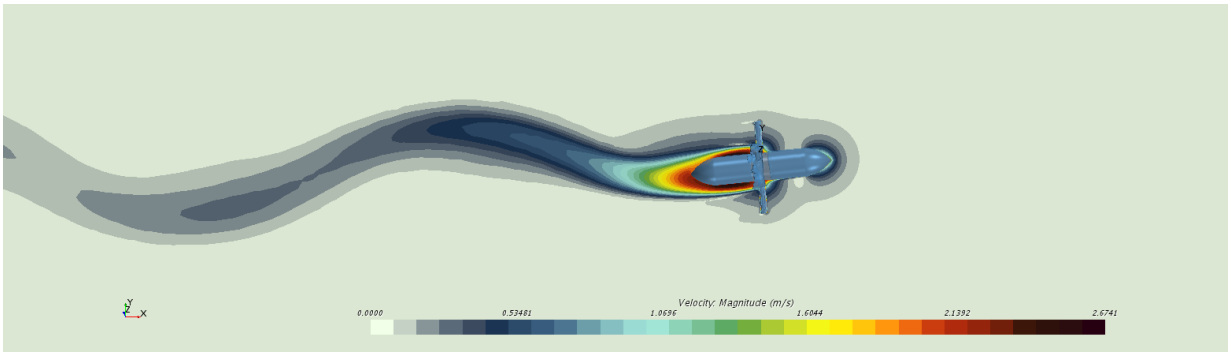

Figure 5.21. Induced velocity field (horizontal plane) in the fluid excited by the simplified omnidirectional UUV hull undergoing the 3cm-amplitude pure-yaw VPMM test.

For the pure-yaw VPMM trial, AUV dynamics (Eqs. 5.21-5.23) simplify to

$$Y_{\text{meas}} = Y^*_{ur} ur + Y_{rr} r|r| + Y_{\dot{r}} \dot{r} \tag{5.28}$$

$$N_{\text{meas}} = N^*_{ur} ur + N_{rr} r|r| + N_{\dot{r}} \dot{r} \tag{5.29}$$

The identification of the hydrodynamic coefficients in Eqs. 5.28-5.29 is performed similarly to the previous case. The times series of measurements of Y_{meas}, N_{meas}, ur, $r|r|$, and $\dot{r}$ are arranged as column vectors, and a new matrix $R = \left[\overrightarrow{ur}, \overrightarrow{r|r|}, \overrightarrow{\dot{r}}\right]$ is created. The hydrodynamic coefficients are estimated

$$[Y^*_{ur} \;\; Y_{rr} \;\; Y_{\dot{r}}]^\intercal = R^\dagger \overrightarrow{Y}_{\text{meas}} \tag{5.30}$$

$$[N^*_{ur} \;\; N_{rr} \;\; N_{\dot{r}}]^\intercal = R^\dagger \overrightarrow{N}_{\text{meas}} \tag{5.31}$$

where $R^\dagger := (R^\intercal R)^{-1} R^\intercal$ is the pseudo-inverse of non-square matrix R.

Pure-Surge

Estimation of coefficients X_{uu} and $X_{\dot{u}}$ is based on measurement of surge force X in the *pure-surge* VPMM maneuver, where the craft is prescribed only a time varying surge velocity $u(t)$ equal to the design velocity u_o plus a small sinusoidal perturbation with amplitude $0.05u_o$ and frequency 0.667Hz. The effects of sway and yaw are nonexistent here, so control surfaces should not be removed for this maneuver as to avoid measuring excess drag from the sockets of missing rudders. Instead, control surfaces are present and locked at zero-degrees. For the pure-surge VPMM test, AUV dynamics (Eq. 5.21) simplify to

$$X_{\text{meas}} = X_{uu}u|u| + X_{\dot{u}}\dot{u} \tag{5.32}$$

where X_{meas} is the measured surge-force. From a *single* times series of measurements, datapoints of $X_{\text{meas}}, u|u|$, and $\dot{u}$ are arranged as column vectors, and a new matrix $U = \left[\overrightarrow{u|u|}, \overrightarrow{\dot{u}}\right] \in \mathbb{R}^{nx2}$ is created. Hydrodynamic coefficients are estimated:

$$[X_{uu} \;\; X_{\dot{u}}]^{\mathsf{T}} = U^{\dagger}\overrightarrow{X}_{\text{meas}} \tag{5.33}$$

where $U^{\dagger} := (U^{\mathsf{T}}U)^{-1}U^{\mathsf{T}}$ is the pseudo-inverse of non-square matrix U.

VPMM Computational Setup

The VPMM computational meshes contain approximately 3 million cells each, with each element connected to the hull surface being approximately 0.2 percent the hull length. Figure 5.22 shows a cross-section of VPMM mesh cells near the surface of the AUV hull:

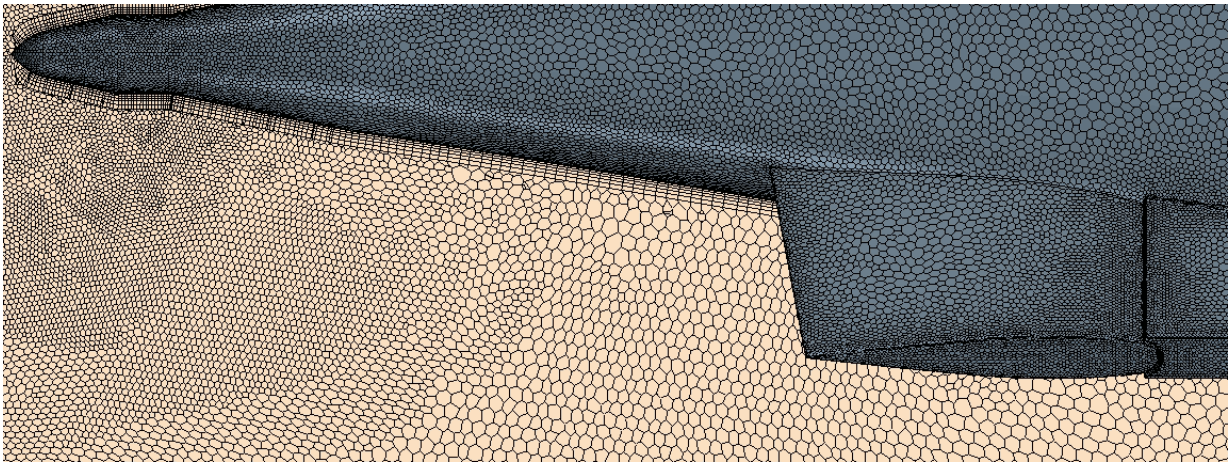

Figure 5.22. Cell density near the HII Concept-AUV tail for a VPMM test.

Likewise, Fig. 5.23 shows the cutout of cells for the simplified omnidirectional UUV hull:

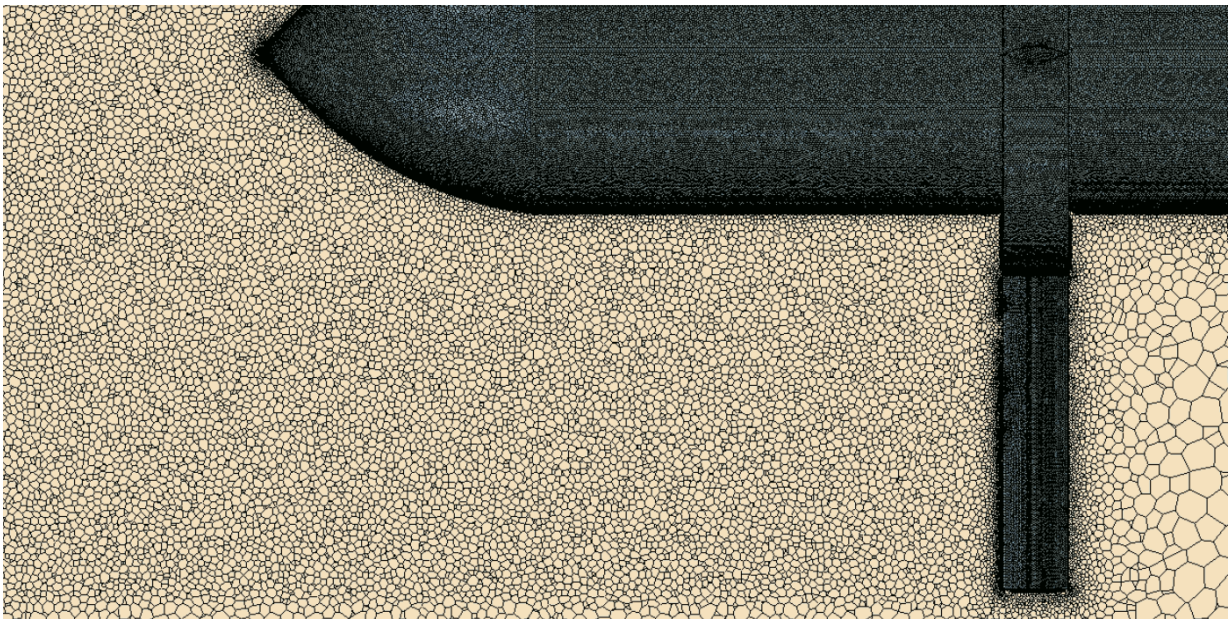

Figure 5.23. Cell density near the simplified omnidirectional UUV surface for a VPMM test.

Even finer meshes of 12 million cells were considered, and it was witnessed that meshes with 3 million cells saw no decrease in accuracy. The VPMM meshes are unstructured and highly refined around the hull, with 12 prism layers to capture boundary layer growth and separation and resolve vorticity shed in the near-field. The computational domain extends 15 meters ahead of the craft's starting position.

Our particular VPMM setup uses an inner moving mesh within the computational domain to emulate the planar motion trajectory, which requires the domain to extend far ahead of the craft for clearance. This approach is necessary for the pure surge maneuver, but is not required for the pure sway or pure yaw maneuvers, where it is possible to assign a fluid inflow velocity to the entire computational domain instead of having the hull physically move forward within the domain.

5.5.2 Estimation of Rudder Control Surface Coefficients

Control surface coefficients are estimated through virtual steady towing tests, with hull attack angle $\psi_{\text{drift}} = r = v = 0$ and constant vehicle surge velocity u. Virtual towing tests use the same computational cell density as the VPMM tests but do not require a moving mesh. Coefficients $N_{uu\delta_r}$, $Y_{uu\delta_r}$ and $X_{uu\delta\delta}$ are derived by analyzing N_{meas}, Y_{meas}, and X_{meas} at various constant rudder angles δ_{r}. For each virtual towing test, AUV dynamics (Eqs. 5.21-5.23) simplify significantly, such that only the following must be satisfied:

$$X_{\text{meas}} = X_{uu}u|u| + X_{uu\delta\delta}u|u|\delta_{\text{r}}^2, \quad X_{uu\delta\delta} < 0 \tag{5.34}$$

$$Y_{\text{meas}} = Y_{uu\delta_r}u|u|\delta_{\text{r}}, \quad Y_{uu\delta_r} > 0 \tag{5.35}$$

$$N_{\text{meas}} = N_{uu\delta_r}u|u|\delta_{\text{r}}, \quad N_{uu\delta_r} < 0 \tag{5.36}$$

The coefficient $X_{uu\delta\delta}$ is derived through evaluating $(X_{\text{meas}} - X_{uu}u|u|)$ at 0, 10, and 20-degree rudder angles. The resulting $X_{uu\delta\delta}u|u|\delta_{\text{r}}^2$ is then fitted to a square curve with respect to δ_{r}. The fitting is shown in Fig. 5.24. Coefficient $X_{uu\delta\delta}$ is always negative, measured in $\text{N}/(rad^2 \cdot (m/s)^2)$.

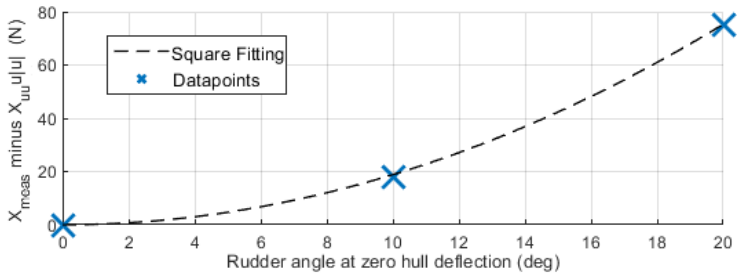

Figure 5.24. $X_{uu\delta\delta}u|u|\delta_r^2$ fitting via multiple CFD towing tests. Y-axis inverted for visual clarity.

Similarly, the coefficient $Y_{uu\delta_r}$ is derived through analyzing the *linear* relationship between Y_{meas} and δ_r at $\delta_r = 0$, 10, and 20-degrees, as shown in Fig. 5.25. $Y_{uu\delta_r}$ is equivalent to the slope divided by $u|u|$, and is always positive, measured in $\text{N}/(rad \cdot (m/s)^2)$.

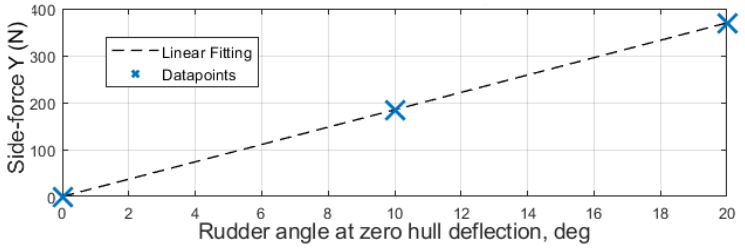

Figure 5.25. $Y_{uu\delta_r}u|u|\delta_r$ fitting via multiple CFD towing tests.

Likewise, $N_{uu\delta_r}$ is derived through analyzing N_{meas} about the center of buoyancy with respect to δ_r at $\delta_r = 0$, 10, and 20-degrees, shown in Fig. 5.26. $N_{uu\delta_r}$ is equivalent to the slope divided by $u|u|$ and is always negative for rear fins, measured in $\text{(N-m)}/(rad \cdot (m/s)^2)$.

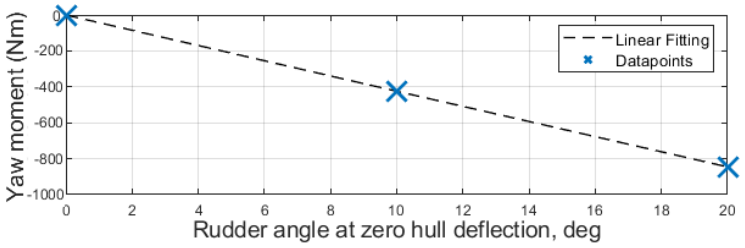

Figure 5.26. $N_{uu\delta_r}u|u|\delta_r$ fitting via multiple CFD towing tests.

5.5.3 Vertical Plane (Pitch-Axis) Coefficients

Coefficients related to the vertical plane are derived in a similar manner to those in the horizontal plane. With the same CFD setup, the craft is rotated 90°, and the same maneuvers are run on a (now vertical) plane.

Pitch-Axis Hull Coefficients

If the craft is symmetric along its pitch and yaw axes, the pitch-axis hull coefficients can be trivially estimated from their corresponding yaw-axis coefficients:

$$\begin{aligned}&[Z_{uw},\ Z_{ww},\ Z_{\dot{w}},\ M^*_{uw},\ M_{ww},\ M_{\dot{w}},\ \ Z^*_{uq},\ \ Z_{qq},\ \ Z_{\dot{q}},\ M^*_{uq}, M_{qq}, M_{\dot{q}}] \\ =\ &[Y_{uv},\ \ Y_{vv},\ \ Y_{\dot{v}}, -N^*_{uv}, -N_{vv}, -N_{\dot{v}}, -Y^*_{ur}, -Y_{rr}, -Y_{\dot{r}},\ N^*_{ur},\ N_{rr},\ N_{\dot{r}}]\end{aligned} \tag{5.37}$$

Otherwise, the craft must be listed 90°, and the *pure-sway* and *pure-yaw* VPMM trials must be re-run. Coefficients $[Z_{uw}, Z_{ww}, Z_{\dot{w}}, M^*_{uw}, M_{ww}, M_{\dot{w}}, Z^*_{uq}, Z_{qq}, Z_{\dot{q}}, M^*_{uq},\ M_{qq}, M_{\dot{q}}]$ are equivalent to new values $[Y_{uv}, Y_{vv}, Y_{\dot{v}}, -N^*_{uv}, -N_{vv}, -N_{\dot{v}}, -Y^*_{ur}, -Y_{rr}, -Y_{\dot{r}}, N^*_{ur}, N_{rr}, N_{\dot{r}}]$ estimated from the new 90°-listed VPMM trials.

Elevator Control Surface Coefficients

If the control surfaces of the craft are symmetric along its pitch and yaw axes, the elevator control surface coefficients can be trivially estimated from their corresponding rudder coefficients:

$$\begin{bmatrix} Z_{uu\delta_e} \\ M_{uu\delta_e} \end{bmatrix} = \begin{bmatrix} Y_{uu\delta_r} \\ -N_{uu\delta_r} \end{bmatrix} \tag{5.38}$$

Otherwise, the craft must be rotated $+90^{\circ}$ in ϕ and the virtual steady towing tests must be re-run on the newly-listed craft. Coefficients $(Z_{uu\delta_e}, M_{uu\delta_e})$ are equivalent to new values $(Y_{uu\delta_r}, -N_{uu\delta_r})$ that were estimated from the new 90°-listed virtual steady towing tests.

Canard Control Surface Coefficients

Canard control surface coefficients $X_{uu\delta\delta_c}$, $Z_{uu\delta_c}$, and $M_{uu\delta_c}$ are derived in a manner similar to that of $X_{uu\delta\delta}$, $Y_{uu\delta_r}$, and $N_{uu\delta_r}$, respectively. As with the rear control surfaces, the force along $\hat{x}$ resulting from canard deflection angle δ_c scales with the square of the deflection angle. Therefore, the method for estimating the coefficient $X_{uu\delta\delta_c}$ is identical to that of the coefficient $X_{uu\delta\delta}$, except instead of the datapoints $\delta_{\mathrm{r}} = 0$, 10, and 20-degrees, the datapoints $\delta_{\mathrm{e}} = 0$, 10, and 20-degrees are tested on the canards. As with $X_{uu\delta\delta}$, the coefficient $X_{uu\delta\delta c}$ is always negative.

Likewise, the force Z and moment M resulting from canard deflection scale linearly with canard angle δ_{e}, making the estimation of coefficients $Z_{uu\delta_c}$ and $M_{uu\delta_c}$ practically identical to the estimation of coefficients $Y_{uu\delta_r}$ and $N_{uu\delta_r}$, respectively. The datapoints $\delta_{\mathrm{e}} = 0$, 10, and 20-degrees are tested in a virtual towing tank environment, and a regression line is constructed. For front canards, coefficient $Z_{uu\delta_c}$ is always negative, and coefficient $M_{uu\delta_c}$ is always positive.

5.5.4 Roll Coefficients

Roll coefficients can be approximated trivially using other known control-surface coefficients, or estimated accurately using special virtual towing-tank tests.

Estimation of Control Surface Roll Coefficient $K_{uu\delta\text{roll}}$

If the average radial distance x_F between the roll-axis of the hull and center or pressure of the rudders is known, $K_{uu\delta\text{roll}}$ can be approximated as

$$K_{uu\delta\text{roll}} \approx -2Y_{uu\delta_r} x_F \tag{5.39}$$

Otherwise, another virtual towing-tank test must be run, with all control fins equally deflected clockwise in accordance with Figure 5.8. The roll moment K is measured at various δ_{roll} commands. $K_{uu\delta\text{roll}}$ is derived through analyzing the linear relationship between roll moment K_{meas} and δ_{roll} at $\delta_{\text{roll}} = 0^{\text{o}}$, 10^{o}, and 20^{o}, as shown in Fig. 5.27. $K_{uu\delta\text{roll}}$ is equivalent to the slope divided by $u|u|$, and is always negative, measured in (N-m)/$(rad \cdot (m/s)^2)$.

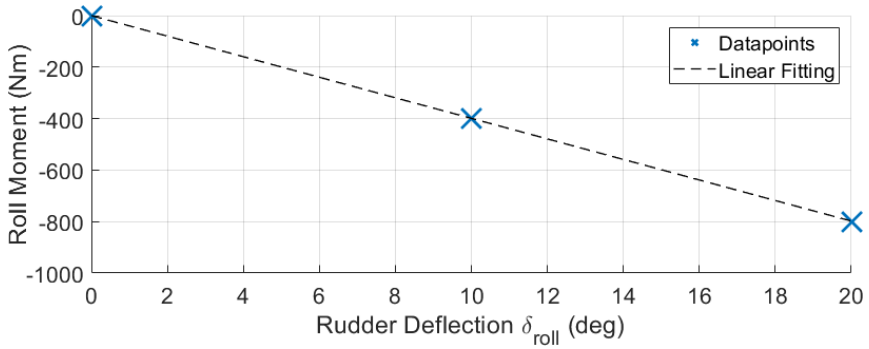

Figure 5.27. $K_{uu\delta\text{roll}}$ fitting via multiple CFD towing tests.

Estimation of Hull Coefficients K_{up}, K_{pp}, and $K_{\dot{p}}$

As a first approximation, the coefficients (K_{up}, K_{pp}, $K_{\dot{p}}$) which represent the hydrodynamic resistance to roll can be approximated using sway coefficients originally obtained from the virtual *pure-sway* maneuver. For a symmetric vehicle in sway, the roll moment on the isolated top half of the craft should be approximately half the total sway force multiplied by some moment-arm. The use of a moment-arm implies the moment can be generated with a virtual point-force. The location of this point-force is assumed to be near the outer radius of the craft, as the point-torque distribution should naturally increase with radial distance (leverage). For a ballpark estimate, we simply place the moment-arm on the effective outer radius x_R of the hull. The isolated roll-moment from the top half of a craft in sway is then approximated as half the total sway force multiplied by the craft's outer radius.

In context, we understand that a roll-induced virtual sway is also occurring in the tangential plane, where the overall magnitude of roll moment K can be reconstructed from two separate tangential projections on the separate planes. Furthermore, the magnitude of side-slip velocity across the entire skin of a rolling vehicle is its effective radius x_R multiplied by the roll rate p. The roll moment can therefore be estimated as four times the moment from the isolated top half of the vehicle in sway, where the *sway* is actually a virtual side-slip velocity induced by roll. The roll coefficients K_{up}, K_{pp}, and $K_{\dot{p}}$ are then roughly approximated as

$$\begin{aligned} K_{up} &\approx 2\ x_R^2\ Y_{uv} \\ K_{pp} &\approx 2\ x_R^2\ Y_{vv} \\ K_{\dot{p}} &\approx 2\ x_R^2\ Y_{\dot{v}} \end{aligned} \tag{5.40}$$

For a typical roll-stable craft which is not expected to roll considerably, it is only im-

portant that K_{up}, K_{pp}, and $K_{\dot{p}}$ are the correct sign and relative order of magnitude to achieve full modeling accuracy. Further refinement of the roll coefficients appears to have a non-existent or negligible role in simulation accuracy when within the correct order of magnitude. Therefore, for the majority of AUVs and submersibles, roll coefficient approximation via Equation (5.40) is adequate.

For the highest achievable roll accuracy, especially for crafts intended to adopt roll control, a more thorough CFD-based approach can be taken to obtain accurate values for the coefficients K_{up}, K_{pp}, and $K_{\dot{p}}$. These three coefficients can be accurately identified from the *pure-roll* virtual motion maneuver. This maneuver operates with a constant surge inflow velocity u_o, where a sinusoidal roll rotation is also prescribed. The roll rotation amplitude is chosen to be 10^{o} at a frequency of 0.667Hz. CFD mesh refinement is similar to the mesh used the VPMM maneuvers, but the computational domain does not need to extend as far ahead of the craft, as a constant inflow velocity can be assigned without the craft progressing in position along $\hat{x}$. For the pure-roll motion mechanism test, relevant AUV dynamics simplify to

$$K_{\text{meas}} = K_{up}up + K_{pp}p|p| + K_{\dot{p}}\dot{p} \tag{5.41}$$

where K_{meas} is the measured roll-moment. From a single times series of measurements, datapoints of K_{meas}, up, $p|p|$, and $\dot{p}$ are arranged as column vectors, and a new matrix $P = \left[\overrightarrow{up},\, \overrightarrow{p|p|},\, \overrightarrow{\dot{p}}\right]$ is created. Hydrodynamic coefficients are estimated:

$$[K_{up}\ \ K_{pp}\ \ K_{\dot{p}}]^{\mathsf{T}} = P^{\dagger}\,\overrightarrow{K}_{\text{meas}} \tag{5.42}$$

where $P^{\dagger} := (P^{\mathsf{T}}P)^{-1}P^{\mathsf{T}}$ is the pseudo-inverse of non-square matrix P.

5.6 Six-DOF Generic Underwater Vehicle Model Simulation and Construction

A 6-DOF open-loop UUV trajectory simulator is presented in Figure 5.28.

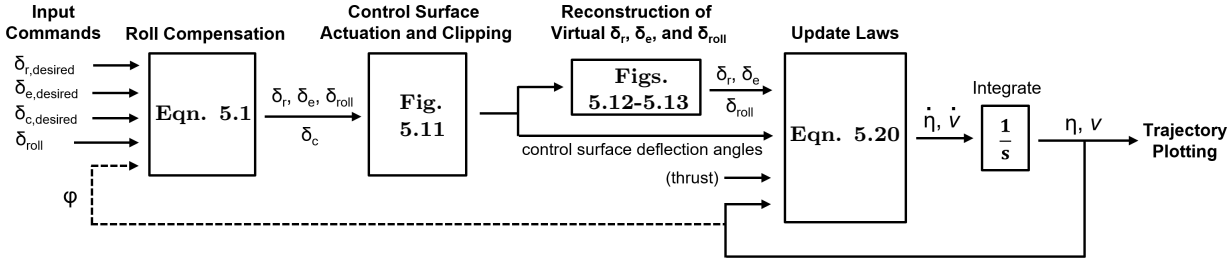

Figure 5.28. Full 6-DOF open-loop simulator layout for any UUV with control surfaces.

For the open-loop 6-DOF simulation, trajectory is plotted for rudder angle $\delta_{\mathrm{r}} = 10^{\mathrm{o}}$ at launch velocity $u_o = 2\mathrm{m/s}$ in Figure 5.32, over the course of 200 seconds. For visualization purposes, the $\hat{z}$ and $\hat{y}$-axes are now flipped such that $\hat{z}$ is oriented upwards. The craft is given a constant thrust equal to $-X_{uu}u_o^2$. During the turn-circle simulation, the craft evidently drifts upwards against gravity due to its 0.2% prescribed positive buoyancy.

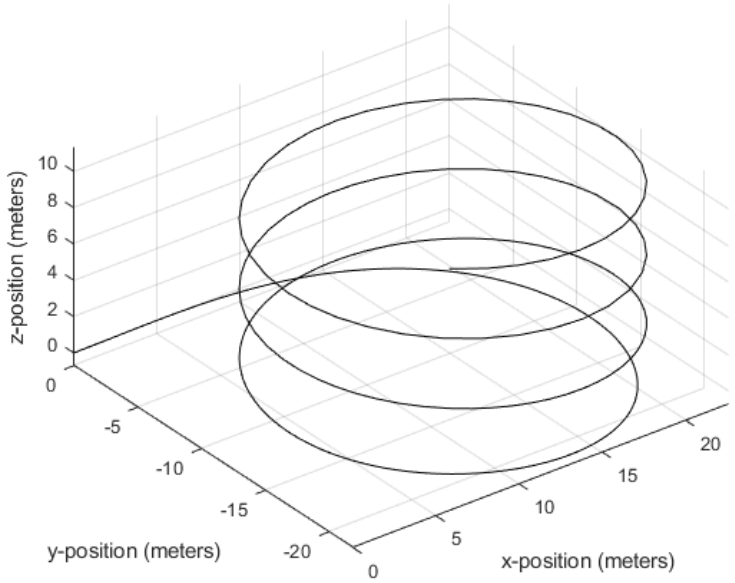

Figure 5.29. Full 6-DOF open-loop simulator trajectory output for an AUV.

By making a desired rudder command δ_{roll}, δ_{e}, or δ_{r} proportional to corresponding world frame orientations ϕ, θ, or ψ, respectively, closed-loop control can be achieved straightforwardly. Implementation of unity feedback in the yaw-axis, for example, is achieved by making the desired rudder command δ_{r} proportional to the negative of the difference between the yaw orientation ψ and a reference orientation ψ_{ref}, shown in Figure 5.30.

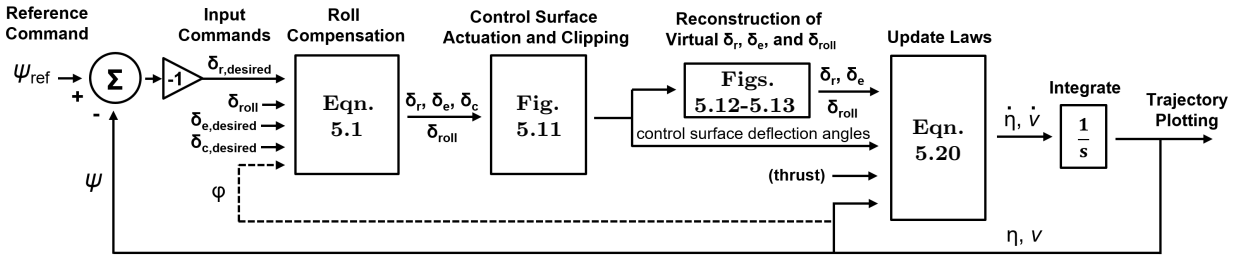

Figure 5.30. Full 6-DOF unity-feedback (yaw) closed-loop simulator.

Rudder angle δ_{r} is made proportional to the *negative* of the difference between the yaw orientation ψ and a reference yaw orientation ψ_{ref}, because by convention (Fig. 5.2), positive δ_{r} induces a negative moment about $\hat{z}$ (i.e. $N_{uu\delta_r} < 0$). The same inverse proportionality applies for roll control ($K_{uu\delta\mathrm{roll}} < 0$), but not for pitch-axis control ($M_{uu\delta_e}, M_{uu\delta_c} > 0$). A yaw controller C_ψ is implemented for horizontal-axis control, shown in Figure 5.31.

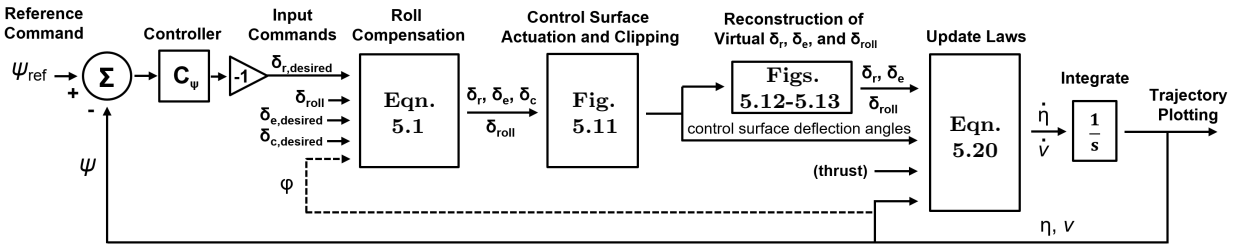

Figure 5.31. Full 6-DOF closed-loop simulator with yaw-control.

With basic proportional feedback implemented on yaw ($\mathrm{C}_\psi = 5$), trajectory is plotted for $\psi_{\mathrm{ref}} = 10^{\mathrm{o}}$ at launch velocity $u_o = 2\mathrm{m/s}$ in Figure 5.32 over the course of 70 seconds:

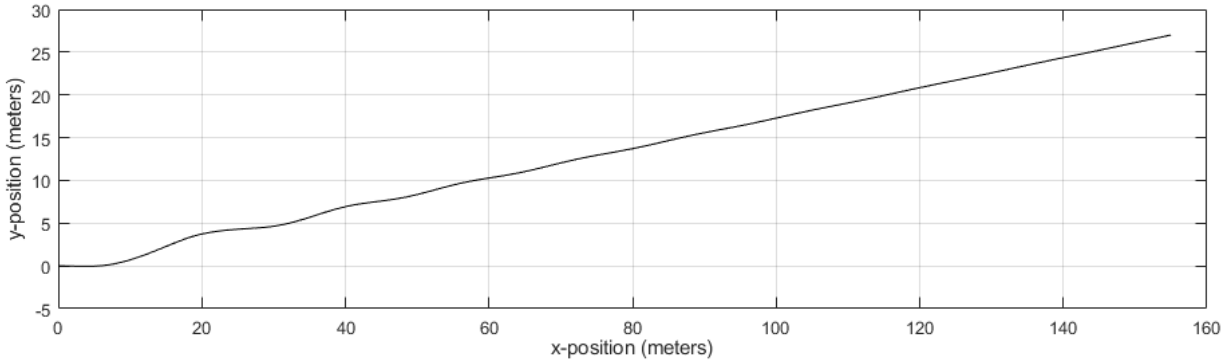

Figure 5.32. Full 6-DOF closed-loop simulator trajectory with simple proportional feedback in yaw.

5.7 Six-DOF Omnidirectional Propulsor Model Simulation and Construction

Because the omnidirectional mechanism UUV implementation does not rely on control surfaces for control-force input, 6-DOF simulation is greatly simplified. For the omnidirectional design, the control-force column vector τ (Eqn. 5.19) is directly implemented through the omnidirectional forces and moments generated by the propulsor. A 6-DOF open-loop omnidirectional UUV trajectory simulator is presented in Figure 5.33.

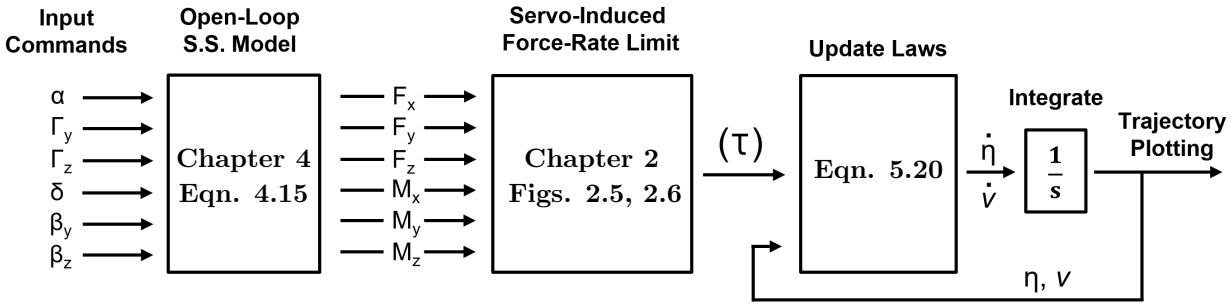

Figure 5.33. Full 6-DOF open-loop simulator for a full-scale omnidirectional propulsor UUV implementation.

By making the desired thrust effort in a given direction proportional to the difference between a reference state and a measured state, unity feedback can be applied straightforwardly. An example is shown in Figure 5.34, where surge-velocity or x-position unity feedback is applied in a trivial manner.

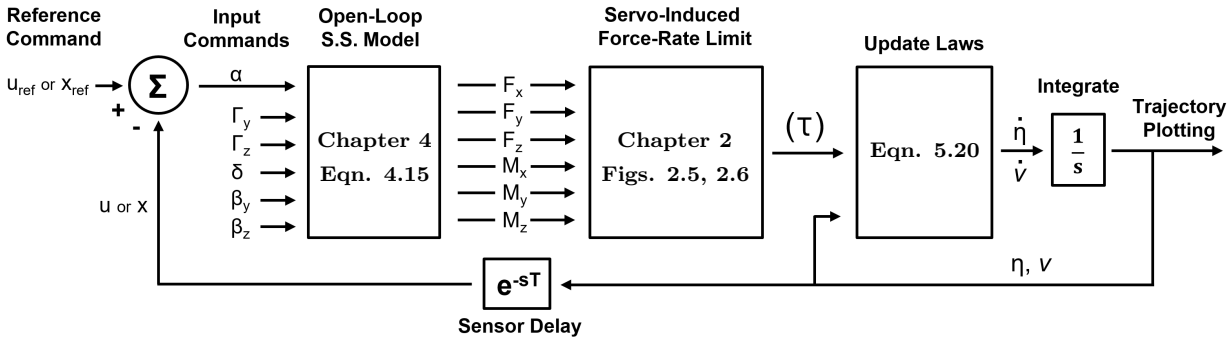

Figure 5.34. Full 6-DOF unity-feedback (surge) closed-loop simulator for a full-scale omnidirectional propulsor UUV implementation.

To actually maintain relative pose to a foreign object or any external reference-frame, feedback must be implemented along *all* axes to restrict orientation. A 6-DOF simulator is shown in Figure 5.35 which details the implementation of full-state unity position feedback in our model.

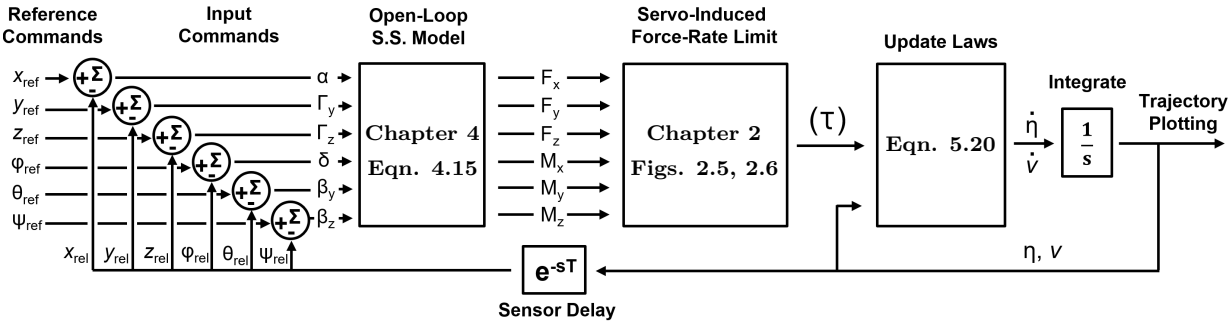

Figure 5.35. Full 6-DOF full-state feedback closed-loop simulator for a full-scale omnidirectional propulsor UUV implementation. Pose can be maintained relative to an observed external reference during operation using this position control method.

Individual axes controllers are situated to interpret the error between a reference position and an actual position. For example, Figure 5.36 shows the implementation of an $\hat{x}$-position controller C_α. Position control cannot be properly maintained if only one axis controller is active at a time, like what is shown in Figure 5.36. If orientation is allowed to drift and only one controller C_α is active, force in the body-frame $\hat{x}$-direction could be made proportional to the body-frame surge-velocity, but not to a reference-frame $\hat{x}$-position. For actively controlled position-feedback, controllers would need to be active on each DOF. Figure 5.36, though simplified, provides an adequate understanding of where each controller would be placed if implemented in Figure 5.35.

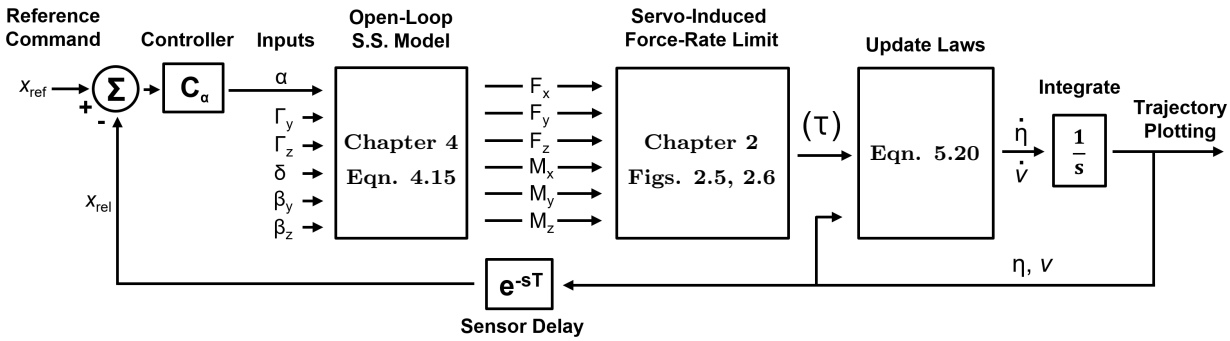

Figure 5.36. Full 6-DOF unity feedback closed-loop simulator with an active $\hat{x}$-position controller for a full-scale omnidirectional propulsor UUV implementation. Pose can be maintained relative to an observed external reference during operation using this position control method if all axes controllers are active.

Figure 5.37 shows the closed loop output with proportional control on all states over the course of six seconds. Non-zero input commands are u = 2 m/s, v = -1 m/s.

A closed-loop forced circular-maneuver can be run by setting reference inputs $u = 2$m/s, $v = 0$ m/s, and $r = \pi/4$ rad/s. Trajectory is plotted over the course of 8.1 seconds in Figure 5.38.

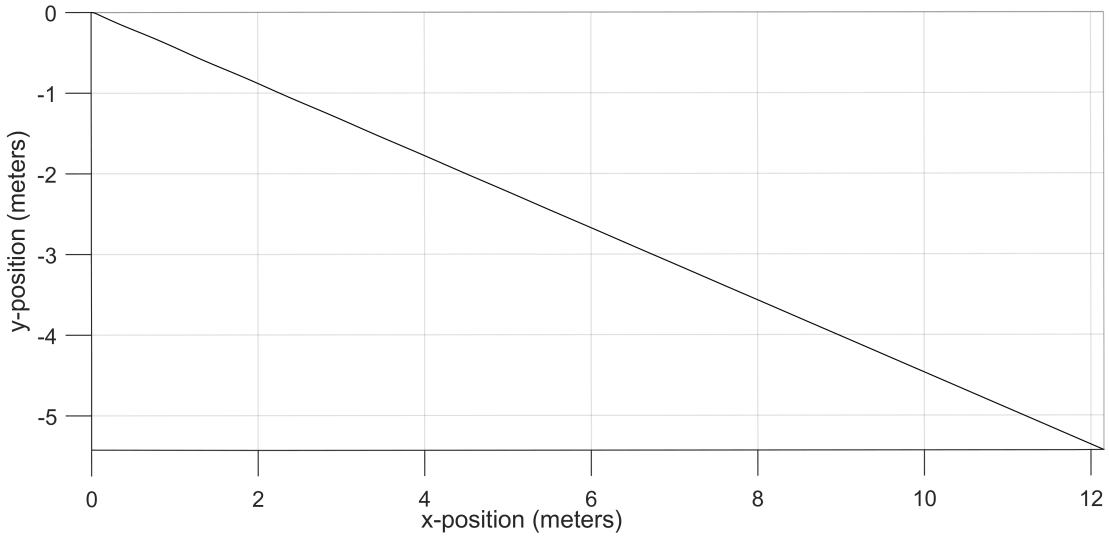

Figure 5.37. Full 6-DOF closed-loop simulation output for a full-scale omnidirectional propulsor UUV implementation with proportional feedback directed to surge and sway. The input reference commands are velocities $u = 2$, $v =$ -1, and other inputs are pose references set to zero. Linear position gains are set to 50, while angular position gains are set to 100. The lack of an integrator in this simple example prevents exact sway-velocity matching, but the proof of concept is met.

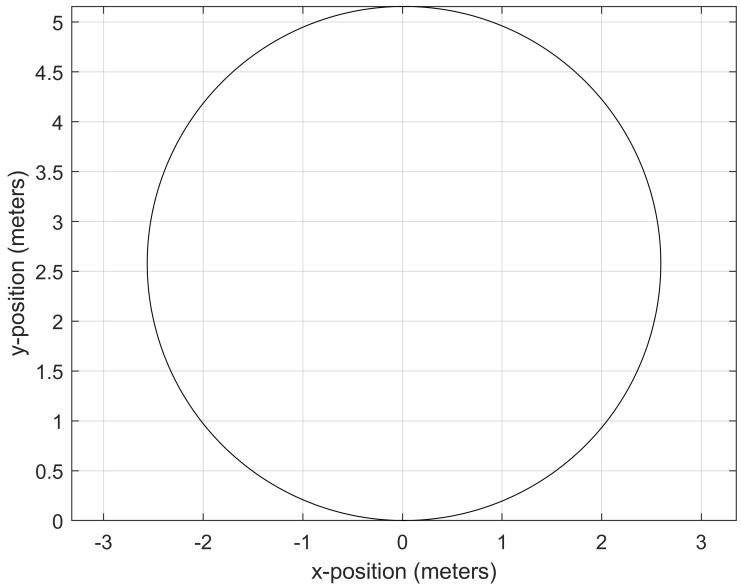

Figure 5.38. Full 6-DOF closed-loop simulation output for a full-scale omnidirectional propulsor UUV implementation with proportional feedback directed to surge and yaw. The input reference commands are velocities $u = 2$, $v = 0$, $r = \pi/4$, and other inputs are pose references set to zero. Linear position gains are set to 50, while angular position gains are set to 100.

Chapter 6

Conclusion

This chapter summarizes the content and contributions within this dissertation, and speculates direction for the future of the mechanism.

6.1 Summary

This dissertation explores a novel omnidirectional propulsion mechanism for observation-class underwater vehicles, enabling for operation in environments outside the scope of current technology. The mechanism utilizes independently-powered rotors to command near-instantaneous forces and moments independently in all six degrees of freedom (DOF). The work presented in this dissertation validates the mechanism through physical small-scale experimentation, confirming near-instantaneous reaction time, and aligns with CFD results presented for the proposed theorized full-scale implementation. It is also shown that the magnitude of forces and moments generated is directly proportional to motor effort and corresponding commands, in par with theory. Any apparent couplings between different control modes are deeply understood and shown to be trivially accounted for, effectively uncoupling all six control parameters. A full 6-DOF model is constructed from the ground up utilizing first-principals and CFD maneuvering to simulate trajectory, with guidelines and information on avoiding redundancies in the literature regarding VPMM and coefficients. With the small-scale model and full scale simulation and analysis, the work successfully demonstrates the mechanism can generate nearly instantaneous omni-directional forces underwater in a controlled manner, with application to high-speed agile vehicles.

6.2 Possibilities for Future Work

As the work presented in this dissertation represents the creation of a novel design concept, there is a clear direction for how the research could progress in the future. First and foremost, future work clearly involves complete fabrication of the full-scale mechanism and full UUV implementation. Small scale tests have validated the theory, and the potential performance of such a vehicle would likely drive its manifestation.

Once a full-scale prototype is built, acceleration and top speed properties should be examined in a controlled environment, at first with selective degrees of freedom physically restricted. The ability to reject different forms of turbulence would then also be tested in a controlled setting, and design iterations and adjustments would be made accordingly. Design adjustments may also be required to further reduce noise from the oscillating blades, which may obscure and skew acoustic sensor readings.

The servos command immense force from within a relatively small angular range. To prevent the small margin of error of the servos from inducing position-control instabilities, the hydrofoil pivot points (Fig. 4.10) can be shifted minutely to create some level of stability around true-zero degree deflection. The magnitude of the intentional pivot offset would be made small to necessitate, yet still restrict, a small servo torque required to actuate the blades. The KST BLS662 servos were chosen in part for their exceptional torque, and are expected to easily overcome the small energy-well to achieve commands outside their margin of error. For precise control within the margin, the light blade-pitch stability also enables thrusts at a small precise fraction of the minimum servo on-state. This is done by either commanding actuators to the minimum angle (or some small desired angle) and varying only servo voltage, or by pulsing a minimum thrust on and off and effectively controlling duty cycle, as used with spacecraft attitude control [5, 25, 44].

Advanced algorithms may need to be developed for the vehicle to better process infor-

mation regarding its surrounds during operation. For example, the use of accelerometer data to potentially cancel Doppler-based noise from blade-related vibration in acoustics processing and imaging could be required if all mechanical solutions to limit noise (inclusive of any described in this dissertation) prove inadequate. Relatively high sonar frequencies and long wavelengths (compared to oscillation amplitude of the vehicle) may render this unnecessary. To broaden the range of usable rotor ESCs, nonlinear control algorithms [32] could be implemented to emulate PWM-torque linearity.

Finally, applications involving pose locking to external objects in dynamic environments (detailed in Chapters 1 and 5) would be explored. A completed full-scale device would ultimately be tested on the field, eventually using sensors to lock pose with a moving object or a static object while in the presence of heavy turbulence. There is strong potential for offensive or defensive military application not explicitly mentioned in this dissertation.

The desired hydrofoil, cord, and curve profile of the blades may be dependent on future application. The current triangular blade cord length profile $C(\mathrm{r})$ is designed in part to maximize bidirectional thrust in *surge*, whereas future designs could theoretically be optimized with more emphasis on a different parameter, like yaw or sway. To the same effect, the blades in the mechanisms presented are optimized around bullard pull for bidirectionality, whereas future mechanisms may be optimized around some nonzero forward cruise velocity, affecting the desired hydrofoil profile and adding the possibility for pitch to change with r. Cavitation effects at very low depths may also influence future blade designs. For applications involving large continuous cruise velocities, control surfaces may be adopted for improved maneuverability at speed, as described in Chapter 5. Depending on application, all outer blade tips on each rotor are likely to be linked together via thin outer hoops (one per rotor), to reduce idle oscillation and also to prevent physical damage to the vehicle or its surroundings upon undesired contact.

Appendix A: ROVs and AUVs Mentioned

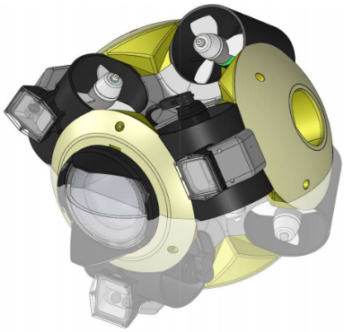

Figure 6.1. [9] CAD representation of the *MEROS* ROV. With a diameter of 0.4m, this omnidirectional ROV is similar in size to the proposed design. Dry weight: 13kg.

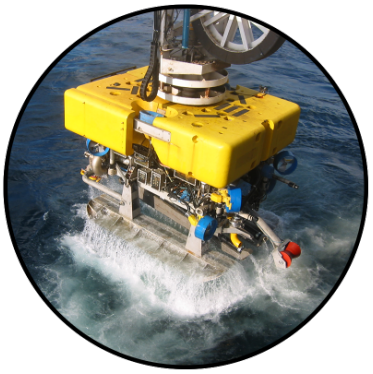

Figure 6.2. [2] The Oceana TRITON XL 100HP - CRANE LAUNCH ROV. This ROV is representative of heavy-duty workclass ROVs. Dry weight: 3500kg.

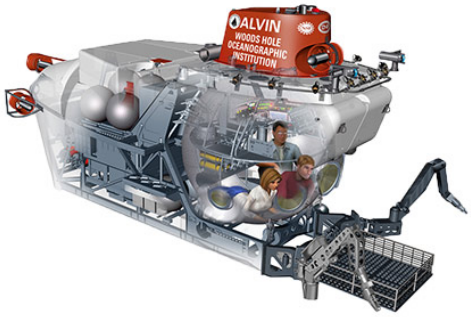

Figure 6.3. [47] The famous WHOI *Alvin* submersible. Though technically not remotely operated, its weight and performance specifications are representative of very large heavyweight work-class underwater vehicles in general. Dry weight: 15966kg.

Figure 6.4. [29] Saab's Seaeye TIGER 1000TMS ROV. Described as an observation class ROV. Dry weight: 150kg.

Figure 6.5. [2] Sub-Atlantic's SUPER MOHAWK TMS ROV. Described as a light work class ROV. Dry weight: 205kg.

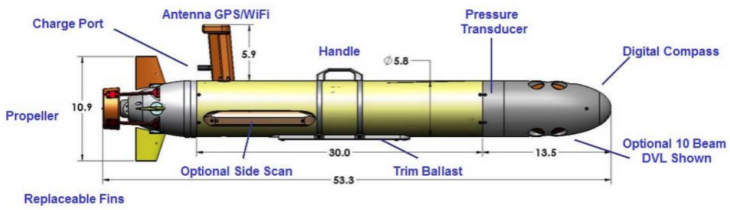

Figure 6.6. [6] The OceanServer Iver2-580 AUV. Length: 1.6m.

Figure 6.7. [20] The Bluefin-9M AUV. Length: 2.5m.

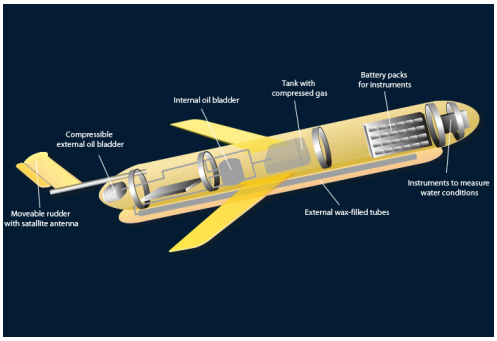

Figure 6.8. [48] The WHOI SLOCUM g-AUV. Length: 1.52m.

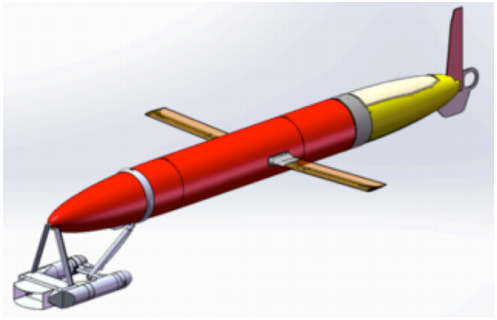

Figure 6.9. [13] The WHOI *Spray* g-AUV. Length: 2.0m.

Figure 6.10. The Huntington-Ingalls $FATB$ conceptual AUV. Length: 5.8m.

Bibliography

[1] Kamov Ka 25 (NATO reporting name: Hormone) walkaround. URL: https://travelforaircraft.wordpress.com/2015/07/15/kamov-ka-25-write/.

[2] Media Downloads — Oceana Subsea Independent ROV Services. URL: http://www.oceanasubsea.com/media-downloads/.

[3] AKVA. World's fastest ROV? - Project ROST, 2018. URL: https://www.akvagroup.com/news/news-archive/news-view/world-s-fastest-rov-project-rost.

[4] H. N. Arafat, D. J. Stilwell, and W. L. Neu. Development of a dynamic model of a small high-speed autonomous underwater vehicle. In *Proc. IEEE/MTS OCEANS*, 2006. doi:10.1109/OCEANS.2006.306895.

[5] Gilberto Arantes, Luiz S. Martins-Filho, and Adrielle C. Santana. Optimal on-off attitude control for the Brazilian Multimission platform satellite. *Mathematical Problems in Engineering*, 2009, 2009. URL: https://www.hindawi.com/journals/mpe/2009/750945/, doi:10.1155/2009/750945.

[6] Autonomous Undersea Vehicles Applications Center. HMC Iver 2 Spec Sheet, 2018. URL: https://auvac.org/241-2/.

[7] Bluefin Robotics. Bluefin Robotics Spray Glider. URL: https://geo-matching.com/auvs-autonomous-underwater-vehicles/spray-glider.

[8] Oliver (Nancy University) Botella and Yohann (Nancy University) Cheny. An Overview of the LS-STAG Immersed Boundary Method for Viscous Incompressible Flows. In *Computational Fluid Dynamics*, 2010.

URL: https://books.google.com/books?id=wP22dtOoOxkC&pg=PA610&lpg=PA610&dq=%22black+box%22+forces+method+hydrodynamics+cfd&source=bl&ots=FLneWGuE_Z&sig=_9R0LlUTATgJSe1S7Z66jEGHvd8&hl=en&sa=X&ved=2ahUKEwiL_L-Qu5vfAhUlvFkKHXSmCN0Q6AEwDXoECAMQAQ#v=onepage&q=%22bla.

[9] Lotfi Chikh. MEROS Project: Technical Advances in Modeling and Control. Technical report, Technalia, 2013. URL: https://sciencedocbox.com/Physics/69830737-Meros-project-technical-advances-in-modeling-and-control-dr-lotfi-chikh-february-33.html.

[10] Olivier Chocron, Urbain Prieur, and Laurent Pino. A validated feasibility prototype for AUV reconfigurable magnetic coupling thruster. *IEEE/ASME Transactions on Mechatronics*, 19(2):642–650, 2014. doi:10.1109/TMECH.2013.2250987.

[11] Ryan Coe. Virtual Planar Motion Mechanism Tests in a CFD Environment. In *Virginia Space Grant Consortium Student Research Conference*, number December, pages 1–8, Williamsburg, VA, 2014.

[12] Franco Concli, Carlo Gorla, Augusto Della Torre, and Gianluca Montenegro. Windage power losses of ordinary gears: Different CFD approaches aimed to the reduction of the computational effort. *Lubricants*, 2(4):162–176, 2014. doi:10.3390/lubricants2040162.

[13] Russ Davis, Daniel L Rudnick, and Jeff Sherman. Thoughts on second generation gliders. Technical Report c, Scripps Institution of Oceanography, La Jolla, CA. URL: https://alps-ocean.us/pdfs/Davis.pdf.

[14] Carol N. Eastwick and Graham Johnson. Gear windage: A review. *Journal of Mechanical Design, Transactions of the ASME*, 130(3):1–6, 2008. doi:10.1115/1.2829983.

[15] Ole Alexander Eidsvik and Ingrid Schjølberg. Determination of Hydrodynamic Parameters for Remotely Operated Vehicles. In *Volume 7: Ocean Engineering*, page V007T06A025. NTNU, 2016. URL: https://brage.bibsys.no/xmlui/handle/11250/2350869http://proceedings.asmedigitalcollection.asme.org/proceeding.aspx?doi=10.1115/OMAE2016-54642, doi:10.1115/OMAE2016-54642.

[16] Jerome Feldmen. DTNSRDC Revised Standard Submarine Equations of Motion. Technical Report June, DAVID W TAYLOR NAVAL SHIP RESEARCH AND DEVELOPMENT CENTER BETHESDA MD SHIP PERFORMANCE DEPT, 1979. URL: https://apps.dtic.mil/dtic/tr/fulltext/u2/a071804.pdf.

[17] Thor I Fossen. *Guidance and Control of Ocean Vehicles*. Wiley, New York, 1994.

[18] Thor I (NTNU) Fossen. *Handbook of Marine Craft Hydrodynamics and Motion Control*, volume 36. John Wiley & Sons Ltd, 1 edition, 2011. doi:10.1109/mcs.2015.2495095.

[19] José Carlos Gamazo-Real, Ernesto Vázquez-Sánchez, and Jaime Gómez-Gil. Position and speed control of brushless dc motors using sensorless techniques and application trends. *Sensors*, 10(7):6901–6947, 2010. doi:10.3390/s100706901.

[20] General Dynamics. Bluefin-9M Unmanned Underwater Vehicle (UUV), 2018. URL: https://gdmissionsystems.com/products/underwater-vehicles/bluefin-9-m-autonomous-underwater-vehicle.

[21] C A Goudey, T R Consi, J W Bales, D K Atwood, J J Leonard, and C Chryssostomidis. A Second Generation Survey AUV. *Proceedings AUV '94*, pages 148–155, 1994.

[22] S F Hoerner, W H Michel, L W Ward, and T M Buermann. Hydrofoil Handbook. Volume I, Design of Hydrofoil Craft, 1954. URL: https://apps.dtic.mil/docs/citations/AD0089648.

[23] Ehsan Javanmard, Shahriar Mansoorzadeh, and Javad A. Mehr. A new CFD method for determination of translational added mass coefficients of an underwater vehicle. *Ocean Engineering*, 215(August):107857, 2020. doi:10.1016/j.oceaneng.2020.107857.

[24] Michael E Kepler, Suraj Pawar, Daniel J Stilwell, Stefano Brizzolara, and Wayne L Neu. Assessment of AUV Hydrodynamic Coefficients from Analytic and Semi-Empirical Methods. In *OCEANS MTS/IEEE Charleston 2018*, 2018.

[25] Trond Dagfinn Krøvel. *Optimal Tuning of PWPF Modulator for Attitude Control*. PhD thesis, Norwegian University of Science and Technology, 2005. URL: http://folk.ntnu.no/tomgra/Diplomer/Krovel.pdf.

[26] J. Gordan Leishman. *Principles of Helicopter Aerodynamics*. Cambridge University Press, New York, 2 edition, 2006. URL: https://www.worldcat.org/title/principles-of-helicopter-aerodynamics/oclc/886667957.

[27] E V Lewis. *Principles of Naval Architecture - Motions in waves and controllability*, volume 3. SNAME, 2 edition, 1989. URL: http://opac.vimaru.edu.vn/edata/EBook/PrinciplesofNavalarchitecture.pdf.

[28] Roger H Maloof, Ned C Forrester, and Charles E Albrecht. A Brushless Electric Propulsion System for the Research Submersible Alvin. In *IEEE/MTS Oceans '86*, 1986.

[29] Marine Solutions Underwater Systems. Saab Seaeye Tiger Specifications, 2015. URL: http://www.marinesolutions.co.za/seaeye/tiger.shtml.

[30] Anirban Mazumdar and H. Harry Asada. Control-configured design of spheroidal, appendage-free, underwater vehicles. *IEEE Transactions on Robotics*, 30(2):448–460, 2014. doi:10.1109/TRO.2013.2291617.

[31] Jonathan McColgan and Euan McGookin. Coordination of Multiple Biomimetic Autonomous Underwater Vehicles Using Strategies Based on the Schooling Behaviour of Fish. *Robotics*, 5(1):2, 1 2016. URL: http://www.mdpi.com/2218-6581/5/1/2, doi:10.3390/robotics5010002.

[32] Chima E. Njaka, P. K. Menon, and Victor H.L. Cheng. Towards an Advanced Nonlinear Rotorcraft Flight Control System Design. *IEEE/AIAA Digital Avionics Systems Conference - Proceedings*, pages 190–197, 1995. doi:10.1109/dasc.1994.369483.

[33] Taylor Njaka, Stefano Brizzolara, and Pinhas Ben-Tzvi. Design and Simulation of a Novel High-Speed Omnidirectional Fully-Actuated Underwater Propulsion Mechanism. In *Proceedings of the 2019 ASME IDETC/CIE*. ASME, 2019. doi:10.1115/DETC2019-97534.

[34] Taylor Njaka, Stefano Brizzolara, and Pinhas Ben-Tzvi. Design and Experimental Validation of a Novel High-Speed Omnidirectional Underwater Propulsion Mechanism. *IEEE/ASME Transactions on Mechatronics*, (December), 2020. doi:10.1109/TMECH.2020.3037887.

[35] Taylor Njaka, Stefano Brizzolara, and Daniel Stilwell. CFD Investigation of Hull-Rudder Interaction for Improved Maneuvering Models. *SNAME Transactions 2019*, 127, 2019.

[36] Taylor Njaka, Lakshmi M Miller, Stefano Brizzolara, and Daniel J Stilwell. Method for Improving Existing Maneuvering Models to Accomodate Large Drift Angles. In *OCEANS MTS/IEEE Global 2020*. IEEE, 2020.

[37] Eduard (Kamov Company) Petrosyan. Aerodynamic Features of Coaxial Configuration Helicopter. Technical report, 2007. URL: https://web.archive.org/web/20071220021153/http://www.kamov.ru/market/news/petr11.htm.

[38] A. B. Phillips, M. Furlong, and S. R. Turnock. Virtual planar motion mechanism tests of the autonomous underwater vehicle autosub. In *CFD in Ship Design*, pages 1–8, 2007. URL: http://eprints.soton.ac.uk/48939/.

[39] S.M. Savaresi, F. Previdi, A. Dester, S. Bittanti, and A. Ruggeri. Modeling, Identification, and Analysis of Limit-Cycling Pitch and Heave Dynamics in an ROV. *IEEE Journal of Oceanic Engineering*, 29(2):407–417, 4 2004. URL: http://ieeexplore.ieee.org/document/1315729/, doi:10.1109/JOE.2004.826902.

[40] Yang Shi, Chao Shen, Huazhen Fang, and Huiping Li. Advanced control in marine mechatronic systems: A survey. *IEEE/ASME Transactions on Mechatronics*, 22(3):1121–1131, 2017. doi:10.1109/TMECH.2017.2660528.

[41] Kazuya Shirahata. Speed Control Methods of Various Types of Speed Control Motors. Technical report, Oriental Motor. URL: https://www.orientalmotor.com/brushless-dc-motors-gear-motors/technology/pdf/speed-control-methods-speed-control-motors.pdf.

[42] George Gabriel Stokes. On the Theories of the Internal Friction of Fluids in Motion, and of the Equilibrium and Motion of Elastic Solids. In *Mathematical and Physical Papers vol.1*, volume 3, pages 75–129. URL: http://mural.uv.es/daroig/documentos/stokes1850.pdfhttp://ebooks.cambridge.org/ref/id/CBO9780511702242A009, doi:10.1017/CBO9780511702242.005.

[43] Kantapon Tanakitkorn, Philip A. Wilson, Stephen R. Turnock, and Alexander B. Phillips. Depth control for an over-actuated, hover-capable autonomous underwater vehicle with experimental verification. *Mechatronics*, 41:67–81, 2017. URL: http://dx.doi.org/10.1016/j.mechatronics.2016.11.006, doi:10.1016/j.mechatronics.2016.11.006.

[44] Akshay Reddy Tummala and Atri Dutta. An overview of Cube-Satellite propulsion technologies and trends. *Aerospace*, 4(4):1–30, 2017. URL: https://www.mdpi.com/2226-4310/4/4/58/htm, doi:10.3390/aerospace4040058.

[45] Sergey Vladimirov. Ka-52 Helicopter at MAKS-2009 aeroshow. URL: https://www.flickr.com/photos/vlsergey/3856568537/in/album-72157622018414559/.

[46] Robert Wernli. The Present and Future Capabilities of Deep ROVs. *Marine Technology Society Journal*, 33(4):26–40, 1 1999. URL: http://openurl.ingenta.com/content/xref?genre=article&issn=0025-3324&volume=33&issue=4&spage=26, doi:10.4031/MTSJ.33.4.4.

[47] Woods Hole Oceanographic Institution. Alvin Upgrade, 2016. URL: https://www.whoi.edu/what-we-do/explore/underwater-vehicles/hov-alvin/history-of-alvin/alvin-upgrade/.

[48] Woods Hole Oceanographic Institution. WHOI OceanRobots Gliders, 2018. URL: https://www.whoi.edu/oceanrobots/robots/glider.htmlhttps://www.whoi.edu/oceanrobots/robots/images/glider1.jpg.

[49] WORTMANN. WORTMANN FX 76-100 (fx76100-il). URL: http://airfoiltools.com/airfoil/details?airfoil=fx76100-il.

[50] Hans Klein Woud and Douwe Stapersma. Chapter 3 Propulsion and Electric Power. In *Design of Propulsion and Electric Power Generation Systems*, chapter Chapter 3. IMarEST, London, 2002.

[51] Yi Yang, Zhenhui Fan, Zhongjing Zhu, and Jianqing Zhang. Underwater Modeling, Experiments and Control Strategies of FroBot. *IEEE International Conference on Intelligent Robots and Systems*, pages 6397–6403, 2018. doi:10.1109/IROS.2018.8594455.